



## MASTERS THESIS

SUBMITTED IN PARTIAL FULFILLMENT OF THE REQUIREMENTS  
FOR THE DEGREE OF **MASTER OF MECHANICAL ENGINEERING**

**TITLE:      Modeling, Simulation, and Control of an Omni-directional Robotic Ground Vehicle**

**PRESENTED BY: Andrew Niedert**

**ACCEPTED BY:**

**Advisor, *Dr. Richard Hill***

**Date**

**Department Chairperson, *Dr. Nassif Rayess***

Date \_\_\_\_\_

**APPROVAL:**

**Dean, *Dr. Leo E. Hanifin***  
**College of Engineering and Science**

**Date**

***To my parents Gene and Joann Snyder***

*Thank you for your never ending love,  
support, and encouragement. I truly believe  
it gave me the determination to rise above every  
challenge in life past, present, and future.*

# Contents

List of Figures .....	i
List of Tables .....	vi
Chapter 1 Introduction .....	1
1.1 Motivation of the Project .....	1
1.2 Motivation and Progression of this Report.....	3
1.3 Other Omni-directional Vehicle Architectures.....	4
1.3.1 Three-pod Designs .....	5
1.3.2 Skid-steer Designs.....	7
1.3.3 Special Wheel Types .....	8
1.4 Omni-directional Vehicle Architecture Used in this Project.....	11
1.5 The Progression of the Project .....	14
Chapter 2 Hardware Identification and Set-up .....	18
2.1 Vehicle Design and Architecture .....	18
2.1.1 Overall Mechanical Design (Mechanical).....	18
2.1.2 Overall Vehicle Design (Control).....	23
2.2 Chassis .....	28
2.3 Pod Design.....	29
2.4 Motor Controllers .....	31
2.5 Maxon EC 45 Flat Motors .....	33
2.6 Slip-rings, Data Acquisition Cards and Wiring, and Encoders.....	34
2.6.1 Slip-rings.....	34
2.6.2 Encoders .....	36
2.6.3 Data Acquisition Cards.....	37
2.6.4 Wiring .....	39
2.7 Masses, Inertias, and Dynamic Characteristics .....	43
2.8 Human Interface and Control.....	46
Chapter 3 Software Description.....	50
3.1 LabVIEW .....	50
3.2 Overall Vehicle VI.....	52
3.3 Gamepad Controls .....	61

3.4 Encoder Sub-VI.....	65
3.5 Desired Pod Angle Sub-VI.....	68
3.6 Inverse Kinematics Sub-VI.....	72
3.7 Closed-loop Control System Sub-VI .....	76
3.8 Pod Voltage Control Sub-VI .....	84
Chapter 4 Vehicle Parameterization .....	87
4.1 Modeling Preparation.....	87
4.2 Tire Model.....	87
4.2.1 Rolling Resistance.....	88
4.2.2 Longitudinal Tire Forces .....	89
4.2.3 Lateral Tire Forces .....	94
4.3 Air Resistance .....	97
4.4 Closed-loop Motor/Wheel Speed Control Characterization.....	99
4.5 Slip-ring Friction .....	102
Chapter 5 Simulation and Control .....	107
5.1 Simulation and Control Overview .....	107
5.2 Control Strategy and Simulation Architecture .....	108
5.3 Desired Pod Angles – Setpoint Generation .....	112
5.4 Inverse Kinematics Model – Feedforward Control .....	114
5.5 Pod Control – PID Controller .....	117
5.6 Wheel Speed Model Sub-model – Transfer Functions.....	122
5.7 Tire Model.....	125
5.7.1 Longitudinal Tire Model .....	126
5.7.2 Lateral Tire Model.....	128
5.7.3 Rolling Resistance.....	129
5.8 Air Drag Model.....	130
5.9 ODV Plant Sub-model.....	132
5.10 Pod Models .....	138
Chapter 6 Simulation and Actual Vehicle Comparison.....	144
6.1 The Comparison of the Actual ODV to the Simulation.....	144

6.2 Longitudinal Comparison .....	145
6.3 User Defined Turn and Vehicle Controller Comparison.....	153
6.4 Test Course Comparison .....	157
Chapter 7 Project Reflection and Future Work.....	164
7.1 Summary of Project.....	164
7.2 The Progression of the Project .....	165
7.3 Reflection and Future Builds .....	167
7.3.1 Build Quality, Manufacturing, and Materials .....	167
7.3.2 Motors, Gearboxes, and Batteries .....	168
7.3.3 Suspension.....	170
7.3.4 Slip-rings.....	171
7.3.5 Tires and Wheels.....	171
7.3.6 Simulation and Software .....	172
7.4 Conclusion .....	176
References.....	177

## ***List of Figures***

Figure 1-1 Three-wheeled Omni-directional Vehicle Architecture [2] .....	6
Figure 1-2 An Example of a Skid-steer Chassis and Drivetrain [6] .....	8
Figure 1-3 Photos of a Mecanum Wheel [8].....	9
Figure 1-4: A Sample Vehicle Utilizing the Mecanum Wheel [4] (top) [7] (bottom).....	10
Figure 1-5 Vehicle Architecture and Layout [1].....	12
Figure 1-6 The Progression of the ODV at the end of August 2007 [1].....	14
Figure 1-7 Pod Assembly at the end of August 2007 [1] .....	15
Figure 2-1 Approximate Dimensions of the Chassis and Pod .....	18
Figure 2-2 CATIA 3D Rendering of the ODV [1] .....	19
Figure 2-3 Isometric View of Mechanical Assembly with Body Coordinate Frame [1]...	20
Figure 2-4 Front View of Mechanical Assembly with z-axis [1] .....	20
Figure 2-5 Overall Vehicle Control Block Diagram w/Control System.....	23
Figure 2-6 Top-level Vehicle Wiring Schematic.....	25
Figure 2-7 Pod Design and Suspension Layout (suspension movement shown) [1].....	29
Figure 2-8 Completed Pod Assembly .....	30
Figure 2-9 1-Q-EC Amplifier DEC 50/5 Controller [15] .....	31
Figure 2-10 Switch Configuration for Speed Control [15].....	32
Figure 2-11 EC 45 Flat Brushless Motor [16] .....	34
Figure 2-12 Summary of Data Acquisition Card Pin Layout [17].....	39
Figure 2-13 DC Motor Pin Layout [16].....	41
Figure 2-14 Wiring Diagram Between the DC Motor and Controller.....	41
Figure 2-15 Wiring Set-up Between Data Acquisition Card and Motor Controller.....	42

Figure 2-16 Wiring Set-up Between Acquisition Card and Encoder .....	42
Figure 2-17 Test Experiment for Determining the Moment of Inertia of an Object [18]..	45
Figure 2-18 Xbox 360 Wireless Game Pad [20].....	49
Figure 3-1 Front Panel Screen Shot of the Overall Vehicle VI .....	53
Figure 3-2 Voltage Circle .....	54
Figure 3-3 Pod and Wheel Numbering System .....	56
Figure 3-4 Overall Vehicle VI Back Panel Summary Block Diagram.....	58
Figure 3-5 Gamepad VI Back Panel .....	61
Figure 3-6 Gamepad Button Summary (Front) [20] .....	62
Figure 3-7 Gamepad Button Summary (Back) [21] .....	63
Figure 3-8 Encoder VI Back Panel (Matrix Comparison) .....	66
Figure 3-9 Encoder VI (Front Panel) .....	68
Figure 3-10 Breakdown of Various Kinematic Inputs on the Vehicle .....	70
Figure 3-11 The Orientation of Pod Joints in Relation to the Chassis.....	70
Figure 3-12 Desired Pod Angle VI Back Panel (Construction of the N-Matrix and User Inputs) .....	71
Figure 3-13 Desired Pod Angle VI Back Panel (N-Matrix and Pod Angle Output) .....	72
Figure 3-14 Pod Geometry Description [1] .....	73
Figure 3-15 Feedforward Control Back Panel (Construction of Equation 3-1).....	74
Figure 3-16 Feedforward Control Back Panel (Wheel Voltage Calculation and Normalization) .....	75
Figure 3-17 PID Gain VI Back Panel .....	77
Figure 3-18 PID Gain VI Back Panel (Error Calculation).....	78
Figure 3-19 Control Effort and Direction Sub-VI within the PID Gain Sub-VI .....	79

Figure 3-20 Control Effort Calculation as a Function of Calculated Pod Error .....	80
Figure 3-21 Direction Calculation as a Function of Calculated Pod Error .....	81
Figure 3-22 Control System VI Back Panel .....	82
Figure 3-23 5-Volt Normalization VI Back Panel .....	83
Figure 3-24 Pod Voltage Control Sub-VI Back Panel (Analog Signals).....	85
Figure 4-1 Coast-down Test Results for Determining Rolling Resistance.....	89
Figure 4-2 Explanation of Variables in Slip Ratio Formula .....	90
Figure 4-3 Example Velocity Profile Used to Calculate Slip Ratio .....	91
Figure 4-4 Slip Ratio versus Accelerating Force .....	92
Figure 4-5 Complete Longitudinal Tire Model .....	94
Figure 4-6 Lateral Tire Force Generation .....	95
Figure 4-7 Experimental Set-up for Measuring Lateral Force.....	96
Figure 4-8 Lateral Tire Force Data and Model .....	97
Figure 4-9 1-Volt Straight-Line Acceleration Transfer Function (Step Input Response) .....	100
Figure 4-10 5-Volt Straight-Line Acceleration Transfer Function (Step Input Response) .....	100
Figure 4-11 Pod Coast-down Test Results.....	103
Figure 4-12 Pod 1 Coast-down Velocity Profile.....	104
Figure 4-13 Pod 2 Coast-down Velocity Profile.....	104
Figure 4-13 Pod 3 Coast-down Velocity Profile.....	105
Figure 5-1 Overall Vehicle Control Block Diagram w/ Control System.....	109
Figure 5-2 Overall Simulation Architecture .....	111
Figure 5-3 M-file Containing all Vehicle Parameters and Characteristics .....	111

Figure 5-4 Desired Pod Angle Sub-model Location .....	113
Figure 5-5 Desired Pod Angles Sub-model Contents .....	114
Figure 5-6 Inverse Kinematics Sub-model Location .....	115
Figure 5-7 Inverse Kinematics Sub-model .....	116
Figure 5-8 Pod Control Sub-model Location.....	117
Figure 5-9 Pod Control Sub-model.....	118
Figure 5-10 Wheel Voltage Normalization Function .....	121
Figure 5-11 Wheel Speed Model Sub-model Location .....	122
Figure 5-12 Wheel Dynamics Sub-model Block Diagram.....	123
Figure 5-13 Tire Sub-model Locations.....	125
Figure 5-14 Longitudinal Tire Sub-model.....	126
Figure 5-15 Lateral Tire Sub-model .....	128
Figure 5-16 Rolling Resistance Sub-model .....	130
Figure 5-17 Air Resistance Sub-model.....	131
Figure 5-18 Plant Sub-model Location.....	133
Figure 5-19 Summation of Longitudinal Forces within the ODV Plant Sub-model .....	134
Figure 5-20 Lateral Tire Force and Pod Location within the Plant Model.....	135
Figure 5-21 Air Resistance Forces and Chassis Location within the ODV Plant Sub-model .....	136
Figure 5-22 Chassis Information Block.....	137
Figure 5-23 Simulink's Chassis (blue) and Pod (gray) Graphical Representation.....	138
Figure 5-24 Inside a Pod Sub-model (Planar and Revolute Joints).....	139
Figure 5-25 Longitudinal Velocity and Direction Calculation .....	141

Figure 5-26 Lateral Slip Angle and Direction Calculation .....	143
Figure 6-1 1-Volt Acceleration Profile for the Simulation and Actual Vehicle .....	146
Figure 6-2 5-Volt Acceleration Profile for the Simulation and Actual Vehicle .....	147
Figure 6-3 1-Volt Various Acceleration and Deceleration Profile Comparing the Simulation to the Actual Vehicle .....	150
Figure 6-4 2-Volt Acceleration Profile for the Simulation and Actual Vehicle .....	151
Figure 6-5 Commanded Turn Profile $V_y = 2V$ , $\omega = +0.06$ to $+0.50$ rad/s .....	154
Figure 6-6 Test Course Layout and Desired Path .....	157
Figure 6-7 Simulation and Actual Vehicle Turn Command Timing .....	160
Figure 6-8 Chassis Heading Comparison .....	161

## ***List of Tables***

Table 2-1 Description of Wiring Pathways in Figure 2-6.....	26
Table 2-2 Motor Pin Summary [16].....	40
Table 2-3 Summary of Pin Connections Passing through the Slip-rings.....	43
Table 2-4 Summary of Masses and Inertias.....	45
Table 3-1 Gamepad Button Summary .....	63
Table 5-1 Ziegler-Nichols Method for Tuning Control Gains [28].....	119
Table 6-1 Command Timing Comparison .....	160

# ***1. Introduction***

## **1.1 Motivation of the Project**

In an effort to modernize the military, it has become necessary to explore the limits of mobile robotics with high mobility and speed in mind. A specialized vehicle was created in response to such a task. This vehicle was to have three major attributes which set it apart from existing types of mobile robotic vehicles. This includes three pods (for stability), six wheels (two on each pod for traction and steering), and zero-turn radius capability (for maneuverability). This vehicle was also configured to be tele-operated as to allow soldiers to remain at a safe distance.

One particular use of such a robotic vehicle is to inspect the chassis or undercarriage of military vehicles such as the Humvee [1]. This application requires the vehicle to have a low-profile. While the inspection process in itself does not require the robot to be highly mobile or to have high speed, there is a high probability to inspect more than one vehicle in one session, and since military vehicles are driven on various surfaces, the inspection vehicle should be mobile and quick. This new vehicle should be able to traverse various terrain profiles ranging anywhere from smooth parking lots to small obstacles in an off-road setting.

Inspecting the undercarriage of vehicles often requires soldiers to be placed in dangerous situations. In an attempt to reduce risk, cost, and improve the ease of inspection, the need for such a vehicle has developed. The challenges presented by this problem drove the nature of the design of this new tele-operated ground vehicle.

Due to the need for the vehicle to be highly mobile and relatively quick, the vehicle needed to be easily and intuitively controlled. Due to the nature of a soldier's job, the vehicle should not be operated by direct contact from the soldier. In this particular application, the reason a vehicle, such as this, exists is so that the soldier does not have to be placed in harm's way. This requirement makes it imperative that the soldier be able to control the device remotely. Furthermore, a soldier should be able to pick up the controller and instinctively know how to operate the vehicle.

The uses of the technology are not only limited to military or inspection uses. This is merely one use of the technology and one area where it has become necessary. Many other applications exist that require zero-turn radius operations combined with high amounts of traction. It is not inconceivable to see this technology make its way into modern lawnmowers, ship container movers, automated vacuum cleaners, and maybe someday passenger vehicles. This project is still in the early stages of development and offers a proof of concept and a test bed for which other applications can be explored.

Physically constructing the vehicle allows the opportunity to observe any unforeseen problems. With only theory or simulation to back up any hypotheses, it could be easy to overlook even simple problems. Building the vehicle also opens up the opportunity to explore how the driver will interface with the vehicle. It is now easier to evaluate the intuitiveness of the vehicle controls. Later, the vehicle may be modified for fully autonomous control or to test new physical dimensions and configurations.

## **1.2 Motivation and Progression of this Report**

The purpose of this document is to explain the development of the Omni-directional Vehicle (ODV) as it is currently being used. This report explains the physical layout of the vehicle as well as all of its components. All of this is done in preparation for the explanation of the control system and overall control strategy used on the vehicle. The motivation of the project, as mentioned in Section 1.1, only sets a specific need on the physical requirements of the vehicle. However, it is the control system and strategy, in conjunction with the mechanical design of the vehicle, that allow the vehicle to successfully fulfill the goals for which it was designed.

The remainder of Chapter 1 discusses other vehicle architectures that could have been used and provides reasoning as to why the current architecture was chosen. Chapter 2 provides a breakdown of the physical components of the vehicle and discusses how the components are physically connected and how they communicate with one another.

Building off of the physical components, Chapter 3 explains the software and how to control the vehicle. It discusses the LabVIEW programming environment employed and explain how the software provides overall communication to and from all of the actuators and sensors on the vehicle. Chapter 3 also begins to give insight into the vehicle's overall control strategy.

In Chapter 4, explanations of the vehicle's physical characteristics are provided. It covers test methods and results that graphically show how the vehicle accelerates, decelerates, and maneuvers. This data allows the characterization of physical parameters such as the dynamics of the electronic motors, the air drag constant for the vehicle, the

character of the friction in the slip-rings, and yields an overall picture of the tire characteristics.

Chapter 5 discusses the simulation environment and how MATLAB and Simulink are used to simulate the vehicle. Chapter 5 combines the dynamic physical characteristics of Chapter 4 with the inertias, masses, and dimensions of the components found in Chapter 2. All of these elements were needed to create a simulation model that could be useful for testing different vehicle geometries and configurations. The simulation also provided a test bed to test new control strategies before risking any damage to the hardware on the actual vehicle.

Chapter 6 compares data from the actual vehicle to results from the simulation. Several driving test cases have been conducted with the actual vehicle for the purposes of benchmarking. The trajectory of the chassis, wheel speeds, and control system effectiveness is compared to the simulation using comparable user inputs. Finally, Chapter 7 concludes the report and discusses the results from Chapter 6. Additional information regarding possible directions for future work and reflection on the project as a whole will be given in this chapter.

### **1.3 Other Omni-directional Vehicle Architectures**

Omni-directional vehicles are a special type of vehicles that allow ground travel in any direction without the need to rotate the chassis or body. They offer zero-turn radius capability, thus allowing the vehicle to operate in confined spaces. Most ground vehicles have a drivetrain type which confines how the vehicle traverses terrain, usually

confining the chassis orientation. An Omni-directional vehicle has a drivetrain that allows the vehicle to travel in any direction and with any chassis orientation.

There are a variety of architectures that allow for zero-turn radius maneuvers; one of the major design considerations for the project. Each of these approaches offers its own benefits and drawbacks. A few of these architectures are described in section 1.3.1, before the specific approach applied in this project is discussed. The specific classes of omni-directional vehicle that will be discussed are three-pod, skid-steer, four-wheeled, and vehicles using specialized wheels. The architecture employed in this project is compared and contrasted to these other known techniques.

### **1.3.1 Three-pod Designs**

The three-pod designs utilize six motors, and are commonly broken down into two variations. In one variation, each pod contains one wheel and one motor to control the vehicle's velocity. A separate steering motor is used to control the orientation of each pod [2] [3]. *Figure 1-1* shows an example of a three-wheeled, three-pod omni-directional architecture.

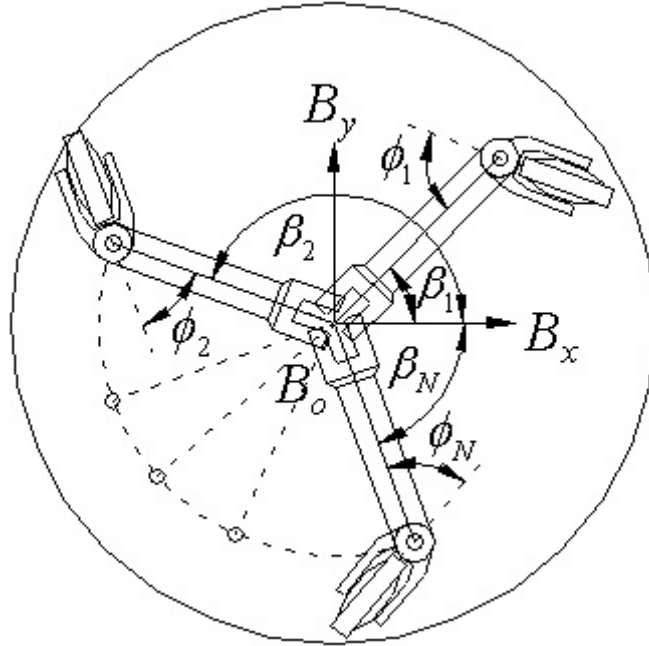


**Figure 1-1 Three-wheeled Omni-directional Vehicle Architecture [2]**

The architecture presented in this document shows that the same number of motors (six motors) can be utilized in a different way than the three-pod, three-wheeled omni-directional architecture. Six motors are now used to propel the vehicle rather than reserving three solely for the purposes of steering the vehicle. It uses six wheels rather than three, and the steering is achieved by a difference of velocity between the right and left wheels on each of the pods.

An advantage of having six wheels on the ground, rather than three, is that it increases the maximum force that can be applied at the ground/tire interface and in turn increases the speeds that can be achieved. The vehicle architecture presented will be discussed in further detail in Section 1.4.

### **1.3.2 Skid-steer Designs**

Skid-steer vehicles, similar to a tank, offer zero-turn radius capability. They have a chassis which is supported by wheels or a track system. The wheels or tracks are laid out similar to that of a passenger vehicle. Though the vehicle may look similar to a passenger vehicle in terms of drivetrain, it does not steer in the same fashion. The wheels or tracks are aligned in parallel with the chassis's intended direction and never change their angle in relation to the chassis. The vehicle is able to steer or change direction due to a velocity difference between the right and left wheel sets or track systems [4] [5].

The pod structure, as described in this document, utilized the ability to control a velocity difference between the right and left wheels. This orientation method will directly control the direction of the pods and indirectly control the orientation of the vehicle's chassis.

This method proves very effective for rotating the chassis especially where a zero-turn radius is necessary. It is very simple to implement mechanically, and is relatively simple to implement from control a control standpoint.

The traditional application of skid-steer was not chosen for this project because zero-turn radius is not the only requirement of the vehicle. The orientation of the chassis is something that also needs to be controlled, either to maneuver the vehicle around, or to point a particular part of the vehicle in a certain direction. Many applications, besides vehicle undercarriage inspection, could require control of the orientation of the chassis. For instance, large cargo containers aboard a cargo ship could require an omni-directional vehicle which could perform strafe maneuvers without changing the orientation of the cargo. A skid-steer vehicle cannot perform this function simply because the wheels

cannot be oriented in relation to the chassis. Therefore, the direction of motion of the wheels always forces the front of the chassis in the same direction. An example of a skid-steer vehicle is shown in *Figure 1-2*.

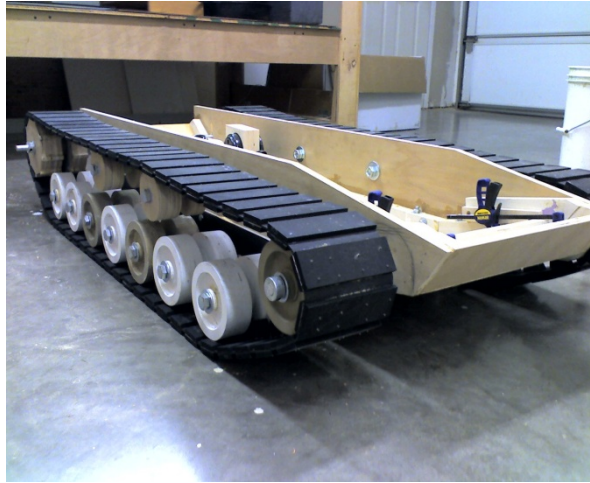


**Figure 1-2 An Example of a Skid-steer Chassis and Drivetrain [6]**

### **1.3.3 Special Wheel Types**

Other types of omni-directional vehicles have a drivetrain that look very similar to that of the skid-steer type vehicles. Like the skid-steer vehicles, the wheels never change their angle in relation to the chassis. Instead, they employ specialized wheels, such as the mecanum wheel, to do all of the turning and chassis orientation [4] [7]. *Figure 1-3* shows an example of a mecanum wheel.

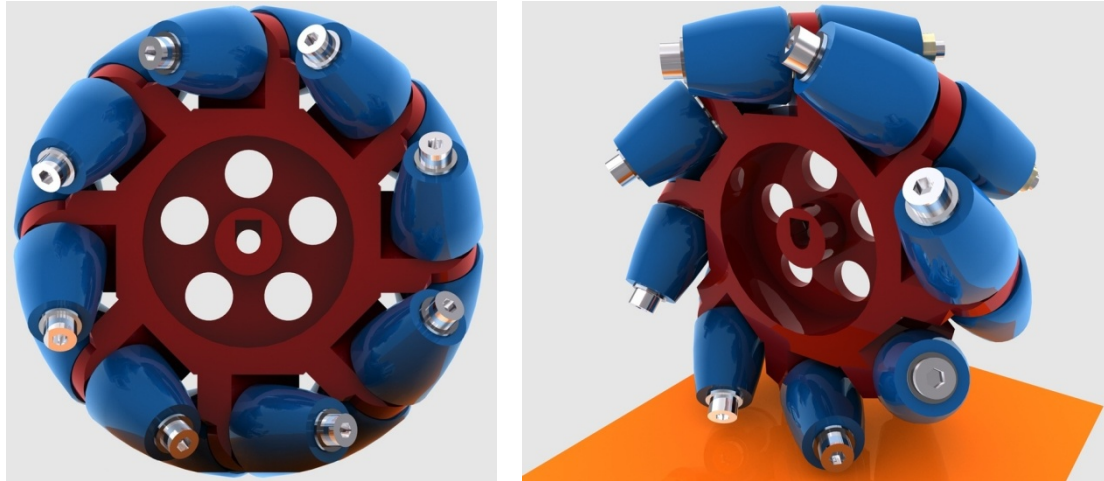


**Figure 1-3 Photos of a Mecanum Wheel [8]**

The side profile of the mecanum wheel looks similar to that of an ordinary wheel or tire and wheel assembly. The wheel is still circular and this why a vehicle equipped with these wheels can roll forward. A vehicle equipped with this type of wheel, however, can also move side-to-side (strafe) or can rotate its chassis with no translational movement.

For right and left turns, the vehicle operates in much the same way as the skid steer application. As long as there is a difference of velocity in the right and left side wheels, the vehicle will rotate the chassis. The shape and placement of the rollers in the mecanum wheels as shown in *Figure 1-3* is what allows the equipped vehicle to move in a direction not aligned with the chassis. For example, rotating the rear wheels in an opposite direction to the front wheels will cause the chassis to translate left or right depending on the orientation of the rollers. In order for this to work properly, however, the direction of the rollers on the rear wheels need to be opposite in direction of the rollers on the front wheels. Moreover, the direction of the rollers between the right side and the left side of the vehicle also must have opposing directions. Therefore, the rollers

on the left front and right rear will be facing the same direction, and the rollers on the right front and left rear will be facing the same direction. *Figure 1-4* shows a vehicle layout using the mecanum wheels.

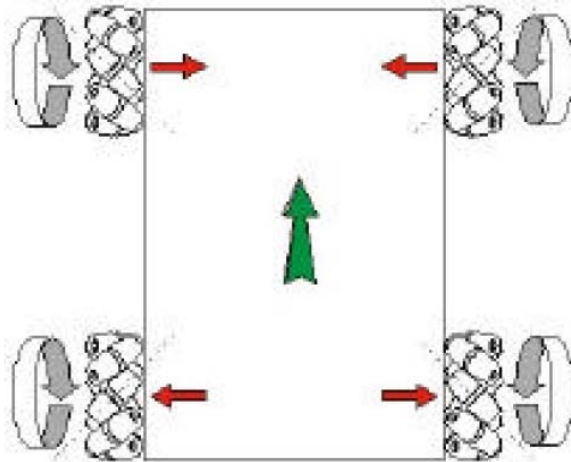
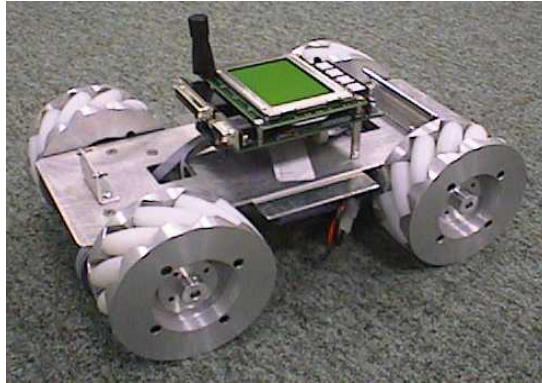


**Figure 1-4 A Sample Vehicle Utilizing the Mecanum Wheel [4] (top) [7] (bottom)**

Though this layout proves to be very advantageous for control of vehicle orientation and translational movement, there are some drawbacks. This architecture type does not lend itself well for the overall efficiency of the vehicle. For the same reasons that the mecanum wheels are advantageous, they are also inefficient. This is due in part because the wheel is always exerting a force perpendicular to the direction of travel as well as parallel to the direction of travel. When the vehicle is utilized for only a single direction of travel, only one component of the force generated by the wheel is used

to move the vehicle. Since the rest of the forces generated by the wheels are opposing one another, the vehicle is wasting energy only to keep itself stabilized.

Yet another disadvantage is that the vehicle using these wheels can only be used on certain surfaces. The wheels and tread surfaces are usually constructed of relatively hard materials such as plastics. This offers little compliance to any disturbance presented by the surface that the vehicle is trying to traverse. The standard pneumatic tire offers the ability to maintain a tractive force even over small obstacles or debris [3] [9].

The shape of the mecanum wheel also prevents off road use and, therefore, is usually restricted to use on flat terrain. The reason the wheels need flat terrain is so that the road is always ensured to come in contact with the center of the wheel. If the wheel contacts the road surface at the side wall or the side of the rollers, the entire mechanism for which the wheels are able to work is no longer present. This situation changes the direction and magnitude of the forces generated by the wheels which will induce an undesired moment on the chassis. It is the balance of forces on the chassis which keep the chassis orientated as desired. Once this balance is disturbed by an off-cambered surface, the control system and/or the user would lack the ability to maintain proper control of the vehicle. Due to the possible application of the proposed vehicle to different terrains, this type of architecture was not chosen for this project [3] [10].

## **1.4 Omni-directional Vehicle Architecture Used in this Project**

The architecture chosen for the vehicle used in this project, as mentioned previously, consists of three pods, each of which includes two independently driven wheels. Each wheel is driven by its own motor and the vehicle is steered by orienting the

pods through the differential motion of the left and right wheels of the pod. A schematic representation of the layout of the pods and wheels is shown in *Figure 1-5*.

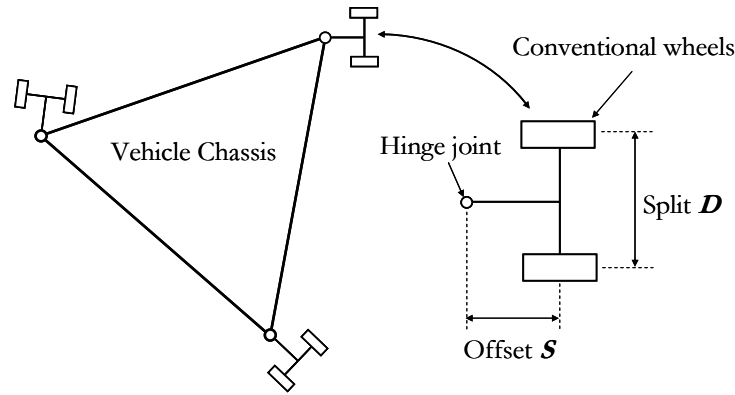


**Figure 1-5 Vehicle Architecture and Layout [1]**

*Figure 1-5* represents the active split offset castor (ASOC) design employed for each pod [11]. The offset castor design (with distance  $S$ ) makes the vehicle holonomic in nature (less likely for a wheel to come to a complete stop during various maneuvers) and thus makes it is easier to traverse curved trajectories. In other words, the castor allows all three degrees of freedom of the pod (x-position, y-position, and orientation) to be controlled. Furthermore, using two wheels with a split ( $D$ ) reduces the load on each wheel and eliminates a great deal of the frictional forces inherent in a single wheel design. The dual wheel design reduces the chance that one of the wheels will have an angular velocity of zero (come to rest) while changing directions [11]. Wheels that continuously roll while changing directions maintain lower and consistent frictional forces by avoiding the stiction associated with the rest state. This leads to a much more smooth and predictable vehicle. This design can be seen on modern airliners. Having the offset split castored wheel mechanism alone does not ensure omni-directionality as some paths may require one of the wheels to stop while reorienting. However, an ASOC

design in conjunction with controlling the velocity of each wheel, any position and orientation of the hinge joint can be achieved. Allowing the joint to move instantaneously in any direction and orientation is the primary function of the ASOC design and is what makes the vehicle omni-directional [11].

The ASOC design allows the vehicle to be oriented independent of its direction of motion as opposed to more traditional skid-steered vehicles. Furthermore, this architecture allows for the generation of higher traction forces and the achievement of greater translational speed than other three-pod architectures due to the fact that six driven wheels are in contact with the ground, rather than only three. Also, this architecture also is more efficient than architectures that rely on mecanum wheels and allows for operation across a variety of terrains, which is not possible with mecanum wheels.

One possible disadvantage of the chosen architecture is that the control strategy that must be employed may be more complicated than required with other architectures. During development it was found that the vehicle could not be driven at high-speeds using an open-loop, kinematics-based control strategy and a dynamic controller needed to be designed and implemented. Specifically, the control strategy was designed to help the driver maintain the desired direction of motion and orientation of the vehicle in the presence of road disturbances or significant wheel slippage and scrubbing.

This section of the report introduced some examples of various types of architectures for omni-directional vehicles and explained the reasoning by which the ASOC architecture was chosen. It is, however, conceded that architectures other than

those considered here may have advantages and could be explored in the future. The architecture of this particular vehicle will be further explained and explored in Chapter 2.

## 1.5 The Progression of the Project

The construction of the vehicle chassis and drivetrain took place between January and August of 2007 by the senior mechanical engineering design class. All of the mechanical design was done by students enrolled in that class as well as most of the manufacturing and assembly. They did not finish the project as this project provided ample work for several semesters. Regardless, the work they did represented a great challenge for the senior design class and served well as a final project. *Figures 1-6 and 1-7* show the results of the work done by the senior class of 2007, as of August 2007. One can see that the students back in 2007 had completed the mechanical assembly of the pod and the chassis, and installed the batteries and encoders [1].

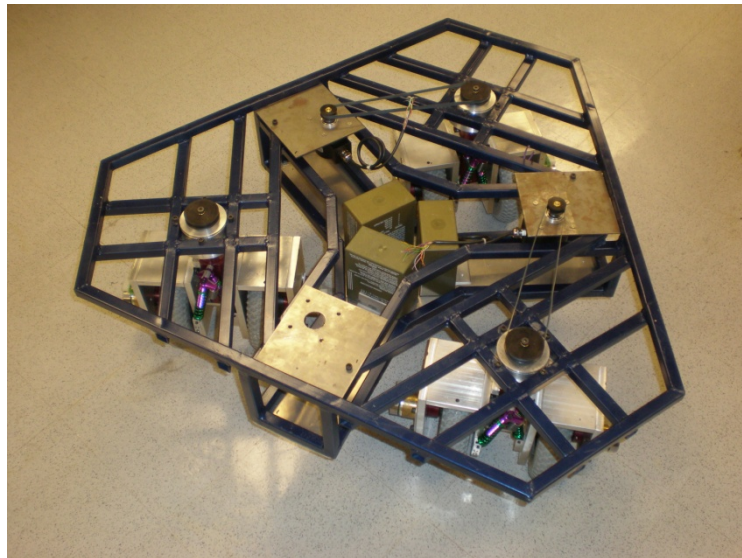


**Figure 1-6 The Progression of the ODV at the end of August 2007 [1]**



**Figure 1-7 Pod Assembly at the end of August 2007 [1]**

The remainder of the manufacturing, assembly, wiring, and computer control became a separate project since these three aspects became part of the overall control strategy. The slip-rings, allowing full electrical connectivity throughout a 360 degree rotation, represented the last of the major sub-assemblies. All other items related to the completion of the vehicle were a matter of preference on placement and did not influence the performance of the vehicle.

The choice of signals to include in the data acquisition and the hardware associated with the overall control of the vehicle aided in clarifying the final layout of the vehicle. For example, the data acquisition cards were one type of component that placed limitations on the way the vehicle was wired. The limitations on the number of available data acquisition channels forced a choice between the features that made it onto the vehicle and those that did not. Limitations such as these are what resulted in the final configuration and capabilities of the vehicle. Placement of the data acquisition boxes, motor controllers, wire routing and battery connections were all set as necessary to

provide the proper function of the vehicle. The wiring was kept as short as possible while trying to maintain a simple layout to the components.

The remaining items assembled onto the vehicle were not critical to the larger design of the vehicle, but were necessary for its function. The encoders, pulleys on the encoders and pods, belts, belt tensioners, and miscellaneous bracketry represented the last of the mechanical assembly.

The battery connectors and wires were soldered together to allow power to the vehicle. Three wire and connector assemblies, one for each battery, were needed which were later installed into the floor pan. The gearboxes for the electric motors also provided a small hurdle which required machining work. One of the gears inside each gearbox was plastic and had to be switched out for a metal gear in order to ensure durability. Later, a flat surface was machined into the output shafts of the gear boxes. The flat surface provided flat spots needed for set screws needed to couple the gear boxes to the wheel axles.

Once the machine work and assembly was completed, the controls aspect of the project could be developed. A laptop equipped with LabVIEW served as the interface between the hardware that physically actuates and senses the vehicle and the software that controls how the hardware operates.

Although there were several control strategies that could be studied, not all were explored. The reasons for this are time, manpower, money, and the current state of the vehicle. The goal was simply to get the vehicle to work well enough to achieve the given operational requirements so that the vehicle could be employed as a proof of concept. For these reasons, control at the pod level was the avenue chosen. Control at the vehicle

level was one choice considered, but the vehicle had an emphasis on speed and reaction time. With these requirements, a pod-level approach to control was deemed better in comparison to vehicle-level approach to control.

Since the pods are smaller and have less inertia than the overall chassis, the pods should conceivably be quicker to respond to inputs from both the operator and the control system. The pods are closer to the point where the forces are actually generated, at the wheel, therefore, there are fewer dynamics between what is being controlled and the actuation being employed to achieve the desired control. Furthermore, vehicle-level control would require the use of an inertial sensor, which is potentially expensive. While it is ultimately the goal to control the motion of the vehicle as a whole, the driver is still in the loop to assist with this and the pod-level control is there just to assist the driver. Additional iterations of control for this vehicle may very well employ vehicle attitude control through the use of an inertial measuring unit (IMU) which measures vehicle heading. Once both control systems (pod level and vehicle level) are studied, tested, and calibrated, it would be conceivable to place them both on the vehicle. This would provide control at both the pod-level and vehicle-level. Ideally, both systems would provide complementary aspects to the control, the pod-level providing quick response to commands and disturbances and the vehicle-level maintaining the ultimate goal of controlling vehicle attitude

## 2. Hardware Identification and Set-up

### 2.1 Vehicle Design and Architecture

The basic design of the chassis and pod is shown in *Figure 2-1*. This figure includes some basic dimensions of the vehicle as well as the vehicle coordinate system that were employed in the vehicle software and simulation. These dimensions were based on a Quality Functional Deployment (QFD) created by the senior engineering class of 2007 and will be discussed further in Section 2.1.1. The dimensions shown in *Figure 2-1* are also relevant to the simulation which is discussed in detail in Chapter 5.

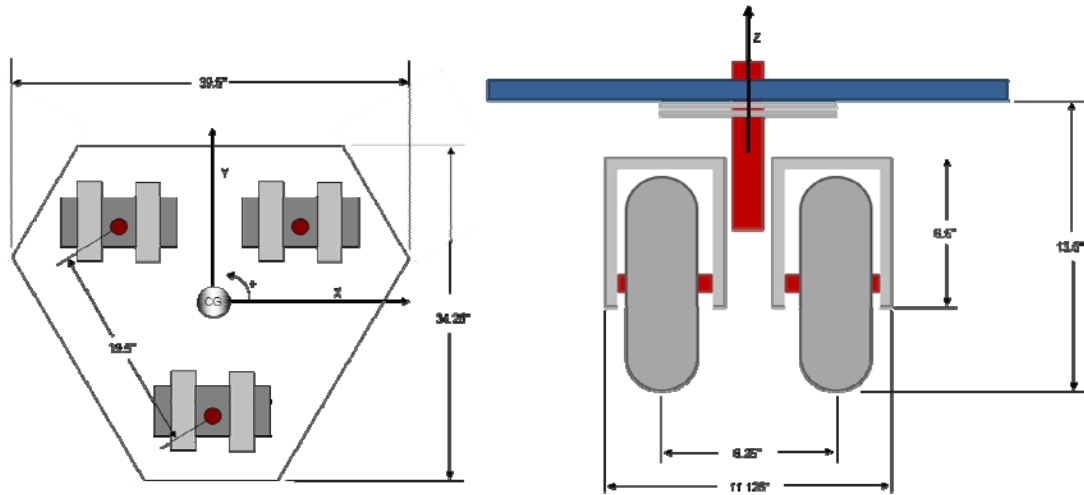


Figure 2-1 Approximate Dimensions of the Chassis (left) and Pod (right)

#### 2.1.1 Overall Vehicle Design (Mechanical)

The mechanical design of the vehicle was started and completed between January and August 2007. The students of the mechanical engineering senior design class used a QFD to come up with specification targets that the vehicle should meet [12]. QFD is a commonly employed engineering design tool that aids in the initial development of a

product. Further details of the QFD process can be found in the tutorial shown at [www.webducate.net/qfd/qfd.html](http://www.webducate.net/qfd/qfd.html) [12].

As is practice in the QFD process, target specifications were benchmarked from other existing robots that perform similar function to those desired of the robot under consideration. An analysis of the priorities of the robot helps decide the major dimensions, materials, cost, and overall performance. Although a QFD was utilized for this project, further consideration of the dimensions and performance characteristics was taken as needed to allow for better control over the vehicle. The main specifications from the initial QFD are listed below [1].

- Ground clearance: 4 inches
- Wheel diameter: 7 inches
- Caster distance: 0.5 inch
- Maximum speed: 10 mph
- Center of Gravity height: 3.5 inches
- Height of vehicle: 12 inches
- Maximum step height: 2 inches

With the main specifications listed above, preliminary renderings and sketches were completed with CATIA, a 3D modeling software. The resulting CAD model is shown below in *Figure 2-2*

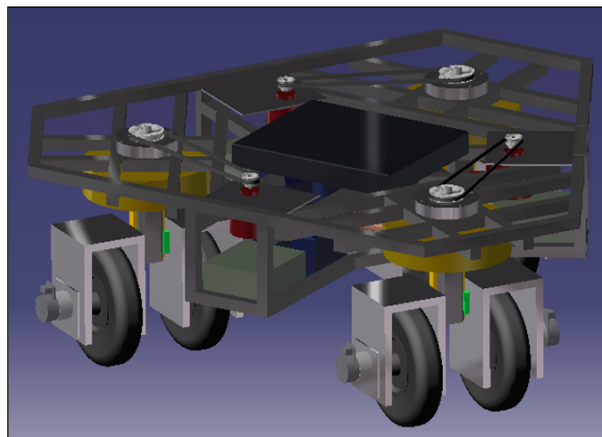


**Figure 2-2 CATIA 3D Rendering of the ODV [1]**

Figures 2-3 and 2-4, show the results of the construction as completed by the senior design class of 2007. Figures 2-3 and 2-4 shows the body-fixed coordinate system employed on the vehicle which was also shown in Figure 2-1.

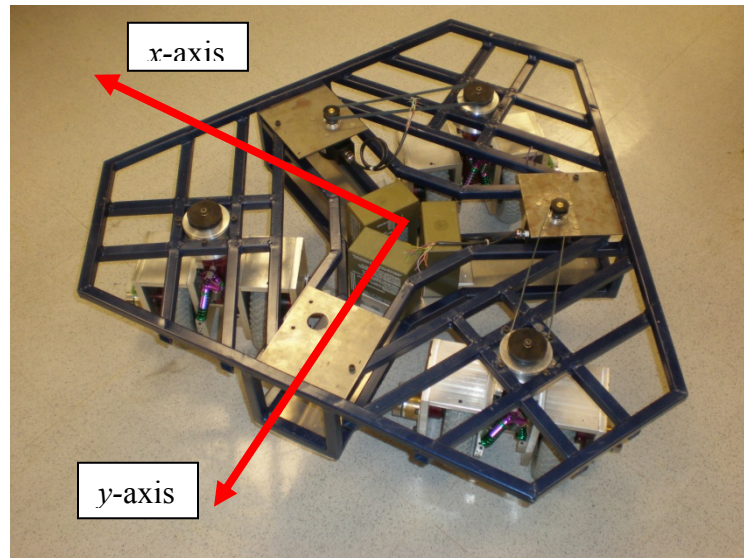


Figure 2-3 Isometric View of Mechanical Assembly with Body Coordinate Frame [1]

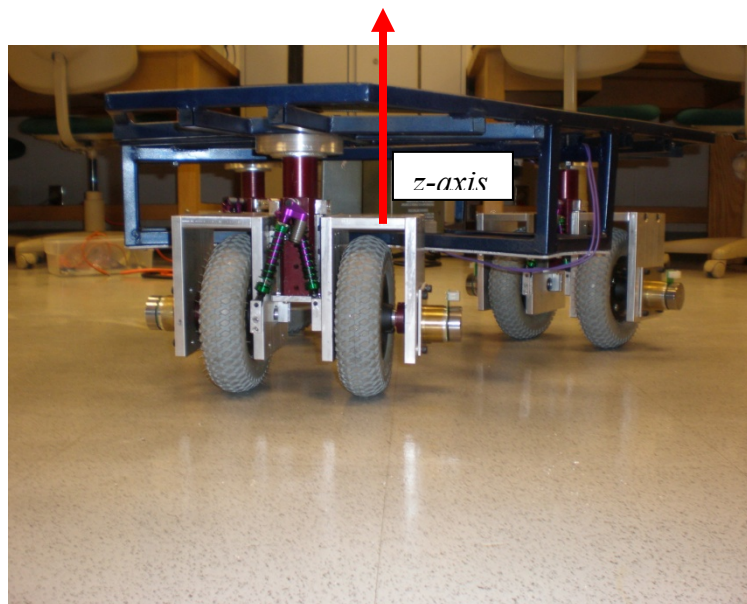


Figure 2-4 Front View of Mechanical Assembly with z-axis [1]

This document concentrates primarily on the dynamic modeling and control of the vehicle as it was received. Physical dimensions of the device itself including parameters, such as caster offset, all affect the control design and ultimately the control gains. Although the structure of the control strategy does not change with varying the physical dimensions of the vehicle, the control effort and control timing would have to be re-calibrated to suit the new physical parameters.

For example, caster distance and pod spacing can have a great effect on the control design. Decreasing the caster distance or offset will make it easier for the vehicle to complete turns. The pods require less net torque from the motors to complete turns and the lower offset also makes the pods respond quicker to inputs. Increasing the caster offset makes the opposite true. The vehicle will become more stable while traversing in a straight line, but it will make turns more difficult to complete.

Finding the appropriate amount of caster offset, wheel spacing, and pod spacing is a balancing act that depends on requirements from the user. No one particular value is a necessity or a direct requirement for the proper operation of the vehicle. Picking these values is a result of a study done outside of this project and, therefore, is beyond the scope of this document.

Physical parameters such as ground clearance, center of gravity height and ground clearance are parameters chosen to be specific for the vehicle's use. The ground clearance is chosen to ensure the vehicle can clear certain size obstacles that could be present on the surfaces on which a soldier decides to operate the vehicle. The vehicle is designed to be operated in urban and desert environments. In these environments, it is

not expected to come across obstacles that are taller than an average red brick lying on its side.

The overall height and center of gravity height along with overall width of the vehicle go hand in hand with each other. The maximum height of the vehicle was chosen as an acceptable height which could still roll under the military Humvee having a standard ride height of around 16 inches [13] [14]. The extra space could serve as a safety factor for approach and departure angles that could be an obstacle offered by the terrain.

A lower center of gravity height is better for the rollover performance and weight transfer of the vehicle. Unfortunately, it is difficult to keep center of gravity height low with a project that is also dependent on ride height clearance. The center of gravity height is greatly dependent on the items attached to the chassis that often times cannot be avoided. The items on the vehicle are necessary for the proper function of the vehicle and so decreasing weight in one area and adding it in another is not always easy. Instead, the mounting location for each component was kept as low as possible in the chassis in an attempt to reduce the height of the center of gravity. For example, the batteries, which are among the heaviest and most dense components, are mounted to the floor pan of the vehicle.

Other dimensions like wheel diameter were chosen based on their effect on other key parameters while keeping cost in mind. The wheels could be considered off-the-shelf items thereby reducing cost. Therefore, picking a wheel size was done by picking one that will give the vehicle the ride height it needs, allows the vehicle drive over obstacles, and maintain a standard wheel size.

### 2.1.2 Overall Vehicle Design (Control)

This section touches briefly on the control strategy used on the vehicle and the ways that the hardware carries out the demands of the control system. The control system, from the software point of view, will be discussed in more depth in Chapters 3 and 5. Chapter 3 discusses the architecture of the software (LabVIEW) and the control system programming which in turn instruct the hardware. Chapter 5 discusses the architecture of the control system as it pertains to the simulation. The control strategy from here forward follows the structure laid out in *Figure 2-5*. Keeping this figure in mind may prove helpful as one considers the actual hardware and software on board the vehicle.

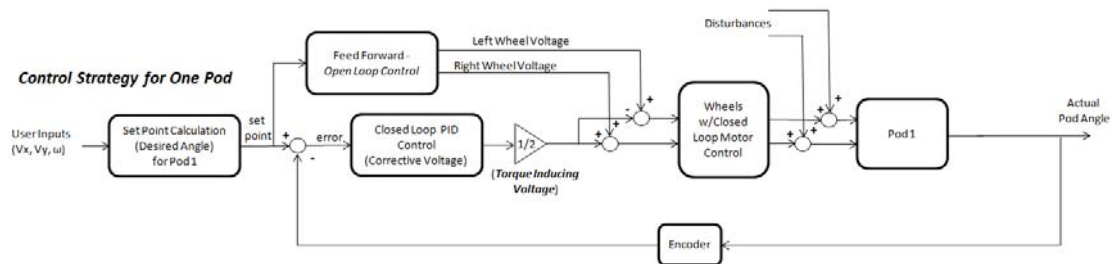


**Figure 2-5 Overall Vehicle Control Block Diagram w/Control System**

The initial inputs from the user are the vehicle's desired translational velocity (x- and y-components) and its desired angular velocity. From experience it has been determined that a kinematics-based open-loop control system is insufficient to allow an operator to drive the vehicle at even moderate speeds. Specifically, the human in the loop is sufficient to achieve a desired velocity magnitude, but the slippage and scrubbing experienced by each of the six wheels makes achieving a commanded direction impossible at all but the slowest speeds without feedback. Therefore, the control strategy depicted in Figure 2-5 has been adopted. This strategy attempts to control the orientation

of the individual pods as a means for achieving an orientation of the overall vehicle. The speed control of the wheels themselves is implemented by the motor controllers which were bought off-the-shelf.

The pod-control strategy specifically attempts to control the angle of a pod with respect to the chassis. A benefit of this approach is that there is no need to know the orientation of the chassis which would require a potentially expensive inertial sensor. Also, the pods will respond much more quickly to control system inputs since they are closer to the application of the control forces and since the inertia of a single pod is significantly lower than that of the entire vehicle. The control strategy includes a feedforward component based on the vehicle kinematics as well as a feedback component that is based on the error between the commanded and actual pod angle. Each component of the control has a complementary effect. The feedforward portion of the control has no dynamics and, as a result, is very fast. Also, since the overall dynamic relations are nonlinear, the feedforward term is expected to get the output close to the command so that for small errors, the system behaves approximately linearly. The drawback of the feedforward control is that it does not account for errors in the model and disturbances, specifically which come from the slipping and scrubbing of the tires. These errors and uncertainties are, therefore, corrected for by the feedback portion of the control. The feedback portion is implemented as a dynamic PID controller which is more robust, but slower than the feedforward controller. Recall that further details concerning this control strategy are discussed in Chapter 3 and Chapter 5.

The overall vehicle system is made up of several smaller components that help the vehicle run as the user wishes. This is depicted in *Figure 2-6*.

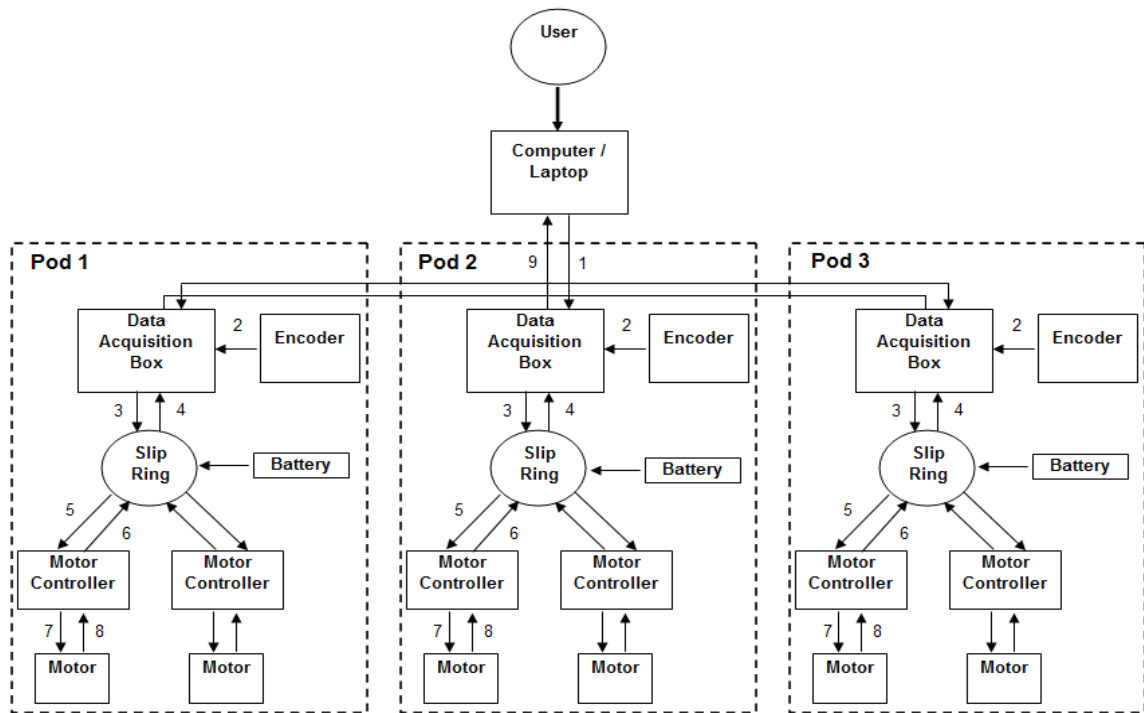


**Figure 2-6 Top-level Vehicle Wiring Schematic**

In order to provide further clarification of the layout of the vehicle, *Figure 2-6* shows the overall wiring schematic for the vehicle. The schematic does not show every distinct wire on the vehicle. That information will be discussed in the wiring section, 2.6.4. Instead, the figure shows the overall direction of signal flow between each of the components. Each of the wiring avenues are labeled with a number for reference. *Table 2-1* briefly describes each of the numbered pathways. Sections 2.3 through 2.6 discuss the hardware used on the vehicle in detail.

All of these components, both hardware and software, help the vehicle run with closed-loop control. First and foremost is the laptop. The laptop receives wireless signal inputs from the driver and runs the software used for control of the vehicle. The software is fully customizable and can effectively alter how the vehicle drives or behaves within the limitations of the hardware. This software can calculate things like error and control

effort, monitor current vehicle status such as individual wheel speeds, and send out control signals to the motors such as a voltage, direction, or disable commands.

1	Signals calculated using LabVIEW, as a result of user inputs or vehicle feedback, are sent to the DAQ cards
2	Signals from the encoder are sent to the DAQ cards. These signals help track the angular position of the pods
3	Motor voltage, disable, and direction signals are sent from the DAQ cards to the slip-rings. Power supplied by the batteries is also routed through the slip-rings.
4	Hall-effect sensor counter signals are sent from the slip-rings to the DAQ cards. These signals help track wheel angular velocity and angular acceleration
5	Motor voltage (speed command), disable, and direction signals come through the slip-rings and to the motor controllers. Battery power supply wires are routed from the slip-rings to the motor controller
6	The motor controllers send a pulse train from the Hall-effect sensors to the slip-rings
7	Closed-loop voltage commands are sent from the motor controller to the brushless DC motors. This voltage physically drives the motors
8	Pulse trains generated by the Hall-effect sensors are tracked by the motor controllers
9	Communication signals translated by the DAQ cards from physical signals are sent back to the computer. LabVIEW processes these signals and uses them for future calculations

**Table 2-1 Description of Wiring Pathways in Figure 2-6**

The data acquisition cards, which are connected to the computer via USB, send and receive communication signals given by the software. They serve as the interface between the software and the sensors and actuators on the vehicle. For this vehicle, the data acquisition cards will send desired wheel speed, direction, and disable commands to the motor controllers. They receive an encoder signal which is the angle of the pod in relation to the chassis. Lastly, they receive counter signals from the Hall-effect sensors in the motors. This counter signal can be used to calculate actual wheel speeds

The wires running from the encoders to the data acquisition cards are one piece and do not pass through the slip-rings since both data acquisition cards and the encoders are attached to the chassis (not the pods). Wires running from the data acquisition cards and going to the motor controllers must first pass through the slip-rings. This is because

the motor controllers are attached to the top faces of the pods which must be able to rotate through a full rotation.

The motor controllers receive the desired wheel speed, direction, and disable commands from the laptop through the data acquisition cards. The controllers also receive data from the Hall-effect sensors in the motors. Based on the angular speed of the motors, the voltage command from the laptop (which can represent desired speed or torque), and disable command, the motor controllers controls the motor's acceleration or deceleration. It does this since the motor controller will be run in closed-loop speed control mode. More information on the modes will be given in Section 2.4.

The encoders are attached to the frame or chassis of the vehicle and have a pulley attached to the input shaft. At the top of the pod is another pulley. The pulley ratio between the encoder and the pod is 1:1 which will allow direct angular rotation tracking of the pod in relation to the chassis. The encoders help to track error in the control algorithm and, therefore, are instrumental in the control of the vehicle.

The motors are DC brushless and are the last element on the vehicle to receive signals. They operate purely on three voltage excitation signals, one for each of the three motor windings. The motors also have three Hall-effect sensors which output a pulse train where each pulse represents an incremental change in motor shaft position. The motors can be commanded to operate in reverse, and by observing the relative phase of each of the Hall-effect sensor outputs the direction of motion of the motors can be sensed. Although the Hall-effect sensors output only position of a motor shaft, the speed of a motor can be calculated with known elapsed time and the angular position signal. In other words, the frequency of the pulse train indicates angular speed.

## 2.2 Chassis

There were several limitations handed out to the initial student design team when designing the vehicle. These limitations drove considerations like the choice of materials utilized on the vehicle. Steel was chosen as the material for the construction of the chassis since it is cheap while still maintaining a fair amount of rigidity. Lastly, students are typically new to manufacturing and activities such as welding. Steel is one of the easier materials to weld together and provides a good testing ground for students to practice. In short, it is a good all-around material for a structural application like this. Other materials such as titanium, aluminum, or carbon fiber could have been used to cut down on mass, but they come at a greater cost to the consumer. These materials are also more difficult to employ for construction. Carbon fiber in particular has to be molded and requires special consideration to the direction and placement of the fibers. Future iterations of the vehicle may explore the use of these other materials in order to take advantage of their mass advantage.

The overall layout of the chassis is such that it allows three pods set 120 degrees apart. The overall dimensions of the chassis are driven by the features needed for the vehicle. It leaves just enough space for things such as the pods, slip-rings, encoders, laptop, data acquisition cards, and batteries. Other features such as cameras could be added, but likely would need to be added to a separately built stage. For now, this vehicle serves as a proof of concept.

## 2.3 Pod Design

The structure and layout of each pod were chosen as to allow independent vertical movement between the wheels. An independent suspension was chosen since it allows better traction and control over the position of the pod. If a solid type axle had been used between the wheels, there would have been a potential for one of the wheels to lose traction over uneven terrain. Complete loss of traction on just one of the wheels would prevent the pod from being able to effectively steer. Furthermore, losing traction on one or more of the wheels reduces the amount of power that can be applied to the ground and, therefore, will reduce velocity and or acceleration of the vehicle. Lastly, if the power cannot be effectively transmitted to the ground, then the control system will not be able to work as designed. A sketch of the suspension and pod design that illustrates how the wheels can move independently of one another is shown below in *Figure 2-7*.

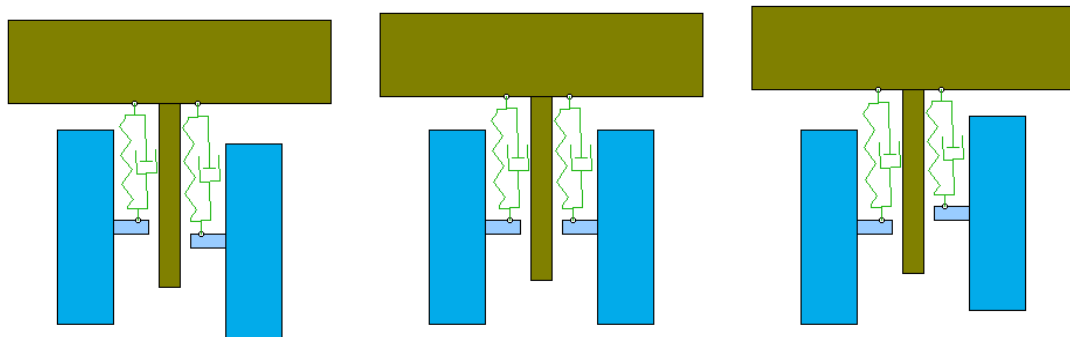


**Figure 2-7 Pod Design and Suspension Layout (suspension movement shown) [1]**

*Figure 2-8* shows the actual pod assembly and references the “U” shape, Wheel Bearings, Top Face, and Motor Controllers.

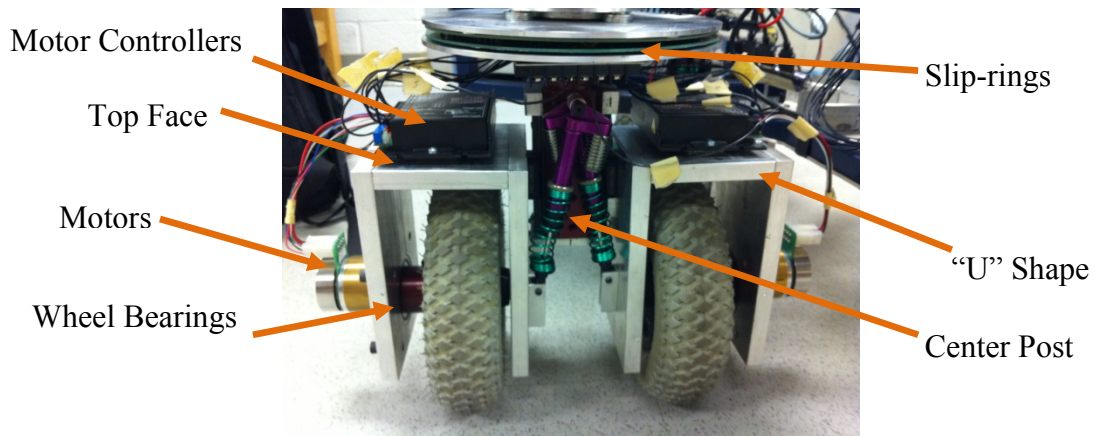


**Figure 2-8 Completed Pod Assembly**

The center post of the pod is constructed of steel with two linear bearing tracks mounted on either side. Mounted to the bearing tracks are three aluminum plates assembled in a “U” shape. Either side of the “U” serves as a mounting point for the wheel’s axle shaft and bearings. The aluminum plate closest to the center post is mounted to the linear bearing. It is this linear bearing that allows vertical movement between the aluminum plates and the steel center post.

The center of the axle is drilled out to allow the gearbox and motor assembly to couple with the axle. A set screw within the wheel axle prevents any angular slip between the wheel axle and the gearbox shaft. The gearbox also mounts to an aluminum plate which in turn mounts to the outer side of the “U”. The motor mounts to the opposite side of the gearbox and completes the motor and gearbox assembly.

The top face of the “U” shapes serve as mounting locations for the motor controllers. Each motor controller is secured to the top of the “U” shape with Velcro. This allows a cost effective and easy mounting structure for the controllers.

## 2.4 Motor Controllers

The motor controllers relay information and control signals between the data acquisition cards and the motors. They receive the motor control signals including an analog speed or torque command, as well as a disable and direction bit. The various potentiometers and switches on the controller can alter control modes, top speed, and acceleration profiles of the motors and ultimately the vehicle. The controllers also read the motor Hall-effect sensors for the purposes of closed-loop control and transmit these signals so that they can be used outside of the motor controllers.

There are three Hall-effect sensors which track the position of the motor shafts. Utilizing three of the Hall-effect sensors yields higher fidelity than using just one or two. Observing the phase between multiple Hall-effect sensors also allows determination of a motor's direction of motion. *Figure 2-9* shows the controller used on the vehicle.



Figure 2-9 1-Q-EC Amplifier DEC 50/5 Controller [15]

The controllers are manufactured by Maxon and offer three modes of operation which include open-loop speed control, closed-loop speed control, and current control (torque control).

A speed control mode was chosen because it aligns with the commands being sent to the vehicle by the user (translational and angular velocity). More specifically, closed-loop speed control was chosen versus open-loop speed control because it is more robust to disturbances and to variation amongst the different motors. Torque control was not selected since it was difficult to command a given velocity. Instead, torque control only commands the torque output to the wheels. While torque control provides consistent acceleration profiles on one surface, it does not do so across different surfaces. Closed-loop speed control will maintain consistent performance for a variety of surfaces within reason. Consistent performance makes the vehicle more predictable to the user and easier to model by simulation. This mode can be set by adjusting the six switches on the controller. The switch configuration is shown in *Figure 2-10*.



**Figure 2-10 Switch Configuration for Speed Control [15]**

Although the above diagram shows the controller setting for the speed control operation of the brushless DC motor, the user can also adjust switches 2, 5, and 6. The number 2 switch controls the gain of the motor with the off position being the highest gain. The gain controls how the vehicle accelerates. The higher the gain, the quicker the vehicle will reach top speed. The top speed will remain the same no matter which position the gain is set. The number 5 and 6 switches control the top speed of the motor.

These switches can do this as they control the maximum allowable RPM. The highest speed the motor can attain is achieved by setting switches 5 and 6 to the off position.

Acceleration profiles, top speed, and available torque are all parameters of the motor that can be adjusted by the potentiometers on the controller. Depending on which mode the controller is in affects which potentiometer becomes active. For instance, when in closed-loop speed control mode, the gain potentiometer becomes active. This potentiometer is able to change how the vehicle accelerates [15].

## **2.5 Maxon EC 45 Flat Motors**

Providing the power and steering capabilities of the vehicle are the six brushless DC motors. Two motors, one on each side of the pod, connect to the drive wheels and ultimately allow for translational and rotational movement of the pods. By providing the same voltage and direction to the motors, they will move the pod in only a translational direction. A difference in the voltages supplied to the motors can result in either pure rotation or a combination of rotational and translational movement. Pure rotation will result if the voltages supplied to the motors are equal in magnitude but in opposite directions. Voltages in the same direction but different in magnitude will result in both translational and rotational movement of the pods. It is the control of these scenarios that move the individual pods that in turn result in the desired movement of the chassis.

The DC motors are also manufactured by Maxon, each produces approximately 50 Watts of power. The particular motors used are the EC 45 Flat Brushless Motor models. Each motor has three windings and three Hall-effect sensors. Hall-effect sensors allow the angular displacement of the motors to be tracked and thus allows for

consistent control of the speed of the vehicle. It also yields more consistency between each of the motors which is important since the vehicle uses six of the motors and relies on a difference of velocity to complete turns. *Figure 2-11* shows the motors used on the device [16].

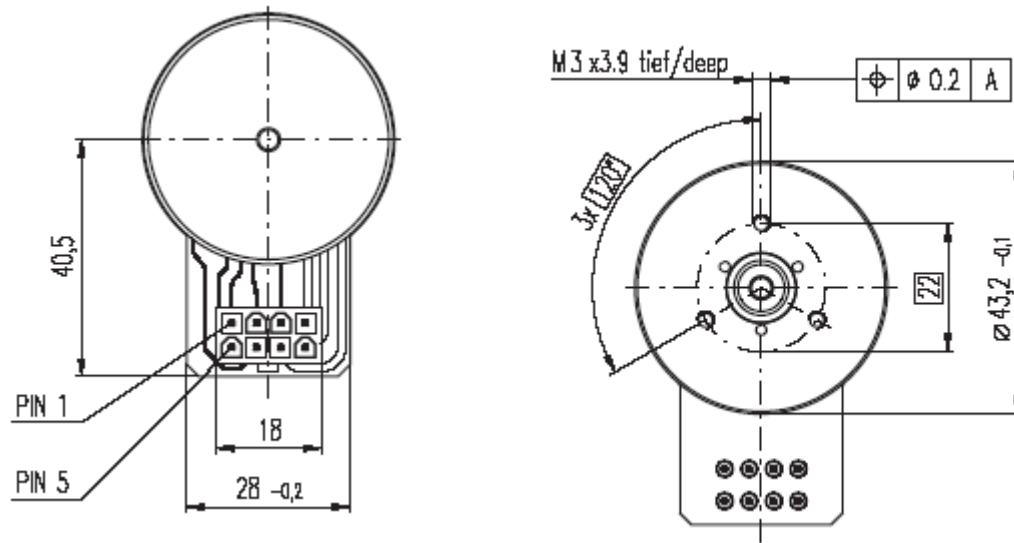


Figure 2-11 EC 45 Flat Brushless Motor [16]

## 2.6 Slip-rings, Data Acquisition Cards and Wiring, and Encoders

### 2.6.1 Slip-rings

Providing the bridge between the motor controllers and the data acquisition cards are the slip-rings. The slip-rings allow the transmission of information and power to and from the pods while allowing them to rotate through a full range of motion. The only other way that the pods could turn 360 degrees without tangling the wires would be by wireless communication. This is a very important aspect for the vehicle. In order for this vehicle to be considered a true omni-directional vehicle, the pods need to be able to move

through 360 degrees of rotation. This prevents the vehicle from getting stuck in tight surroundings and allows it to maneuver through difficult areas.

There is one slip-ring, shown in *Figure 2-8*, located at the top of each pod and each is constructed out of circular shaped aluminum plates. Sandwiched between the aluminum plates are two circuit board-like circular structures. These circular circuit board-like structures are what allow electrical connection throughout a 360 degree rotation of the plates relative to each other.

Molded into the bottom circuit board are 16 brass rings thus allowing 16 separate electrical signals. The top circuit board remains stationary relative to the chassis and contains gold leaves which provide the physical connection to the bottom 16 rings directly below. These gold leaves are shaped like a “V” and are fairly flexible. The flexibility and shape of the leaves generate a spring force that keeps the connection between the top and lower plates. Even if the gap between the plates were to vary, the spring force in the leaves maintains the electrical connection. A circular piece of vinyl, with a sticky back, was cut out and placed between each of the rotating aluminum plates and the corresponding circuit-board. This was done to prevent the aluminum plates from causing a short across different channels of the circuit boards.

After installing the slip-rings, the pods could then be put into their respective places in the framework. Here, the location of the lower half of the slip-ring becomes important as this is what can either create or break the electrical connection in the slip-rings. If the gap between the plates of the slip-rings is too large, the electrical connectivity could be affected. Similarly, if the gap is too small, there is increased

friction and a risk of breaking the gold tabs. Breaking the tabs off of the slip-rings will result in a loss of electrical connection.

### **2.6.2 Encoders**

The optical encoders, belts and pulleys are connected to the top side of the vehicle. The pod encoders generate an output that is similar to that produced by the Hall-effect sensors but are unable to determine the angular position. The angular position of an encoder can be determined using a system of wires that switch between high and low voltage signals. The low voltage is considered to have a value of zero (0), while the high voltage has a value of one (1). The encoders specifically are 10-bit (employ 10-wires) such that each revolution can be split into  $2^{10}$  increments. By comparing the string of values being generated by an encoder to a matrix of combinations of zeros and ones, a specially written VI can output the current angular position of a pod.

For packaging reasons, each of the encoders is attached to the pods by way of a belt and pulley mechanism. In order to make the software run correctly and easier to implement, there had to be a one-to-one ratio between the encoder pulley and the pulley on the pod. This ensures that the encoders properly track any movement of the pods. This is very important for the control strategy of the vehicle. Once the pulleys were on, they were adjusted so that all the pods had a consistent origin.

If a theoretical coordinate system were placed at the center of gravity of the chassis, shown in *Figures 2-3* and *2-4*, the positive *y-axis* would point at the front of the vehicle. The positive *x-axis* would point from the right side of the vehicle. The positive *x-axis* is synonymous with a pod angle measurement of zero (0) radians, in relation to the chassis (as read from the encoders). The pods were initially aligned so that the wheels of

each pod are facing forward when they are parallel with the positive  $y$ -axis thus making the pods have an angle of  $\pi/2$  radians in relation to the chassis. This is the default forward direction as used by the mathematics in the software.

For stability purposes, the front of the vehicle was taken to be one of the flat faces of the framework. This means that two pods will be leading rather than trailing. It is believed, however, that the vehicle may be more maneuverable if two of the pods are trailing.

The encoders were mounted to a special plate which can slide in relation to the chassis. The mounting plates enable the tension to be properly set on the belt running between each of the encoders and pods. The remaining hardware is the data acquisition cards. These were placed on the lower plane of the chassis with Velcro and labeled corresponding to their respective pods.

The batteries were similarly set in the floor pan of the vehicle. All three wire sets carrying power to each of the pods had to have their wires soldered into a plug-in connection. A fuse was introduced in line with the wiring between the motor controller and the battery to protect against the possibility of over-current or over-voltage. Three brackets were created and bolted to the chassis which served as the mounting method for the plug-in connections to the floor pan.

### **2.6.3 Data Acquisition Cards**

There are three data acquisition cards (DAQ cards) attached to the chassis; one for each pod. There is a USB connection between the laptop and each DAQ card which allows communication with the LabVIEW software. In this particular setup, LabVIEW is sending communication signals to the DAQ card, and the card change these

communication signals into a physical voltage. The outputs are considered either digital using TTL logic (0V for false and 5V for true) or are analog where the voltage is proportional to the command from LabVIEW with a range of 0V to 5V.

For each pod, LabVIEW sends five communication signals to the DAQ cards which are represented by five channels. Three channels are digital and two are analog. Two of the digital signals are used to change the direction of each wheel. The last digital signal is used to simultaneously disable both wheels on a pod. The analog channels are used to send voltage signals to each wheel which in turn control the velocity of the wheels. Here 0V is a command of no motion and 5V represents maximum motor speed.

The last function of the DAQ cards is to receive physical signals from the components on the vehicle. From there, the DAQ cards change those to a communication signal LabVIEW can interpret.

In this particular set-up, the encoders and the motor controllers send signals to the DAQ cards. Due to the limited amount of digital channels, all 10 wires from each encoder were wired to analog channels. It is acceptable to run digital signals on an analog channel because the software will not be able to detect the difference. A low signal (0V) or a high signal (5V) can still be interpreted as false or true, respectively, on an analog channel. The encoders receive their power from the DAQ cards.

The motor controllers send a pulse train signal, generated by the Hall-effect sensors in the motors, to the DAQ cards. The DAQ cards are able to count the pulses and use an internal timer to track the velocity of the wheels. Though there are three Hall-effect sensors, only two are utilized. This is again due to the limited amount of digital channels. Unlike the encoders, the Hall-effect sensors need to be wired to digital

channels. This is due to the DAQ cards only being able to count the pulse trains on digital channels. Only the digital channels have counting capability. A minimum of two pulse trains are needed in order to detect motor direction.

Figure 2-12 shows a data acquisition card and the various pins available for use on the device. National Instruments makes several Data Acquisition Cards where the major differences are the number and quality of the channels in the card. The DAQ card used in this project is model number USB-6215. A detailed description of the wiring layout and channels as used for this project is described in the wiring section, 2.6.4.

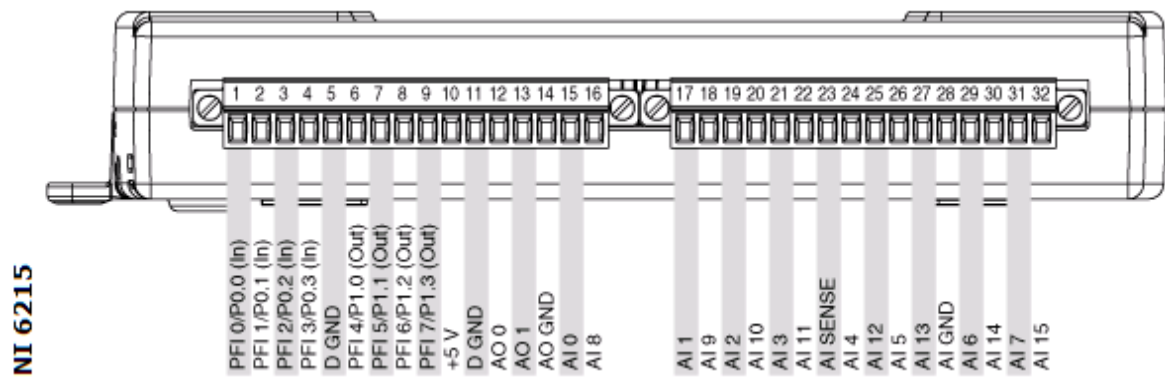


**Figure 2-12 Summary of Data Acquisition Card Pin Layout [17]**

## 2.6.4 Wiring

The batteries supply power to motor controllers and ultimately the motors. The battery leads had to be run through the slip-rings since the batteries are mounted in the floor pan of the vehicle and the motors and motor controllers are mounted to the pods which can rotate. The data acquisition cards, encoders, and receiver for the vehicle controller are all powered by the laptop. The receiver is part of the game pad controller system. The game pad transmits signals to the software through the receiver. The game pad will be discussed in detail in Section 2.8

The wiring between all the physical hardware mounted to either the chassis or pods is responsible for all power and signal-level communication. For a given pod this includes the two motors, the pod encoder, the DAQ card, the battery, and the slip-ring. The brushless DC motor has eight pins all of which are connected to the controller. They are conveniently numbered Pins 1-8. A summary of the pin layout is listed in *Table 2-2* below [16].

Pin #	Connection
Pin 1	Hall Sensor 1
Pin 2	Hall Sensor 2
Pin 3	4.5 ... 18 VDC
Pin 4	Motor Winding 3
Pin 5	Hall Sensor 3
Pin 6	Ground
Pin 7	Motor Winding 1
Pin 8	Motor Winding 2

**Table 2-2 Motor Pin Summary [16]**

The pins of the motor are laid out in two rows of four. The geometry of the pin layout is more than likely what controlled the pin designation. For instance, Pins 1&5 for the Hall Sensor 1 and Hall Sensor 3 are not near each other numerically, but they are physically due to the pin geometry. The pin layout can be seen in *Figure 2-13*.

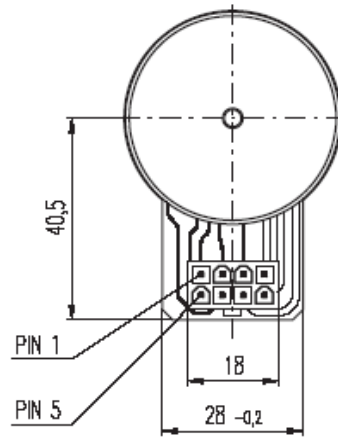


**Figure 2-13 DC Motor Pin Layout [16]**

The wiring between the DC motor and the controller is illustrated below in *Figure 2-14*.

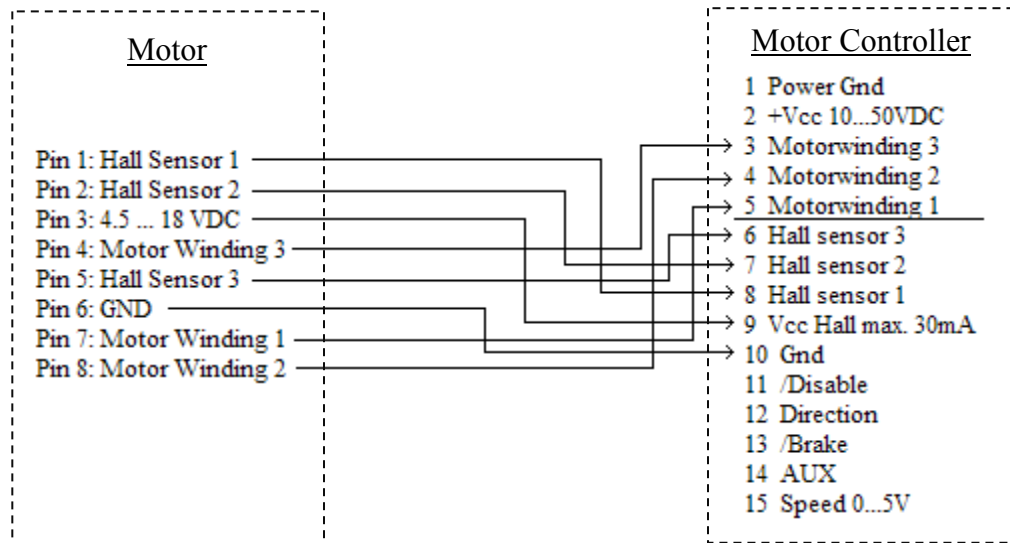


**Figure 2-14 Wiring diagram between the DC Motor and Controller**

The remainder of the wiring is between the pod encoder and the DAQ card and between the motor controller and the DAQ card. The best way to explain this wiring is through the simplified wiring diagram shown in *Figures 2-15 and 2-16*.

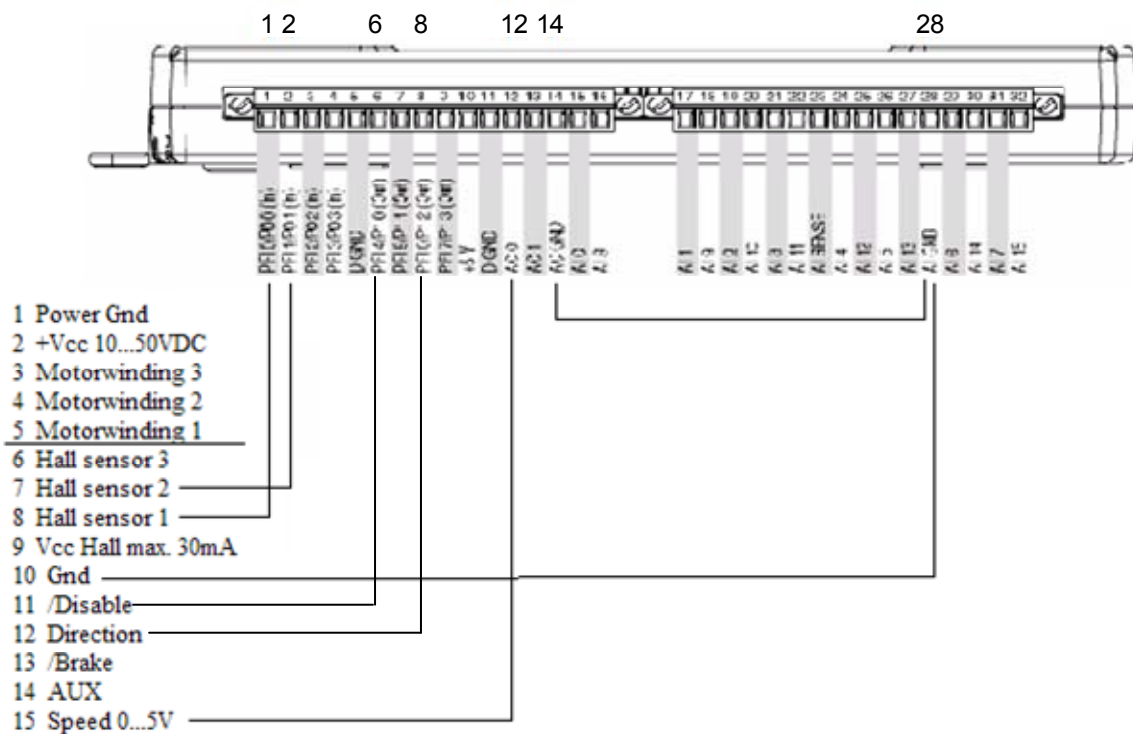


Figure 2-15 Wiring Set-up between Acquisition Card and Motor Controller

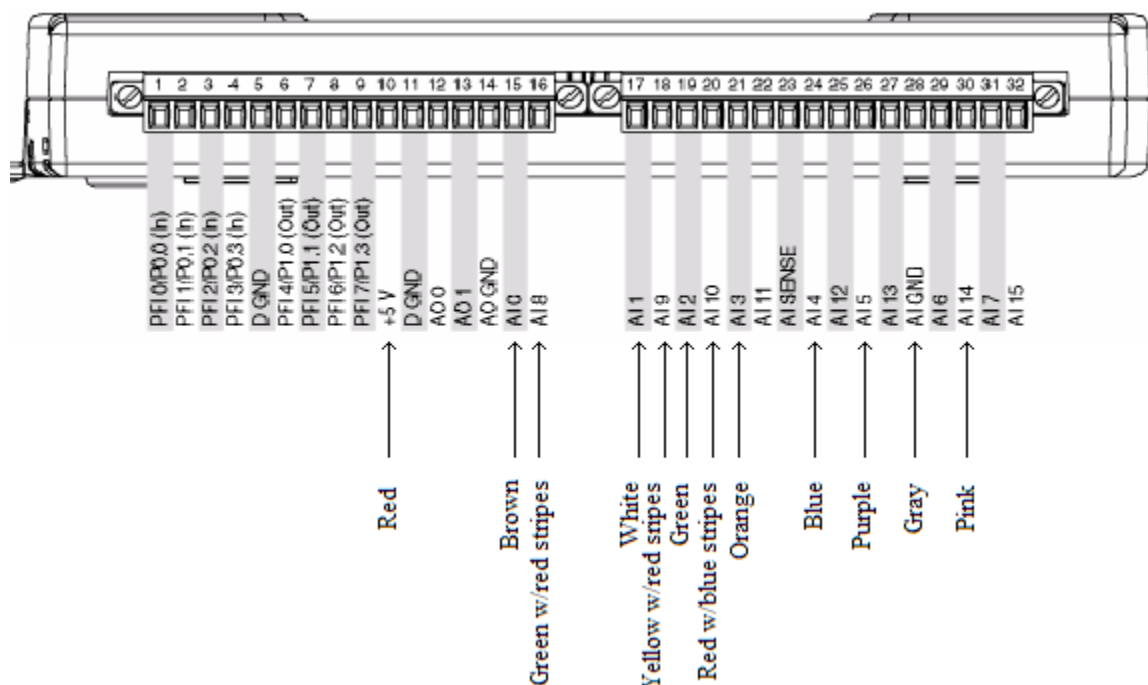


Figure 2-16 Wiring Set-up between Acquisition Card and Encoder

The last item is the wiring of the slip-rings. The slip-rings allow a wiring connection even though the two items being connected may move (rotationally) in relation to each other. For each pod, the DAQ card as well as the pod encoder is attached to the chassis of the vehicle. Therefore, the encoder signals do not have to pass through the slip-ring. The motor controllers (2x) are attached to the top of the pods and, therefore, need the slip-ring to complete the connection from the pod to the DAQ card. The power source for the controllers, since it is coming from the chassis, needs to go through the slip-ring as well. The quantity of each type of channel (analog vs. digital) is limited by the DAQ card. In general, the total number of channels used on the vehicle was limited by the slip-rings. A summary of the channels being controlled, the type, and whether or not it can be shared by the two controllers at the same time is shown in *Table 2-3*.

Used by both controllers	Type	Used by separate controllers	Type
Power +		5V Control	Analog / O
Power – (ground)		Direction	Digital / O
Analog Ground	Analog	Hall Sensor 1: Motor 1	Digital / Ctr.
Digital Ground	Digital	Hall Sensor 2: Motor 1	Digital / Ctr.
Brake	Digital / O	Hall Sensor 1: Motor 2	Digital / Ctr.
Disable	Digital / O	Hall Sensor 2: Motor 2	Digital / Ctr.

**Table 2-3 Summary of Pin Connections Passing through the Slip-rings**

## **2.7 Masses, Inertias, and Dynamic Characteristics**

Most of the mechanical aspects of the device were completed and built by prior senior design classes, but the masses and inertias of the vehicle components still needed to be captured for use in the design of the controller and construction of the vehicle simulation. The mass of the pod as an assembly and the mass of its components

(including the suspension components, two wheels and axles, the motors, and the controllers) all needed to be found and documented. Furthermore, the rotational inertias of the wheels and the completed pod also needed to be identified. The mass and inertia of the complete vehicle was taken only after the final layout and composition of the vehicle was determined. These parameters are important for the vehicle to be modeled and simulated. The simulation will be discussed in detail in Chapter 5.

The masses of the components were found by placing them on a digital scale. Finding the rotational inertias of the wheel assembly and completed pod was not as straightforward as finding the masses of the components. Since the exact make-up (density and geometry) was not known of the components, the rotational inertias needed to be found experimentally employing a multi-filar suspension [18] [19].

This encompasses suspending the assembly by two or more wires, inducing an initial rotational displacement, and letting the assembly oscillate freely. The resulting period of oscillation and the physical parameters of the experiment can be employed in Equation 2-1 [18] to estimate the moment inertia of the assembly.

$$J = \frac{WR_2^2 L_0}{4\pi^2 (L_0 + (R_2 - R_1)^2)} t^2 \quad (\text{Eq. 2-1})$$

The parameters in Equation 2-1 are shown in *Figure 2-17*.  $t$  is the recorded period of oscillation,  $W$  is the weight of object, and  $J$  is the inertia. For the pod assembly, only two wires were used in the experiment. The chassis inertia was measured using three wires, though the number of wires used to suspend the component or assembly has no effect on the measured inertia.

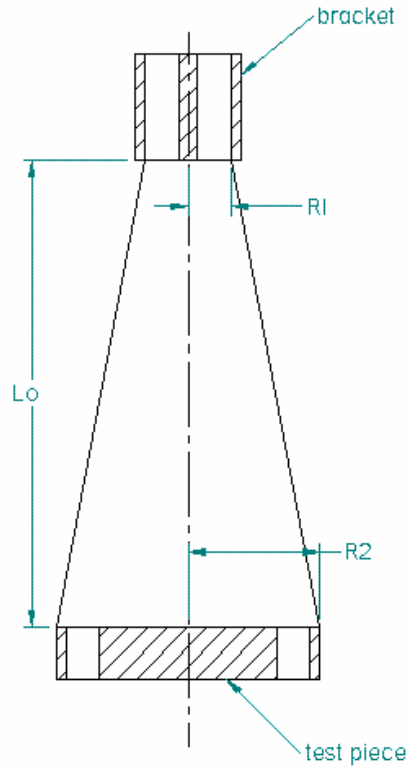


**Figure 2-17 Test Experiment for Determining the Moment of Inertia of an Object [18]**

*Table 2-4* includes the experimental inertias and masses of the various components.

	<b>Mass (kg)</b>	<b>Inertia (kg-m<sup>2</sup>)</b>
<b>Wheel, Axle &amp; Bearing Assembly</b>	1.012	N/A
<b>Wheel</b>	0.570	0.00204
<b>Pod Frame</b>	1.561	N/A
<b>Motor, Mount Plate, 4 Bolts, &amp; 4 Washers</b>	0.422	N/A
<b>Controller w/Wiring</b>	0.136	N/A
<b>Entire Pod</b>	9.705	0.07238
<b>Entire Vehicle</b>	55.000	21.80
<b>Chassis (w/o Pods)</b>	25.885	18.785

**Table 2-4 Summary of Masses and Inertias**

## **2.8 Human Interface and Control**

The PC laptop runs the vehicle software that carries out all of the complex calculations needed for controlling the vehicle. For this particular application, an IBM ThinkPad running Windows XP was chosen to run the software used for implementing the logic that controls the vehicle. The logic for interfacing with and controlling the vehicle is specifically implemented in LabVIEW. The LabVIEW software is well-suited to interfacing with physical hardware. Specifically, LabVIEW has a graphical interface that makes it easy to configure channels that send signals to, and acquire information from, the vehicle. The LabVIEW software also offers the ability to implement the algorithms needed for controlling the vehicle.

This particular project is not autonomous and, therefore, requires a human operator to give commands to the vehicle. Three specific options for wireless control of the vehicle were considered. The first was a personal digital assistant (PDA). The advantage of a small computer, like a PDA, is that it can serve multiple functions and can employ multiple different applications. For example, the PDA can allow the operator to take notes of what he/she saw while using the vehicle, or he/she can store data sets and even perform calculations with a program like Excel.

The downside is that it required a peer-to-peer internet or blue tooth connection. This type of connection is only good within a 30 foot radius. Often times the connections are intermittent and can be randomly and unexpectedly lost. The connections also take long durations of time to set up before becoming available for use. Setting up LabVIEW to interface with the PDA also took large amounts of time and was very difficult to initiate. This is not a problem if the software was adjusted one time and one time only.

However, one particular setup may not work for every operator and hence may require adjustment. Thus, for the sake of time, the ability to rapidly and accurately change the control software is an advantage.

Yet another drawback of the PDA is that it did not receive more than one input from the user. It only accepted one input from a stylus which was a decided disadvantage since the user would need to input speed and direction simultaneously. The user also has to take his/her eyes off the vehicle to make sure the stylus is in the correct position on the PDA screen. This is a severe disadvantage to a vehicle that is supposed to be operated at a high pace by a soldier that must be aware of his/her environment.

A second option was the use of a cellular phone. A phone like Apple's iPhone is able to share the screen and essentially take over the IBM laptop attached to the vehicle. Screen sharing software could be installed on both the PC and the iPhone and, therefore, allow total control over the PC. This would be a good approach if there had not been quality issues related to the screen sharing capabilities. Specifically, long lag time between inputs to the iPhone and communication to the laptop made it almost impossible to drive the vehicle without fear of crashing it. The phone and laptop connections also suffered from the same problems the PDA did. The iPhone required either a wireless internet connection (Wi-Fi) or bluetooth connection. As stated previously, a Bluetooth connection is still only good within a 30 foot radius. A Wi-Fi connection is undesired since the vehicle was intended to be used in an outdoor, possibly remote, setting where wireless service is often not available.

The third option was a gaming controller as seen on most modern gaming consoles such as PlayStation, Xbox or other similar consoles. The Xbox 360 controller

was chosen since Microsoft makes both the laptop operating system and the Xbox gaming console. This eliminated any compatibility issues between the controller and the computer. The controller works as a transmitter and the laptop as the receiver, therefore, this arrangement offers a more robust wireless connection that works very well up to a minimum radius of 100 feet. Another upside to the controller is that it allows the user to control the vehicle while maintaining visual contact 100 percent of the time. The soldiers of this generation also grew up playing Nintendo, PlayStation, or other similar consoles. The feel and control of this type of controller is completely natural to this generation of soldiers.

The raw signals from the game pad controller are also easily read in and can be easily manipulated within the LabVIEW software. Therefore, setting up and changing the configuration of the interface with the gamepad controller is quite simple. Lastly, initializing the connection between the LabVIEW software and the gamepad controller is fast enough that it is effectively instantaneous. *Figure 2-18*, below, shows the controller used for control of the vehicle. The button configuration will be discussed in Chapter 3.



**Figure 2-18 Xbox 360 Wireless Game Pad [20]**

### ***3. Software Description***

#### **3.1 LabVIEW**

LabVIEW is the software chosen to provide the interface between the hardware on the vehicle and the commands given by the driver. Within this program, users can freely set-up algorithms that control or monitor physical devices. These routines are termed Virtual Instruments or VIs for short. LabVIEW can specifically interface with these devices through channels of a DAQ card. These channels allow the ability to track various physical signals within a system or allow control signals to be sent to an array of actuators. In addition to monitoring signals from traditional sensors, LabVIEW can also read in real-time, signals from a user such as inputs from a gaming controller.

All of the abilities possessed by LabVIEW come together and allow for the creation of very specific and customizable environments (programs). Given that a user has an in-depth knowledge base of LabVIEW, users can set up new programs or edit existing ones fairly quickly. The reason is that the interface between the user and the computer screen is very intuitive for setting up programs. The interface utilizes a block and wire diagram which allows the user to easily see what he/she is doing on the screen. The blocks can be dragged and dropped from existing libraries and represent some calculation or process while the wires connect the blocks by simple pointing and clicking of a mouse and represent signal flow. It is this physical interaction that allows relatively quick and easy program set-up and editing. It especially provides a simple way to interact with the physical devices through a DAQ card where much of the underlying

hardware interface is handled at a high-level by specifying options from menus built-in to various existing blocks.

Within LabVIEW, there are two windows used to make VIs. The “front panel” is a graphical user interface used to either monitor or control something. Physically intuitive switches, dials, lights, graphs, or readouts can be arranged on this screen again by dragging and dropping elements from built-in libraries. It is more or less a quick summary of the physical device the user is trying to control or monitor. Using only this panel, the user sees the inputs, control or initial settings, and the outputs, such as pressure, velocity, position, voltage, etc. In the case of this project, the user cannot adjust anything on the front panel. The inputs, like speed, direction, orientation and emergency disable, come from the video game controller. The video game controller inputs, wheel speed, direction of the wheels, pod encoder angles, and emergency stop are monitored on the front panel.

Keep in mind that the front panel, in this case, was not designed to take inputs directly from the user since the vehicle will be in motion. Instead, the inputs come from the video game controller, thus allowing the driver to control the vehicle remotely. The front panel here was primarily used to monitor the vehicle’s operation and to assist with the design and debugging of the vehicle during development.

The “back panel” is a separate screen where all hardcoded elements, calculations, processes, and interactions with the DAQ cards are initiated and take place. The programmer can open up various channels with the DAQ cards and send the inputs from the front panel to the actual device. A programmer can either send the control signal from the front panel straight to the actual device, or the signal from the front panel can be

used as an input to some algorithm that calculates commands to be sent to any of the device's actuators.

The back panel is also the place to open up a channel on a DAQ card and pull in signals from the device. Similar to the signals sent to the device, the received signals can also go through some processing before being displayed on the front panel or sent to another portion of the back panel. For instance, data from the Hall-effect sensors on the motors is recorded as pulses representing changes in angular position, but is not of much use to the driver or to someone trying to model the vehicle. Therefore, an approximate derivative of the position is calculated to estimate wheel speed before being written to a file or displayed on the front panel. This information is much more valuable than the raw position data initially read from the sensor.

### **3.2 Overall Vehicle VI**

The front panel for the overall vehicle control program, shown in *Figure 3-1*, allows the user to monitor various aspects of the vehicle.

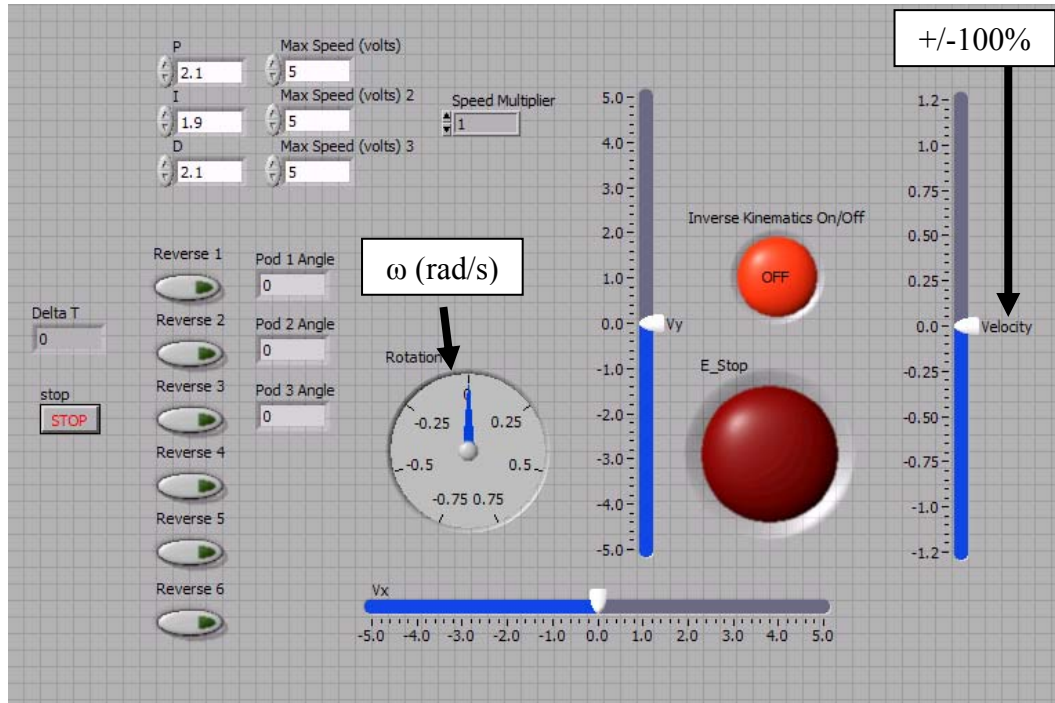


**Figure 3-1 Front Panel Screen Shot of the Overall Vehicle VI**

Five volts is the saturation limit on the brushless DC motors. Therefore, the voltage sent to the motors is held to within  $\pm 5.0$  volts by the DAQ card. The range of possible voltage inputs (from  $V_x$  and  $V_y$ ), from the driver, can be characterized by an imaginary circle centered at the origin of a coordinate system. This coordinate system, as mentioned in Chapter 2, has its origin located at the center of gravity on the vehicle and remains fixed to the vehicle. This “voltage circle” would have a radius of five units representing the five volts. The driver can send the vehicle any voltage combination as long as it is within this circle which is shown in *Figure 3-2*.

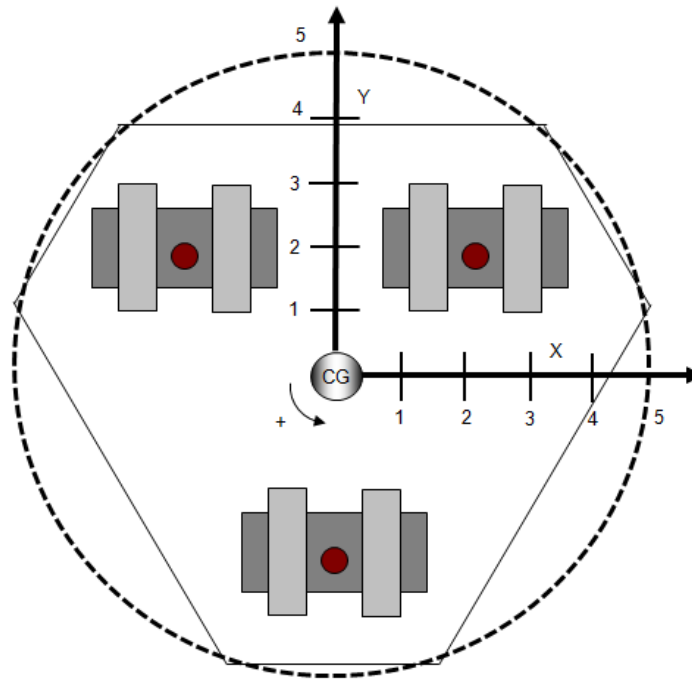


**Figure 3-2 Voltage Circle**

This coordinate system can be seen on the front panel of the vehicle, shown in *Figure 3-1*. In LabVIEW, the imaginary circle is represented by two sliders; one for the y-axis (Vertical,  $V_y$ ) and one for the x-axis (Horizontal,  $V_x$ ). The last slider (Vertical, *Velocity*) represents the velocity control as given from the gamepad and can range between +/- 100% (0-100% forward or 0-100% reverse).

Both the *Velocity* scaling and the x- and y- coordinates of the velocity need to be commanded in order for the vehicle to move. This method for vehicle control was set-up to improve control over the vehicle. It was assumed that the user will automatically move the coordinate control (left analog stick on the gamepad) to its extreme when operating the vehicle. This would represent a full five volts to the motors in any given direction. The right analog stick on the gamepad is used to control a percentage of the voltage. Since the motors are operated in closed-loop speed control mode, the right

analog stick also represents a percentage of the velocity and that is why it is labeled as such. Only a forward and reverse movement is registered on the right analog stick on the gamepad. Again, the analog sticks on the gamepad were set-up in this fashion to increase control over the vehicle. This was thought to be amongst the most intuitive methods for controlling the vehicle with the gamepad.

The dial indicator marked *Rotation* displays the angular speed (rad/s) commanded of the chassis. This is also a command given by the gamepad. The sliders and dial indicator are used as a display only. These are used only to display what the gamepad is sending to the laptop and, therefore, the vehicle.

The two red lights on the right hand side of the front panel indicate the vehicle status. The vehicle can be run with or without the feedforward portion of the control system turned on as indicated by the red light towards the top of the front panel. Running the vehicle without the feedforward control system only allows the alignment of the pods. It does not allow any physical movement of the chassis. The feedforward and feedback portions of the control system were split up again to allow more precise control of the vehicle. In particularly tight situations, it may become advantageous to orient the pods prior to translating or rotating the chassis. This will also aid in ensuring the safety of the vehicle and its surroundings.

The bottom red light on the front panel shows whether or not the emergency stop ( $E\_stop$ ) function is activated. If it is activated, the motor controllers will cease to receive inputs from the gamepad and will coast to a stop due to rolling and air resistance.

The rest of the indicators are output values based upon the physical status of the vehicle. Reverse light indicators, on the left of the front panel, are just a quick way of

telling if the wheels on each pod are running in reverse. Odd numbered wheels are the left wheels on the pods while the even numbered are right wheels. Wheels one and two are on pod one. Pod two houses wheels three and four and wheels five and six are attached to pod three. The *Pod Angle* indicators show the actual pod angle in relation to the chassis in radians. The numbered wheels, pods, and pod angle calculation method is shown in *Figure 3-3*.

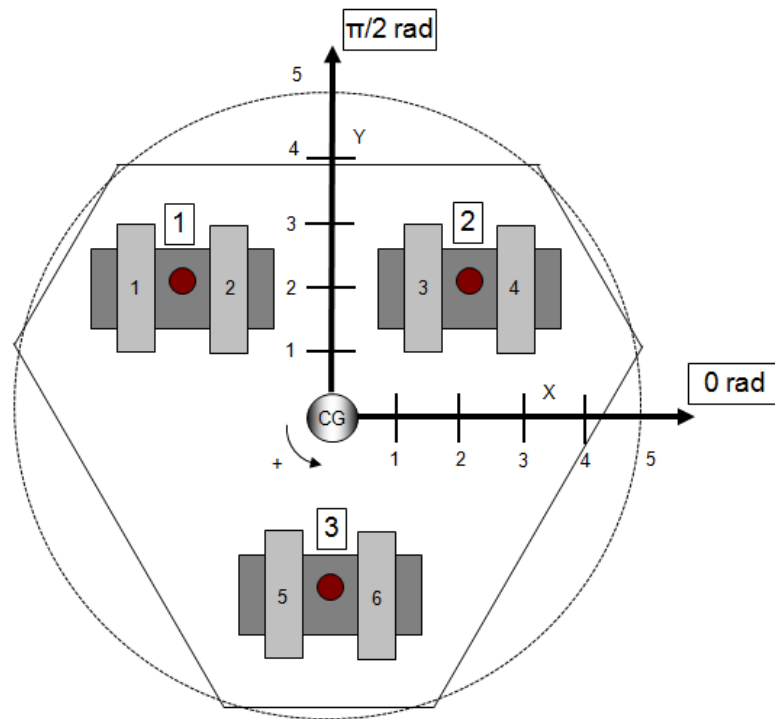


**Figure 3-3 Pod and Wheel Numbering System**

In *Figure 3-3*, the pods are currently aligned at  $\pi/2$  radians in relation to the chassis. This is an example of how the pod angles are calculated both in LabVIEW and in the simulation.

The *delta T* box, shown in *Figure 3-1*, towards the left hand side of the front panel, shows approximately how much time has passed since the last iteration of the algorithm loop implemented in the back panel.

The  $P$ ,  $I$ , and  $D$  gains and the *Max Speed* voltage controls on the upper left hand portion of the front panel allow the operator to quickly change the gains on the control system and the maximum allowable voltage that the motors are allowed to receive. Each voltage control represents one pod and, therefore, two wheels. Although the maximum allowable voltage is separate for each pod, the voltage limit should be set to the same value for all three pods. These controls are only there temporarily for design and debugging purposes. The final layout for the vehicle's front panel will not include these items. The last point to keep in mind is that all of the items displayed on the front panel are there for monitoring purposes or initial set up. They are not essential for the control of the vehicle and most likely will not be used by the driver once he/she starts to drive the vehicle.

On the back panel, the overall vehicle VI starts with receiving inputs from the gamepad. Those inputs are then sent to the feedforward (inverse kinematics) and to a sub-VI that calculates the desired pod angles. Calculated results from the Feedforward Sub-VI and the Desired Pod Angle Sub-VI are sent to the Closed Loop Control Sub-VI. The actual pod angles are also sent to the Closed Loop Control Sub-VI. The Closed Loop Control Sub-VI makes adjustments to the wheel voltage signal and, therefore, corrects for any error that may be present in the system (vehicle). The wheel voltage signals then flow from the Closed Loop Control Sub-VI to the Pod Voltage Control Sub-VI. A screen shot of the entire back panel is too large to be placed within this document and, therefore, is replaced with a block diagram that summarizes the Overall Vehicle VI back panel. This is shown in *Figure 3-4*.

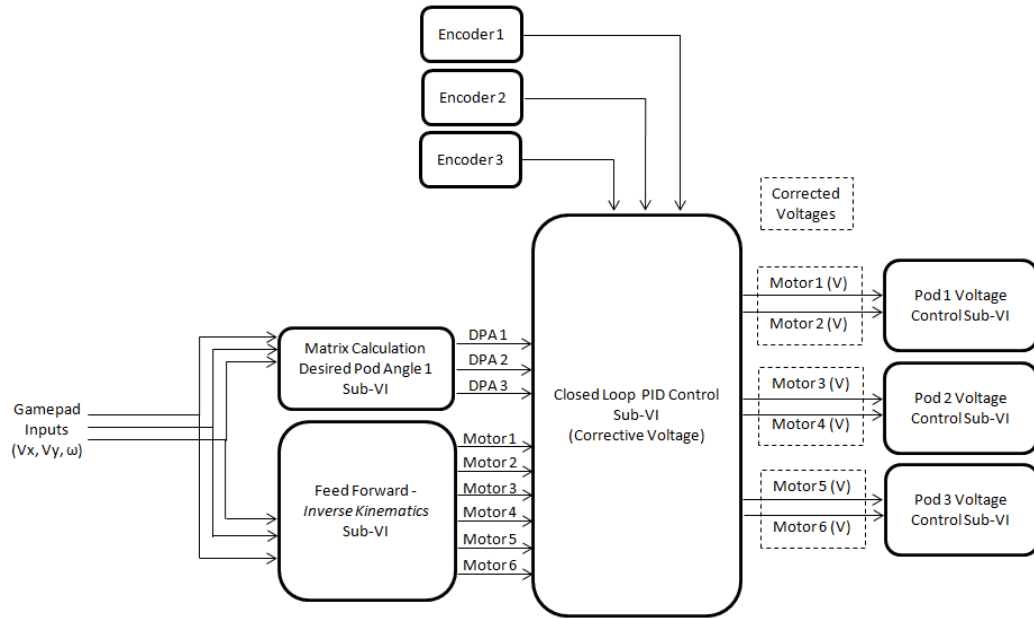


**Figure 3-4 Overall Vehicle VI Back Panel Summary Block Diagram**

The VIs within LabVIEW are an iterative process which means that the program runs one series of calculations (gamepad → inverse kinematics/desired pod angle → closed loop control → motors) and then terminates upon completion. This is considered to be one iteration of the loop. The vehicle, however, is dynamic and thus may require several iterations per driver command. To combat this issue, LabVIEW has built-in loop features.

In order to keep the VI running, a timed loop structure was placed around the sub-VIs and the gamepad controller inputs. The timed loop will continue to run until the user stops the Overall Vehicle VI. The loop used on the vehicle continues to run an iteration once every  $1/5^{\text{th}}$  (0.2) of a second, within precision limits. LabVIEW will continue to do this until the user stops the program from the laptop. It is desired that the time between each iteration of the loop be as low as possible. However, the complex calculations

within the Overall Vehicle VI will not allow the use of cycle times less than approximately 0.2 seconds.

The signals read from the gamepad come in as raw signals and need to be conditioned before they are usable by the vehicle control algorithm. The three most important signals are the x-component and y-component of the vehicle's velocity and desired angular velocity,  $\omega$ . These signals are used to calculate desired pod angles, in relation to the chassis, which in turn are used as inputs to the vehicle control system. All of these calculations aid in better overall control for the driver. More detail on the gamepad controls will be given in Section 3.3.

Signals from the video game controller are fed directly to the feedforward control system (Inverse Kinematic Model Sub-VI) and to the Desired Pod Angle Sub-VI. The feedforward control system helps to send the proper motor voltage to each of the six wheels. The voltage each wheel receives, prior to the correction offered by the PID controller, is dependent on the current angle of the pod, in relation to the chassis, and the control signals given from the gamepad. The Desired Pod Angle Sub-VI calculates what the pod angles should be for a given command from the gamepad. This gives the closed-loop control system its setpoint. More information on the Desired Pod Angle Sub-VI and Inverse Kinematic Model Sub-VI is given in Sections 3.5 and 3.6, respectively.

The Encoder Sub-VI provides the vehicle with actual pod angle measurements. The Encoder Sub-VI will be discussed in detail in Section 3.4. These measurements, one angle from each of the three pods, in conjunction with the desired pod angle measurements help calculate the error for the closed-loop control. Inside the PID Gains Sub-VI, the actual pod angle is subtracted from the desired pod angle or setpoint, for each

particular pod, which becomes the error. The error undergoes additional conditioning before being fed into the PID gains. Details on how the error is conditioned are discussed in Section 3.7. Once the error has been adjusted with the control gains, it is sent to the Control System Sub-VI.

The Control System Sub-VI takes inputs from the PID Gains Sub-VI and the feedforward control signals to generate each individual wheel voltage for that particular loop iteration. The feedforward control should provide wheel voltages that are close to what the vehicle needs. The closed-loop control system in essence corrects the feedforward command to account for errors and disturbances. The control effort calculated by the closed-loop control system is divided by two. One half of the control effort is subtracted from the left wheel and the other half is added to the right wheel on the pod. This will induce a net torque on the pod which helps to change its direction and ultimately reach the setpoint. The Control System Sub-VI and the overall control strategy will be discussed in Section 3.7

Six voltage commands representing desired speed, one for each wheel, are output from the Control System Sub-VI and routed upwards on the back panel. They are received at the Pod Voltage Control Sub-VI. There are three Pod Voltage Control Sub-VIs representing each of the pods. Two voltage signals are fed into each of these VIs. The voltage signals are specific to its intended wheel so it is important that each signal is connected to its correct input. The Pod Voltage Control Sub-VI simply opens up the channels to the DAQ cards so that the voltage signals can be sent to the motor controllers and eventually the motors. Section 3.8 contains detailed information on the Pod Voltage Control Sub-VI.

### 3.3 Gamepad Controls

Figure 3-5 shows the Gamepad Sub-VI. There is no front panel to this VI so only the back panel is shown. The Gamepad Sub-VI could have been embedded as its own Sub-VI, but was left as a part of the Overall Vehicle VI to allow users/drivers to quickly set-up and alter the gamepad controls. Once the controls are finalized, this VI can be embedded as a sub-VI in the Overall Vehicle VI.

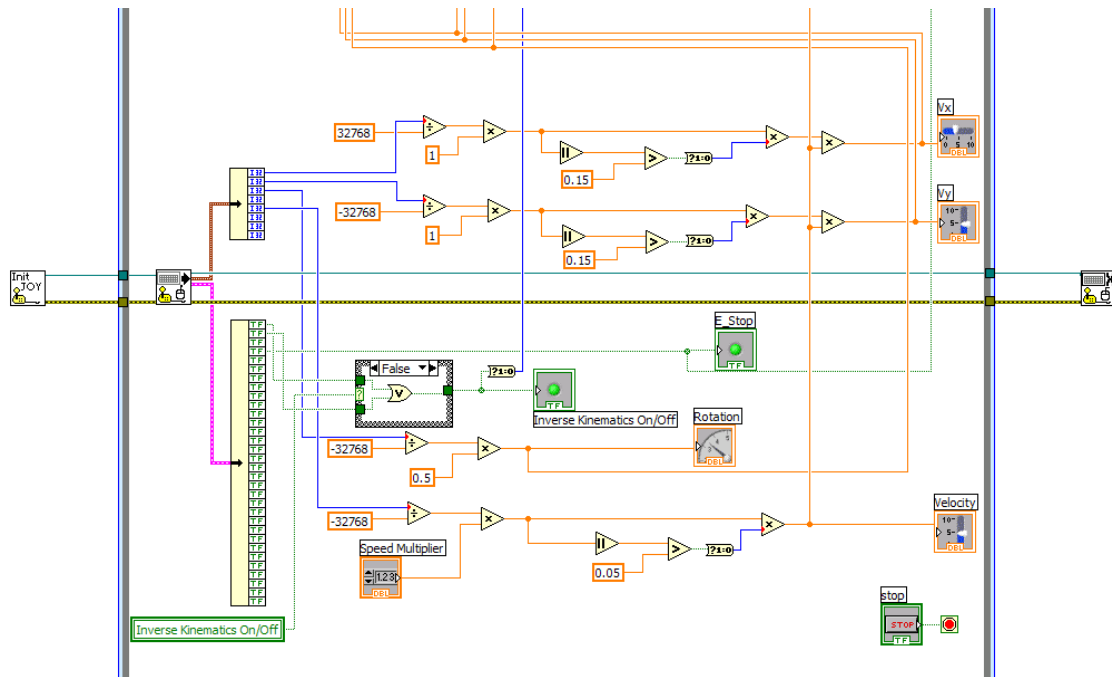
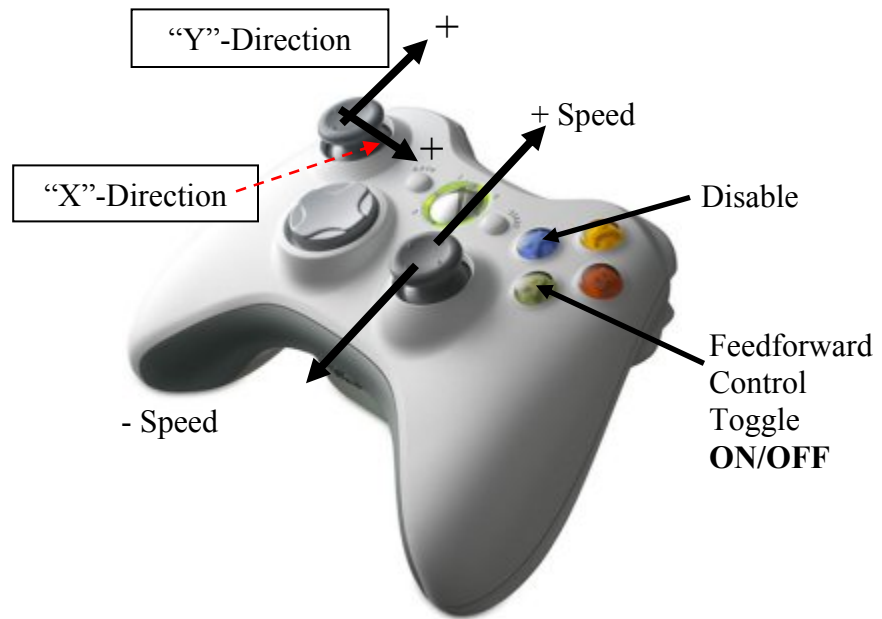


Figure 3-5 Gamepad VI Back Panel

The Init Joy Icon on the left-hand side of Figure 3-5 sets up the lines of communication between the gamepad controller and LabVIEW. This sub-VI resides just outside of the loop since it only needs to be run once per session or once each time the vehicle is used. The sub-VI to its immediate right opens up the channels on the gamepad. Each channel represents a specific button, so care was taken to identify what channel controlled what button. The buttons chosen to control various aspects of the vehicle can

be chosen based upon user preference and can be altered at any time. The current gamepad setup, the actions of each of the buttons, joysticks, and bumpers perform, is shown in *Figures 3-6 and 3-7*.



**Figure 3-6 Gamepad Button Summary (Front) [20]**



**Figure 3-7 Gamepad Button Summary (Back) [21]**

*Table 3-1* describes the function of each button based on *Figures 3-6 and 3-7*.

<b><i>Control Name</i></b>	<b><i>Type</i></b>	<b><i>Range</i></b>	<b><i>Activation</i></b>
<b>y-component Velocity</b>	Analog	+/- 5V	Left Joystick (Up/Down)
<b>x-component Velocity</b>	Analog	+/- 5V	Left Joystick (Right/Left)
<b>Speed Multiplier</b>	Analog	+/- 100 %	Right Joystick (Up/Down)
<b>Chassis Rotation</b>	Analog	+/- 0.5 rad/s	Triggers
<b>Disable</b>	Digital	On / Off	X-button (hold to disable)
<b>Feedforward Control</b>	Digital	On / Off	A-button (Tap, Toggle )

**Table 3-1 Gamepad Button Summary**

As described in Section 3.2 and in *Table 3-1*, the left analog stick on the gamepad has a maximum value of five volts in any direction. This again can be represented by an imaginary circle with a radius of five which is centered at the origin of a coordinate system local to the CG of the chassis. The driver can request a velocity vector which is broken into x- and y-components of velocity depending on the position of the left analog stick.

On the back of the controller, as shown in *Figure 3-7*, there are triggers. Both triggers are part of one axis. The left is for negative values while the right trigger stays positive. Holding down both triggers at the same time cancel one another out and the value goes to zero. This value/axis is reserved for the angular velocity control,  $\omega$ , of the vehicle. A full deflection of one of the triggers will request the vehicle to rotate about its Z-axis with an angular speed of  $\pm 0.5$  rad/s depending on which trigger is pulled.

The signals are read in as integers with a range dependent on the number of bits of the channel being used, in this case 16 bits: one bit for the sign of the raw signal and 15 bits for the controller signal. In order to modify the axis values to something usable for the vehicle, each raw signal was divided by the maximum value given by the possible value ( $2^{15}$ , 32768). This normalizes each signal to a range from -1 to +1. From there, each analog was multiplied by a scale usable for the vehicle. In the case of the x- and y- directions, the signals were multiplied by five to give a range of  $\pm 5$ . The speed control signal was not scaled since a range of  $\pm 1$  was desired. This represents  $\pm 100\%$  of the speed commanded to the vehicle. A negative percentage means the vehicle is instructed to go in reverse. The axis for rotation was multiplied by 0.5. This does not have as wide of a range as the other signals due to vehicle characteristics found during testing. There was no need to require the vehicle to make sharper turns.

These controls are set up based on the preferences of one or two users. Other users may find it necessary to adjust the range of each input to suit their driving style or needs. The most probable adjustment is the rotation command, especially when various terrains place different demands on how the vehicle should turn.

The X-button on the gamepad controls the disable function on the vehicle. By pressing and *HOLDING* this button, the vehicle will become disabled and will coast to a stop regardless of any other commands given by the gamepad. The vehicle will continue to be non-responsive to other gamepad inputs as long as the X-button is HELD.

The A-button controls the feedforward control portion of the control system. This button was setup to act as a toggle. TAPPING the button once will either turn the feedforward control on or off depending on the initial state of the feedforward control. For example, if the feedforward control was on and the A-button was tapped, the feedforward control would then be turned off and vice versa. It is also the case that none of these button or axis configurations are permanent. The controls can be configured to suit the preferences of any user.

### **3.4 Encoder Sub-VI**

The pod encoders are able to track the angle of the pod with the help of a matrix of numbers, combinations of zeros and ones. This matrix is located within the Encoder Sub-VI. *Figure 3-8*, shows this matrix. There are three encoders so there are three sub-VIs. Each sub-VI and its calculations are performed independently for each pod. The encoders used on the vehicle are optical and output a 10-bit binary number which correspond to the angular position of the shaft inside the encoder casing. Since the encoders are 10-bit or has 10 wires that carry a signal, the total number of position combinations is  $2^{10}$ , or 1024 combinations. The number of combinations is the number of sectors the encoder can be divided into. A greater number of sectors reflect a more precise angle measurement. Therefore, the angular position can be tracked to within

360/1024 or 0.352 degrees per sector. In comparison, an encoder that only had three wires would only have  $2^3$  (8) sectors. This brings the angle measurement to within 360/8 or 45 degrees.

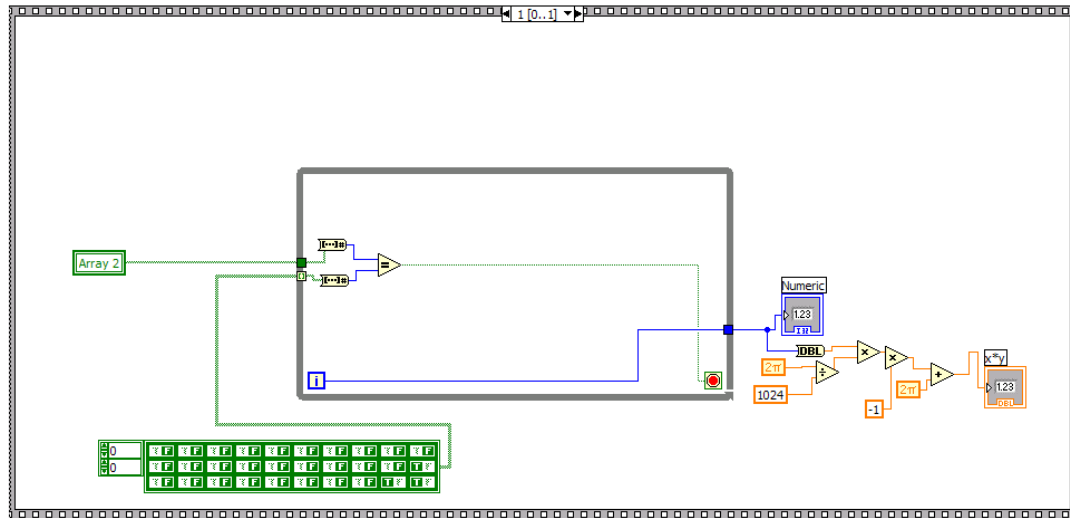


**Figure 3-8 Encoder VI Back Panel (Matrix Comparison)**

*Array 2* is a 1x10 matrix that is made up of ones or zeros, in other words, it is the 10-bit binary number. The ones and zeros correspond to a high voltage (1) or a low voltage (0) signal passed through the connections made between the pod encoder and the data acquisition card. Each different binary number corresponds to a different position of the shaft in the encoder. As the encoder and the shaft to which it is attached changes position, the voltages from each of the channels are passed through the wires connected to the data acquisition card. That data is eventually placed in *Array 2* where it is compared to a hardcoded matrix that maps each binary number to a different angular position.

The hardcoded 1024x10 matrix is included in the back panel of the VI. Only the first three rows are shown in *Figure 3-8*. This matrix includes all possible combinations

where a “1” is represented as true and a “0” is represented as false. By comparing the actual data, *Array 2*, to the hardcoded matrix, the angle can be tracked to within approximately 0.352 degrees. LabVIEW runs a while loop, which compares the array data produced by the encoder to the hardcoded matrix, until there is a match. The number loop iterations it took LabVIEW to find the match corresponds to that particular sector in the encoder. For example, say it took LabVIEW 56 loop iterations to find a match to the data in *Array 2*. That would correspond to the 56<sup>th</sup> sector in the encoder. This places the encoder shaft between 19.688° and 20.039°.

The green LED's on the front panel, shown in *Figure 3-9* are for observational purposes where each LED corresponds to each digit of the binary number read from the encoder and are there mostly to make sure the VI is running correctly.

As each wire receives a voltage input, a high input (1) will cause the LED to light up and a low input (0) will cause the LED to be off. The  $x*y$  value is the encoder angle and the readout labeled *Numeric* is the number of loop iterations or sector the encoder is currently positioned. The encoder angle is eventually routed to the front panel of the Overall Vehicle VI.

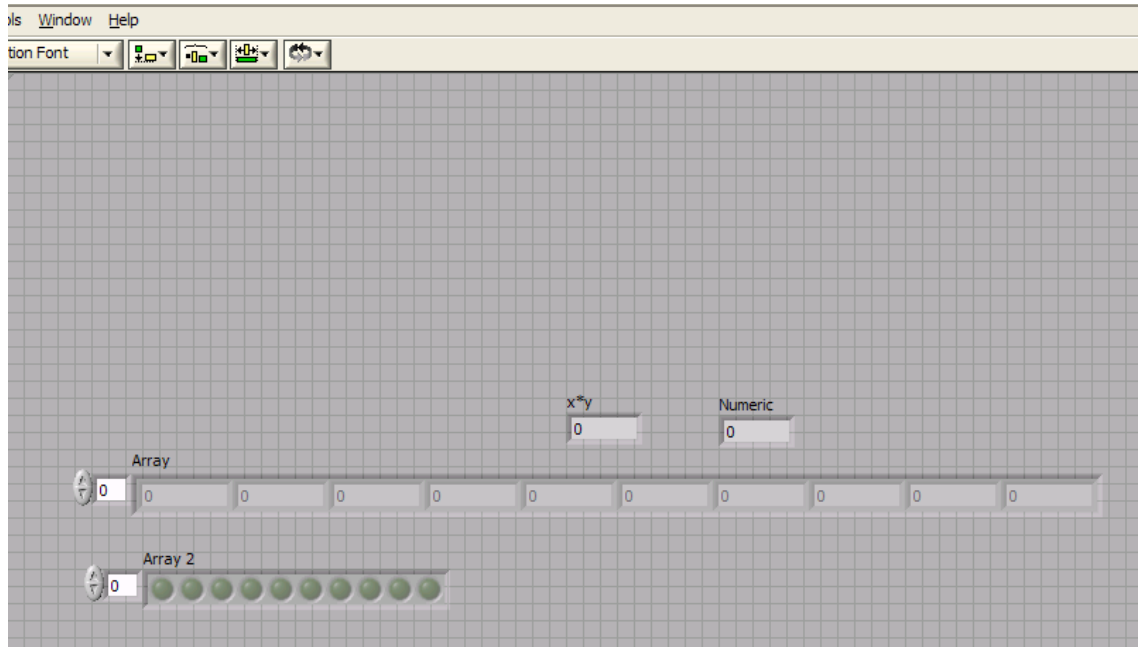


Figure 3-9 Encoder VI (Front Panel)

### 3.5 Desired Pod Angle Sub-VI

The Desired Pod Angle Sub-VI calculates a desired pod angle,  $\theta_i$ , based on the user inputs from the gamepad:  $V_x$ ,  $V_y$ , and  $\omega$ . There are three outputs from the Desired Pod Angle Sub-VI. All three are pod angles which become the setpoint (in relation to the chassis) for each of the pods within the closed loop control system. These angles are compared to their respective pod's actual angle thereby producing an error signal to the closed loop control system. The front panel for this sub-VI does not serve any purpose to the Overall Vehicle VI other than for diagnostic reasons.

Again, the Desired Pod Angle Sub-VI produces a requested angle or desired angle relative to the chassis. This angle is also based on the chassis's local coordinate system shown in *Figure 3-2*. The basis for the desired pod angles calculation is a kinematic analysis which is summarized in Equation 3-1 [1].

The velocities of the pods can be broken down into their x- and y-components through matrix operations using the vehicle's physical parameters and three inputs from the driver. In Equation 3-1, the driver inputs a desired velocity in terms of the chassis's components including translational velocity in either the x- or y-direction and in the rotational direction by specifying a yaw rate,  $\omega$ . The outputs are the velocity of each pod broken down into their x- and y-components. For example,  $V_{1,x}$  is the x-component of the velocity of Pod 1. This is why the output of Equation 3-1 is a 6x1 matrix.

The  $N$ -matrix is a 6x3 matrix which contains a  $B$  term and  $\varphi$  terms. The  $B$  term is the distance, in meters, from the geometrical center of the chassis to the center of a pod (same for all pods). For this vehicle,  $B$  is 0.58928 meters. The  $\varphi_i$  terms represent the angular position from the x-axis (0 radians) of the attachment point of each pod. These angles are again based on the chassis's local coordinate system shown in *Figure 3-2* and are constant since a body-fixed coordinate system is used.

$$\begin{bmatrix} V_{1,x} \\ V_{1,y} \\ V_{2,x} \\ V_{2,y} \\ V_{3,x} \\ V_{3,y} \end{bmatrix} = \begin{bmatrix} 1 & 0 & B \sin \varphi_1 \\ 0 & 1 & -B \cos \varphi_1 \\ 1 & 0 & B \sin \varphi_2 \\ 0 & 1 & -B \cos \varphi_2 \\ 1 & 0 & B \sin \varphi_3 \\ 0 & 1 & -B \cos \varphi_3 \end{bmatrix} \begin{bmatrix} V_x \\ V_y \\ \omega \end{bmatrix} = [N] \begin{bmatrix} V_x \\ V_y \\ \omega \end{bmatrix} \quad (\text{Eq. 3-1})$$

The x-axis is designated as zero (0) or  $2\pi$  radians and the angle increases as a pod or encoder is rotated counter-clockwise. This forces the  $\varphi_i$  value for each pod. As shown in *Figure 3-3*, Pod 1 has an angle of  $5\pi/6$  radians or  $150^\circ$ . Pod 2 is at  $\pi/6$  radians or  $30^\circ$ , and Pod 3 is at  $2\pi/3$  radians or  $270^\circ$ . *Figures 3-10 and 3-11*, help explain the origin of the values in Equation 3-1.



the desired velocity, the desired pod angle  $\theta_i$  is calculated by taking the inverse Tangent of the quotient of the y- and x-component velocities;  $\theta_i = \text{Tan}^{-1}(V_{i,y}/V_{i,x})$  where  $i$  is the index of the particular pod. LabVIEW contains an *atan2* function block that keeps track of the quadrant the angle  $\theta_i$  should be in so as to output the true angle. The *atan2* function block differs from a standard  $\text{Tan}^{-1}$  function because it has a range of  $-\pi$  to  $+\pi$ . The standard  $\text{Tan}^{-1}$  only has a range between  $-\pi/2$  and  $+\pi/2$ . The back panel of the Desired Pod Angle Sub-VI helps to illustrate the construction of the matrices shown in Equation 3-1 as shown in *Figures 3-12 and 3-13*.

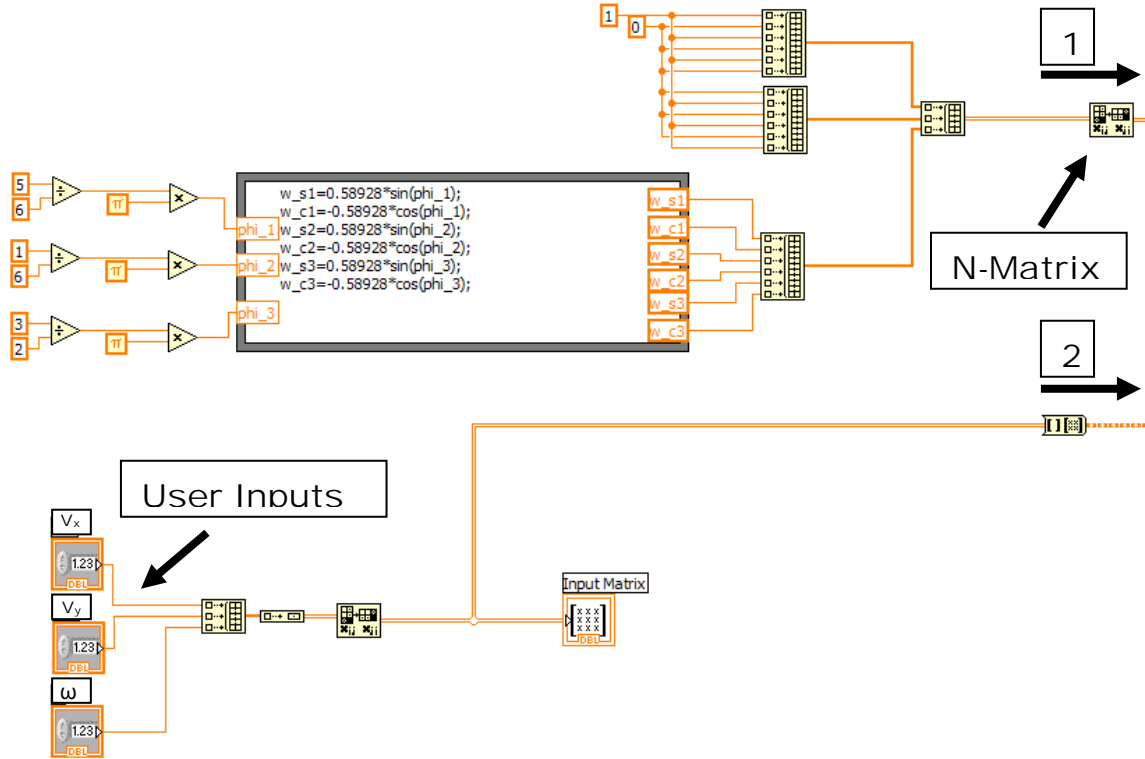


**Figure 3-12 Desired Pod Angle VI Back Panel (Construction of the N-Matrix and User Inputs)**

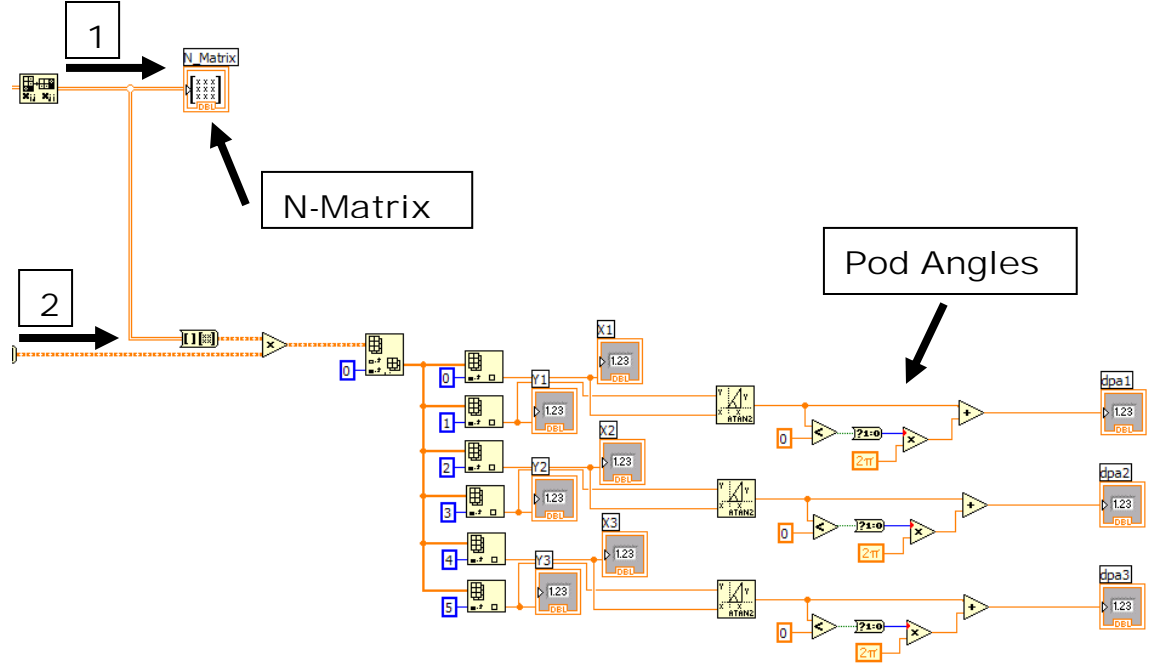


**Figure 3-13 Desired Pod Angle VI Back Panel (N-Matrix and Pod Angle Output)**

After the *atan2* function block, each of the pod angle signals undergo a shift to ensure that the range of the calculated angle is always between 0 and  $2\pi$  radians. Otherwise, the default angle ranges between  $-\pi$  and  $+\pi$ .

### 3.6 Inverse Kinematics Sub-VI

Similar to Equation 3-1 in Section 3.5, a kinematic relationship was derived based on the geometry of the vehicle which relates the velocity of a pod to the velocity of its wheels as described in Equation 3-2. Specifically, Equation 3-2 shows the relationship between the joint velocity  $V_i$  (where the pod connects to the chassis) and the velocities of the left and right wheels on the pod,  $V_{i,l}$  and  $V_{i,r}$ .

$$\begin{bmatrix} V_{i,x} \\ V_{i,y} \end{bmatrix} = \begin{bmatrix} 1/2 \cos(\alpha_i) - S/D \sin(\alpha_i) & 1/2 \cos(\alpha_i) + S/D \sin(\alpha_i) \\ 1/2 \sin(\alpha_i) + S/D \cos(\alpha_i) & 1/2 \sin(\alpha_i) - S/D \cos(\alpha_i) \end{bmatrix} \begin{bmatrix} V_{i,r} \\ V_{i,l} \end{bmatrix} = [J_i] \begin{bmatrix} V_{i,r} \\ V_{i,l} \end{bmatrix} \quad (\text{Eq. 3-2}) [1]$$

In Equation 3-2,  $V_{i,x}$  and  $V_{i,y}$ , are the velocity components of the pod joint where the subscript  $i$  is the  $i^{th}$  pod on the vehicle.  $S$  is the caster distance or the planar distance from the center of the wheel axle to the center of the joint connecting the pod to the chassis.  $D$  is the distance between the centers of the right and left wheel on each pod. The  $S/D$  ratio for this vehicle is 1.2 with  $S$  equal to 0.75 in and  $D$  equal to 6.25 in. Units do not matter in this case since the number is a ratio of two distances. The  $S$  and  $D$  dimension are shown in *Figure 3-14*. The  $\alpha_i$  value is the encoder angle for each pod and would change based upon the current status of the vehicle. Note that the matrix containing the  $S$ ,  $D$  and  $\alpha_i$  values is called the  $J$ -matrix.

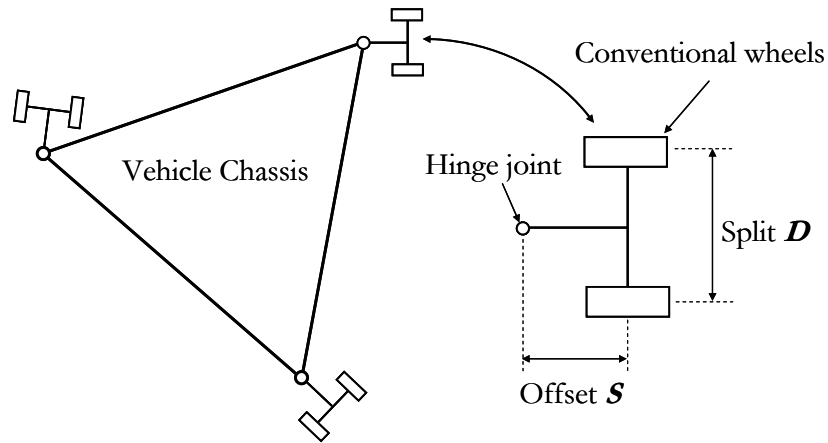


**Figure 3-14 Pod Geometry Description [1]**

The 2x2  $J$ -matrix from each pod can be combined to create a 6x6 matrix which describes the entire vehicle. Using the 6x6  $J$ -matrix from Equation 3-2 can help calculate the left and right wheel velocities for each of the wheels on the vehicle. Equation 3-3 shown below inverts the  $J$ -matrix and multiplies it by the  $N$ -matrix and the control input vector from Equation 3-1. The  $J$  notation is used in Equation 3-3 instead of rewriting all of the terms and to help clarify that there are three pods.

$$\begin{bmatrix} V_{1,r} \\ V_{1,l} \\ V_{2,r} \\ V_{2,l} \\ V_{3,r} \\ V_{3,l} \end{bmatrix} = \begin{bmatrix} [J_1] & 0 & 0 \\ 0 & [J_2] & 0 \\ 0 & 0 & [J_3] \end{bmatrix}^{-1} [N] \begin{bmatrix} V_x \\ V_y \\ \omega \end{bmatrix} \quad (\text{Eq. 3-3})$$

The back panel from the Inverse Kinematic Sub-VI shows the block-by-block construction and multiplication of these matrices. Most of the architecture is shared from the Desired Pod Angle Sub-VI with additional multiplication as shown in Equation 3-3.

Figure 3-15 shows the construction of the  $J$ -matrix,  $N$ -matrix, and the inverted  $J$ -matrix.

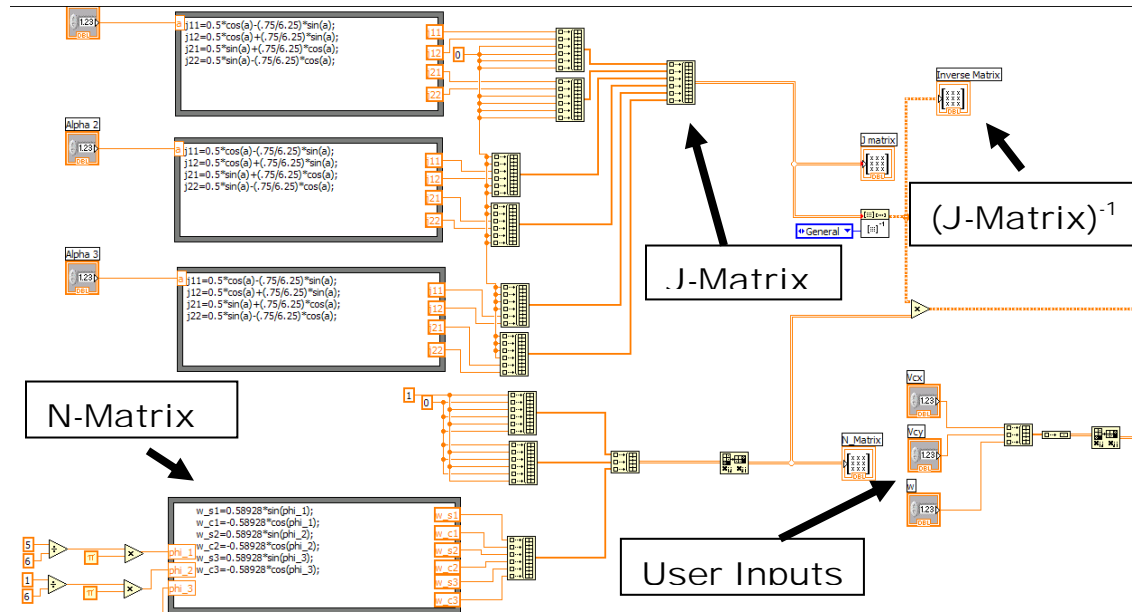


**Figure 3-15 Feedforward Control Back Panel (Construction of Equation 3-1)**

Figure 3-15 also shows the multiplication of the user inputs and the inverted  $J$ -matrix. Figure 3-16 shows the additional steps taken to make sure that the output values for each wheel are normalized to +/- 5 volts thus preventing the saturation of the motors. The output is a 6x1 matrix of normalized wheel voltages. The direction is taken care of

with the sign on the voltage. Negative values signal a wheel running in reverse and vice versa.

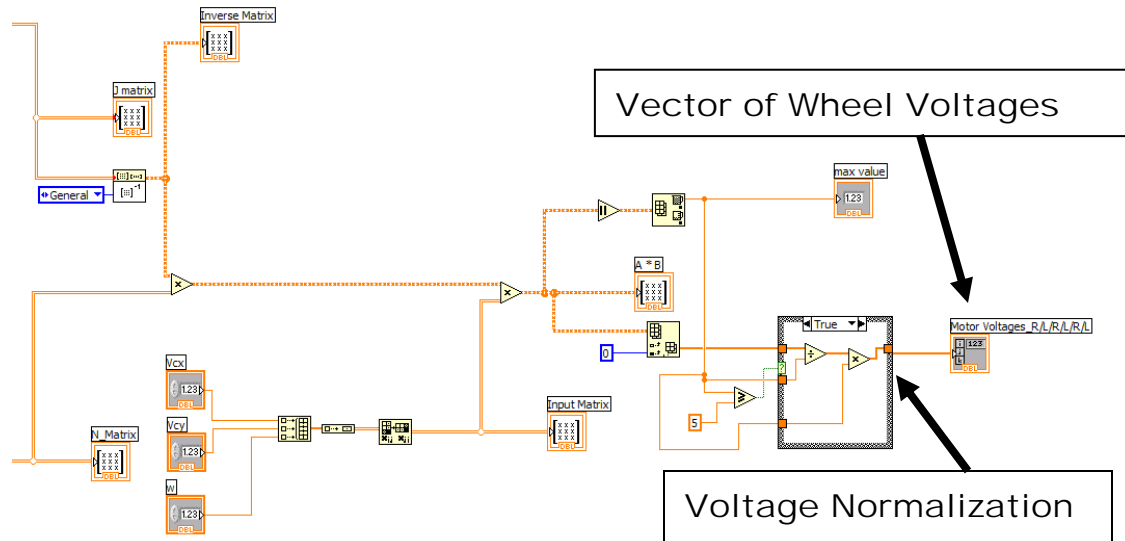


**Figure 3-16 Feedforward Control Back Panel (Wheel Voltage Calculation and Normalization)**

If this vehicle were to run in open-loop control, the pod angles ( $\alpha_i$ ) fed into this VI would be the actual pod angles as read by the encoders. This approach would produce the desired wheel speeds at any given instant if the models were correct and there was no slip at the wheels. Since the vehicle will employ feedback, the angles ( $\alpha_i$ ) employed in this VI to calculate the matrix  $J$  have been changed to the desired pod angles ( $\theta_i$ ). This is to trick the inverse kinematics into thinking that the pods are already aligned where they should be. This will make the feedforward controller output the same voltage between the left and right wheels when it is desired to travel in a straight line. It will also output the appropriate voltage in steady-state between the right and left wheel when turning if there is no error in the system. All of this is done to help the performance of the closed-loop control system. The concern is that the feedback portion of the controller will fight against the feedforward portion of the controller if both controllers are sent the actual pod

angles ( $\alpha_i$ ). By employing only the desired pod angles in the feedforward controller, only the closed-loop controller eliminates the error in the system. This approach helps to decouple the two controllers and was found to make the vehicle easier to tune and more predictable while being driven.

### **3.7 Closed-loop Control System Sub-VI**

The purpose of the control system is to close the loop and provide feedback at the pod level in order to assist the driver with achieving a desired heading for the vehicle. This was found to be necessary due to the significant wheel scrubbing and slip that made open-loop control unusable at all but the slowest speeds. A pod-level approach to control was decided on due to the speed advantage the pod control had over chassis control. This was also decided since the driver could theoretically correct for disturbances at the chassis level, but not at the pod level. The control strategy and reasons why the particular controller type was chosen will be discussed in detail in Chapter 5.

A simple proportional-integral-derivative (PID) controller was used on this vehicle and is shown in the PID Gain Sub-VI. An Integral and derivative function were both available in LabVIEW, but the integral function did not have an option for anti-windup or error reset. For this project, emphasis is placed on speed. Having an integrator with no error reset might lead to excessive overshoot and, therefore, take more time for the pod to reach steady state. Scrubbing and slip in the wheels as well as stiction in the slip-rings all cause the pods to take longer to reach a commanded, steady-state angle in relation to the chassis. Therefore, a new integral function was required for the vehicle.

The derivative function within LabVIEW worked well, so it was utilized in the PID Gain Sub-VI. *Figure 3-17*, shows a portion of the back panel for the PID Gain Sub-VI which highlights the integral and derivative functions.

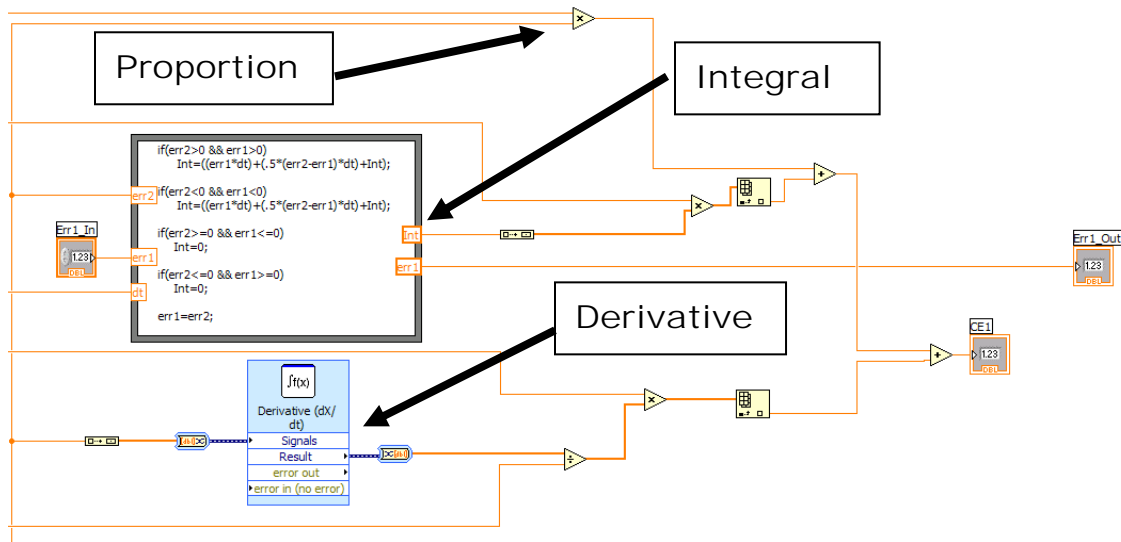


**Figure 3-17 PID Gain VI Back Panel**

As shown in *Figure 3-17*, the integral function is a simple four line conditional statement that checks for the current state of the error and then proceeds in adding the new error. If the error changes sign (negative to positive or positive to negative) then the error is set to zero (0). The integration of the error is approximated using the trapezoidal rule and so the  $\Delta t$ , or time between each loop iteration within LabVIEW, is used as the  $dt$  value within the summation. In *Figure 3-17*, the *err1* represents old error or the initial error, while *err2* is the new error or the summation of the error. Depending on the condition of *err1*, the integral function will either continue to add the error or set it to zero (0) for the next loop iteration.

The error is calculated by subtracting the actual pod angle of each pod from the desired pod angle setpoint. This subtraction is shown in PID Gain Sub-VI Back Panel in *Figure 3-18*.

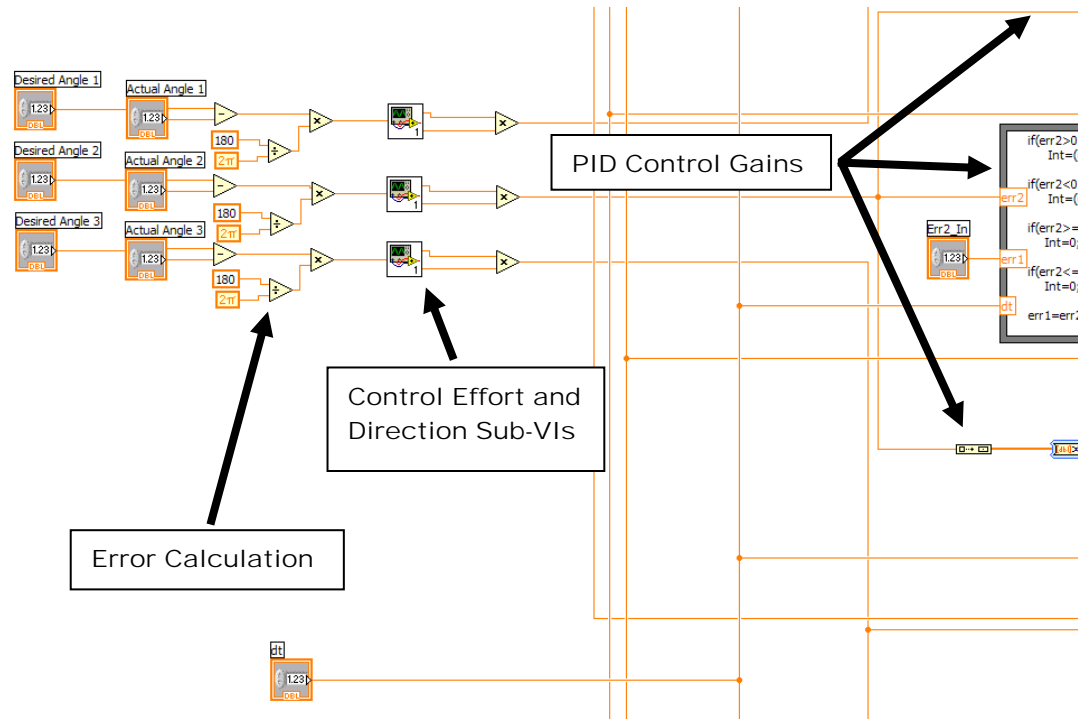


**Figure 3-18 PID Gain VI Back Panel (Error Calculation)**

The error is in units of degrees and would normally be available for direct use in the control system. However, each pod can revolve 360 degrees and end up back in the same location as it started. This creates a problem when the pods read 360 degrees since this could also read 0 degrees. This is especially of concern when the setpoint is near 0 degrees.

There is also a problem with symmetry when using the direct subtraction. Once the error reaches  $\pm 180$  degrees away from the setpoint, the vehicle would have trouble knowing whether to go clockwise or counter-clockwise to correct the error. Preliminary testing showed that the vehicle often would take the longest path back to the setpoint.

The Control Effort and Direction Sub-VI within the PID Gain Sub-VI takes care of these problems and still keeps the error linear with a few piecewise functions. One piecewise function controls the magnitude with a maximum control effort requested at +/- 180 degrees of error and no control effort requested at 0 or 360 degrees. A second piecewise function accounts for the direction such that the pods take the shortest path back to the setpoint. At 180 degrees of error, where the pod could go either direction, the piecewise function dictates that the pods turn clockwise by default. This could have easily been set to rotate counter-clockwise. In this scenario, directional values that are positive make the pods go clockwise. Values that are negative make the pods rotate counter-clockwise. *Figure 3-19* shows the Control Effort and Direction Sub-VI within the PID Gain Sub-VI.

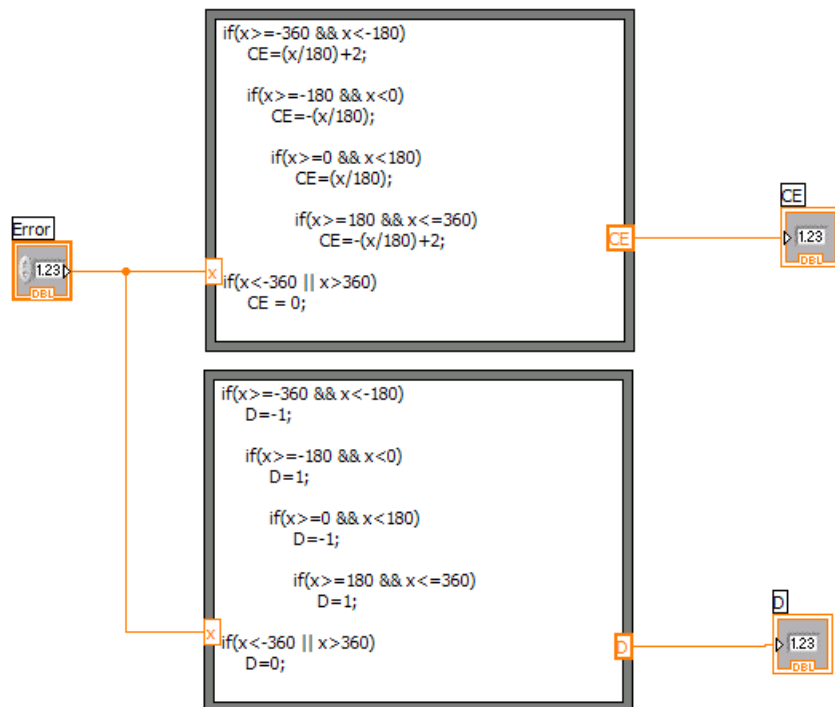


**Figure 3-19 Control Effort and Direction Sub-VI within the PID Gain Sub-VI**

In *Figure 3-19*, the error comes is the input to the Control Effort and Direction Sub-VI which gets processed through both of the piecewise functions and then is output on the right side of the VI. The *CE* value represents the modified error or corrected error and ranges between zero (0) and one (1). The *D* value represents the direction and is either equal to zero (0), negative one (-1), or positive one (+1). These two values are then multiplied in the PID Gains Sub-VI where the result represents both a direction and magnitude of error. This is the error that is then fed into the proportional, integral, and derivative terms. *Figures 3-20 and 3-21* show the piecewise functions graphically.

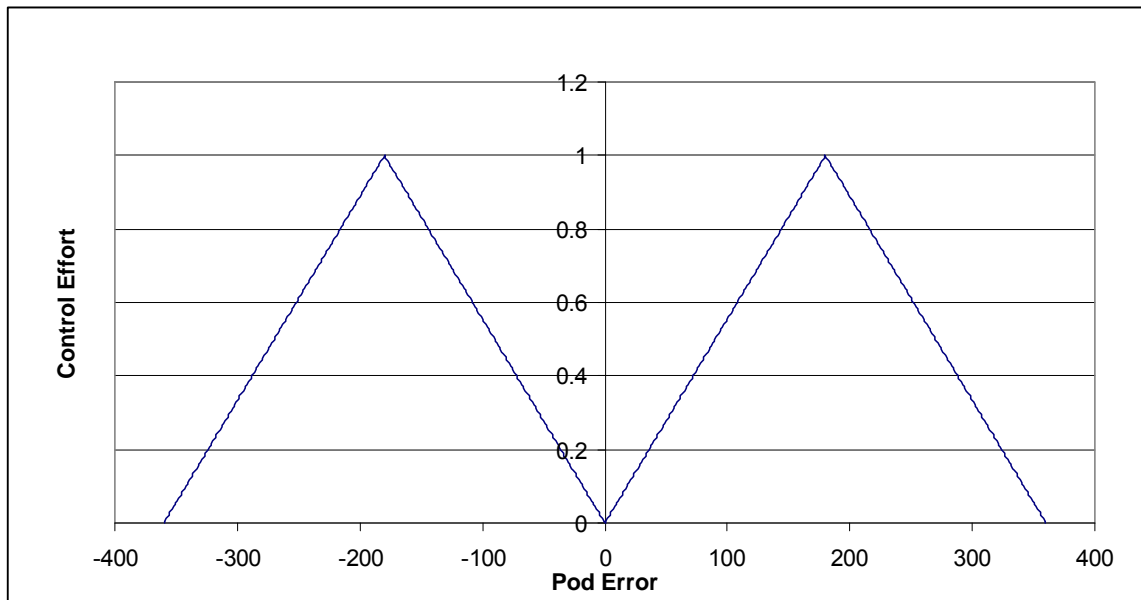


**Figure 3-20 Control Effort Calculation as a Function of Calculated Pod Error**

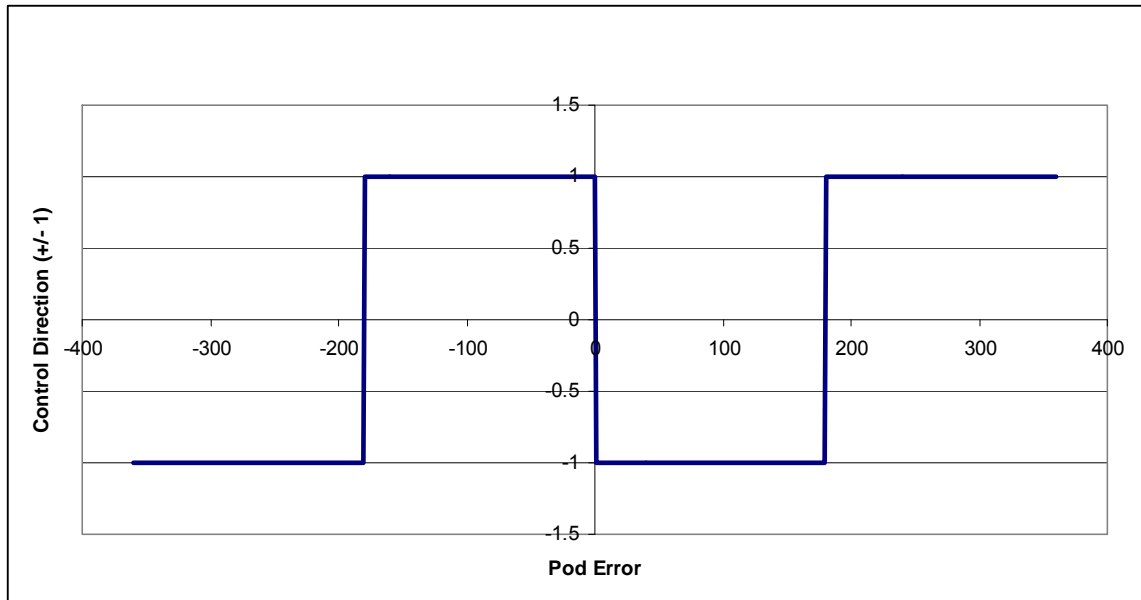


**Figure 3-21 Direction Calculation as a Function of Calculated Pod Error**

For each pod, the corrected error is multiplied by each of the gains. The three terms are added to make an overall control effort for each pod. This overall control effort is then sent through the PID Gain Sub-VI and out into the Overall Vehicle VI. The three control effort signals, one for each pod, are then routed to the Control System Sub-VI. In this VI, the control effort signals for each of the pods and the voltage signals from the feedforward controller are added together to create a final set of voltages for each of the six wheels. *Figure 3-22* shows the back panel for the Control System Sub-VI.

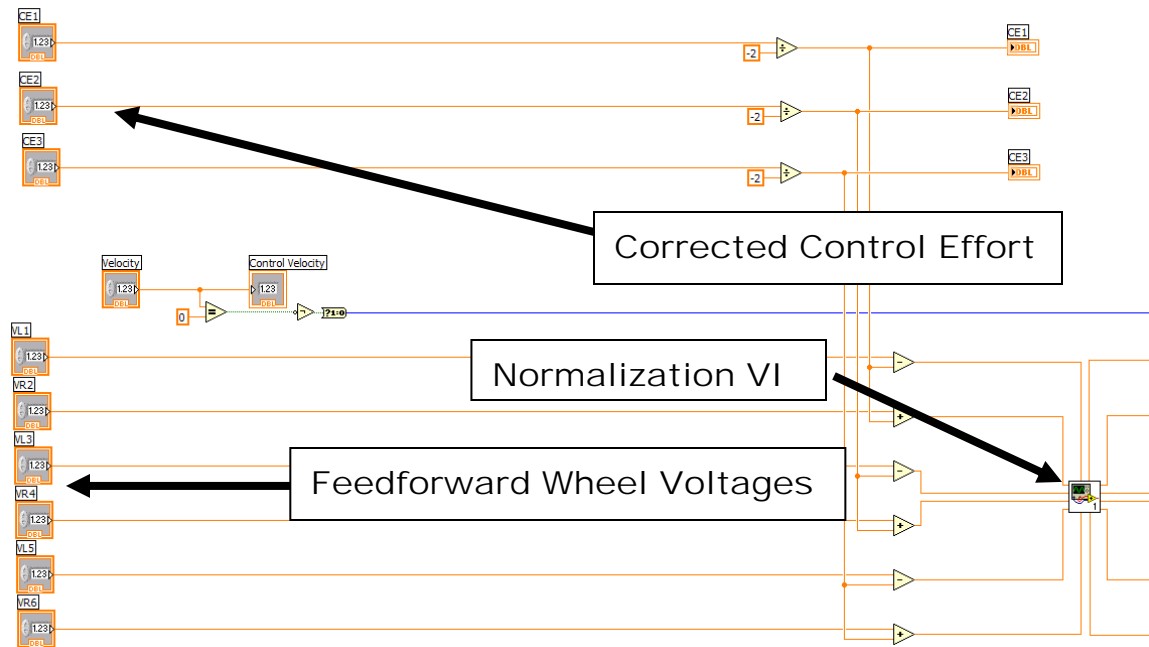


**Figure 3-22 Control System VI Back Panel**

In the Control System VI, the corrected control effort for each pod is divided by two. One half of the control effort is subtracted from the left wheel and the other half is added to the right wheel. This induces a net torque on the pod as long as there is a correcting signal coming from the PID Gains Sub-VI. Subtracting the effort from the left and adding to the right wheels ensure that the pods rotate in the correct direction as instructed from the PID Gains Sub-VI.

Simply adding the control effort to the feedforward voltages creates a potential for a total wheel voltage to be greater than 5 volts. To combat this, another sub-VI called the 5 Volt Normalization Sub-VI was added to bring the range to within +/- 5 Volts. Most of the coding within this VI was borrowed from the Inverse Kinematics Sub-VI since it included a 5 Volt normalization procedure. The back panel for the 5 Volt Normalization Sub-VI is shown in *Figure 3-23*.

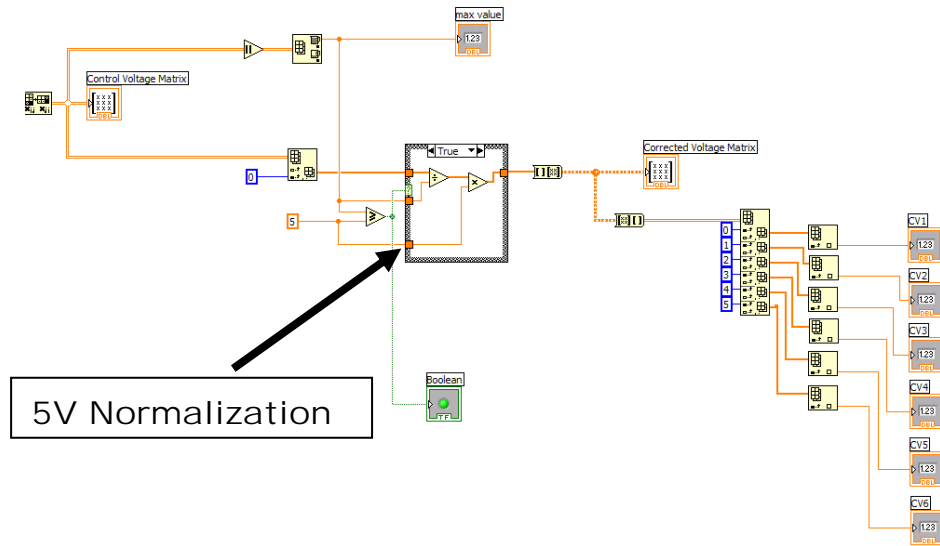


**Figure 3-23 5-Volt Normalization VI Back Panel**

The left side of the VI is the addition of the feedforward control voltages with the corrected control effort values. The VI then checks the 6x1 matrix of values to see if the absolute value of any of the voltages is greater than five. If one of the voltages exceeds  $\pm 5$ , the matrix is divided by the absolute value of the maximum value and then multiplied by five. Performing the normalization in this manner keeps the size of the commands to the individual wheels the same relative to one another. This has the effect of maintaining the overall desired heading of the vehicle. If none of the voltages exceed  $\pm 5$ , the matrix is passed through without scaling. The output, right side of the VI, is a 6x1 matrix of usable voltages. Directly to the right of the 6x1 matrix are LabVIEW blocks that extract individual values from the matrix depending on the index number given to the block. Eventually all six wheel voltages are extracted from the matrix so that the individual wheel voltages can be routed to the rest of the Overall Vehicle VI as needed.

### 3.8 Pod Voltage Control Sub-VI

The final wheel voltages calculated in Section 3.7 are routed from the Control System Sub-VI within the Overall Vehicle VI to the three Pod Voltage Control Sub-VIs. There is one Pod Voltage Control Sub-VI for each of the pods. Of the six wheel voltages found in the Control System Sub-VI, there are three left and three right wheel voltages. One left and one right wheel voltage, corresponding to their respective pod number, is routed to each Pod Voltage Control Sub-VI. The result is that “Pod 1 Voltage Control Sub-VI” represents pod one. The final left wheel voltage one and the final right wheel voltage one, *CVLI* and *CVRI*, are both routed to Pod 1 Voltage Control Sub-VI.

The Pod Voltage Control Sub-VI is very simple. In this VI, there are five channels opened up on the DAQ card. Three are digital signals and the last two are analog. The analog signals are the voltage signals that command the individual wheel speeds. There is one analog signal for the left wheel and one for the right wheel. In this VI, the sign (+ or -) is extracted from the analog signal, converted to a digital signal, and used to maintain the wheel’s direction. Positive values mean that it is desired that the wheel roll forward and negative values mean that the wheel is to roll backward. The left side of *Figure 3-24* shows where the wheel voltages come in and where the DAQ assistant block opens up the analog channels on the DAQ card.

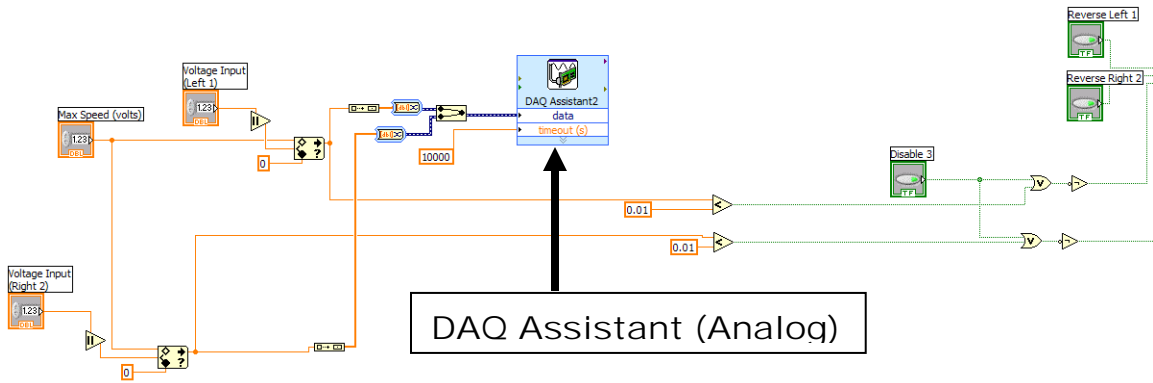


**Figure 3-24 Pod Voltage Control Sub-VI Back Panel (Analog Signals)**

The extracted sign from the wheel voltage represents a digital signal, so there is one signal for each of the two motors. The sign from the wheel voltages are converted into a Boolean operator where a negative value will cause the operator to be true and will, therefore, reverse the motor. A true value coming from the VI produces a physical command of 5 Volts to the direction channel of the motor controller while a false value produces a command of 0 Volts.

The last digital signal is for the wheel disable. Only one signal is needed for this since we will always disable both wheels on a given pod together. Similar to the wheel direction signals, the disable is a Boolean operator. When the disable button on the gamepad is depressed, a high value (1) will be sent to the Boolean operator and converted to true or false. A value of (1) represents a true value and so the DAQ card sends a 5 volt signal to the motor controllers to disable the brushless DC motors.

Similar to the analog DAQ assistant, the digital DAQ assistant opens up three digital output channels, instead of analog outputs, on the DAQ card. This will allow the high and low signals to be sent to the motor controllers. As shown in *Figure 3-24*, all three of the digital signals are routed through this DAQ assistant. The Pod Voltage

Control Sub-VI corresponding to the other two pods are analogous to the one shown in *Figure 3-24*.

## ***4. Vehicle Parameterization***

### **4.1 Modeling Preparation**

In preparation for modeling the vehicle in simulation in Chapter 5, it is necessary to characterize the vehicle using measured data. The development of a tire model is the most important application of this data, but other parameters such as air resistance, slipping friction, and motor characteristics are also important aspects of the vehicle model that must be identified. The remainder of Chapter 4 will break down these parameterizations. Furthermore, the test procedures used to gather this data will be explained in detail as Chapter 4 progresses.

### **4.2 Tire Model**

A great deal of time could have been spent on the tire model alone. More time spent characterizing the model yields improved accuracy of the simulation in terms of the predicted longitudinal and lateral acceleration of the vehicle during different types of maneuvers. There are many things that could be taken into consideration when characterizing the tire equipped on the vehicle. Normal load, temperature, air pressure, surface roughness, surface material, and suspension set-up all play a role in how the tire performs on the vehicle.

In the interest of time, just three parameters describing the tires equipped on the vehicle were studied. Furthermore, these parameters were studied using a relatively tight range of conditions. Currently, the vehicle is run indoors on one surface. So for modeling purposes, the tire was characterized using only one friction surface; the shop

floor in the engineering building highbay. Since the vehicle was always run indoors, the temperature remained fairly consistent from test to test. The vehicle was not driven to the limits of traction enough to force heat or air pressure build-up in the tire. Tire pressure was kept at 20psi on all six wheels and consistent suspension geometry was maintained on the vehicle. Given these initial conditions and assumptions, the vehicle was tested for longitudinal tractive force, lateral force, and rolling resistance [22].

#### **4.2.1 Rolling Resistance**

The first piece of tire information needed to describe the tire is the rolling resistance. To acquire this information the vehicle was accelerated and then allowed to coast to a stop. For this test, only the deceleration portion of the data was considered. Once again, vehicle velocity was estimated from the DC motor's Hall-effect sensors assuming no-slip since the wheels were not being driven during the coast-down.

The derivative of the velocity curve gave the deceleration profile. This profile was multiplied by the mass of the vehicle to give the total resistance force during the deceleration period, including air resistance. As the velocity approaches 0 m/s, however, the force drastically falls to zero. The force value recorded just prior to the force falling to zero is representative of the rolling resistance. There is a great deal of noise generated by the Hall-effects sensors which is shown in *Figure 4-1*. Nonetheless, straight lines were fit to the data. *Figure 4-1* is just one of the data sets acquired from the vehicle.

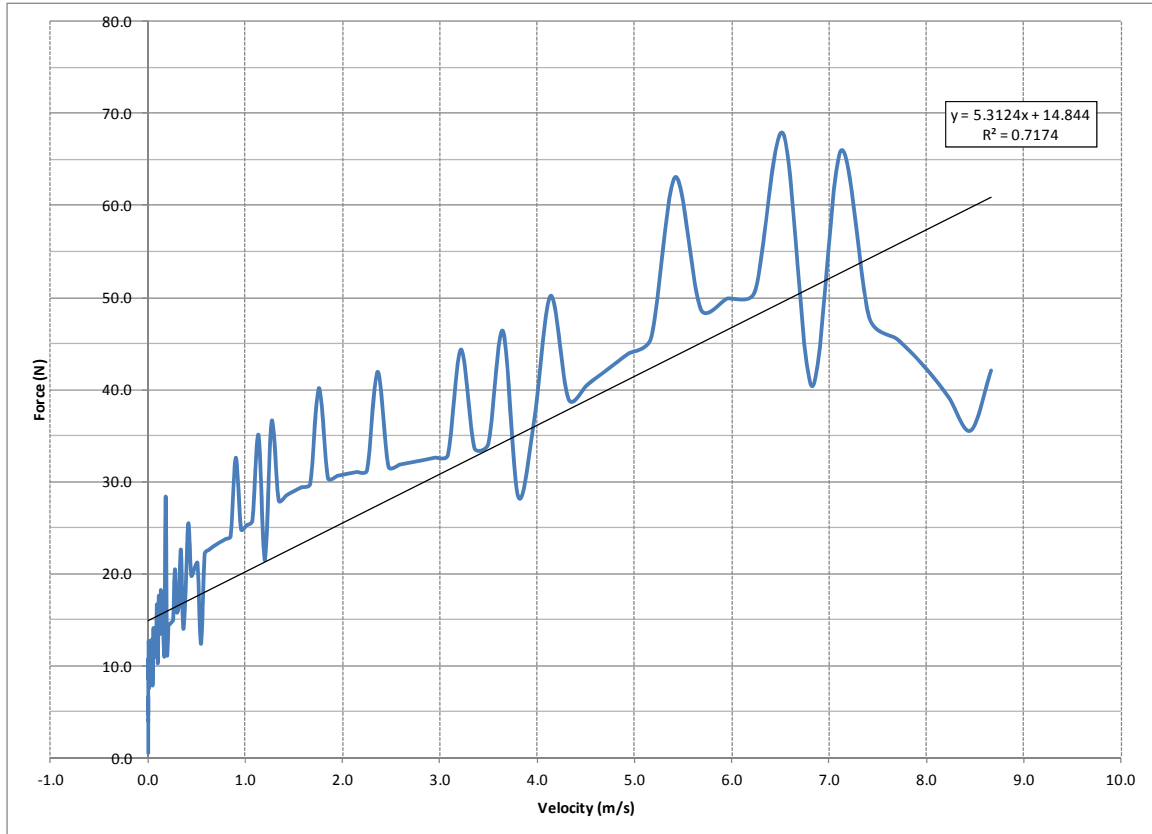


**Figure 4-1 Coast-down Test Results for Determining Rolling Resistance**

The *y-intercept* of the data set, shown in *Figure 4-1*, is the rolling resistance for all six wheels. For this vehicle, the rolling resistance was approximated as 15.385N or about 2.564N for each wheel; the average of several data sets. For simulation purposes, the rolling resistance force of each tire can be approximated by using a signum function where rolling resistance ( $RR$ ) =  $-2.564 \cdot \text{sgn}(\text{wheel velocity})$ . The calculated rolling resistance will eventually be added to the longitudinal tire forces. Using a signum function ensures that the rolling resistance will always oppose the motion of the tires.

#### **4.2.2 Longitudinal Tire Forces**

The force a tire exerts longitudinally is commonly understood to be a function of the slip ratio which is described by Equation 4-1. Slip ratio is the normalized difference

between the velocity of the vehicle's chassis and the velocity of the tire. Refer to *Figure 4-2* to further understand each variable in Equation 4-1.

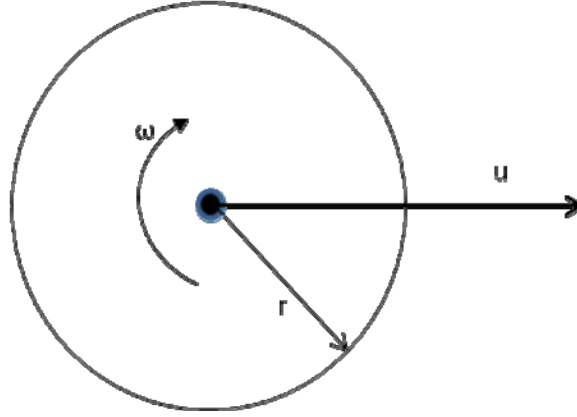


**Figure 4-2 Explanation of Variables in Slip Ratio Formula**

$$SR = \frac{u - rw}{u} \quad \text{if } u \geq rw \text{ (Braking)} \quad (\text{Eq. 4-1})$$

$$SR = \frac{rw - u}{rw} \quad \text{if } rw \geq u \text{ (Acceleration)}$$

In Equation 4-1,  $SR$  is the slip ratio as a fraction of the total slip.  $u$  is the translational speed of the axle (m/s),  $r$  is the wheel radius (m), and  $\omega$  is the angular speed (rad/s). Only the acceleration portion of the slip ratio formula was used since vehicle does not have brakes [23] [24] [25].

To find the relationship between longitudinal tire force and slip ratio, the vehicle was run under different levels of constant acceleration. During these vehicle tests the motor controllers were set to torque-control mode. This maintains the output torque at a level that is proportional to the commanded voltage. This was done to maintain consistency in the torque output throughout the acceleration phase of the test. Two of the six wheels, one pod, were not driven during vehicle acceleration tests. This was done

since non-driven wheels do not experience significant slip and hence the rotational velocity of the wheels (which is measured) serves as a reasonable indication of the vehicle's translational velocity. In other words, the translational velocity  $u$  is approximated using the following relationship for rolling without slip,  $r\omega_{\text{non-driven}}$ . The rotational velocity of the driven wheels is measured to allow calculation of the slip ratio of each driven wheel as shown in Equation 4-1. The difference between the velocities of the driven and non-driven wheels can be seen in *Figure 4-3*.

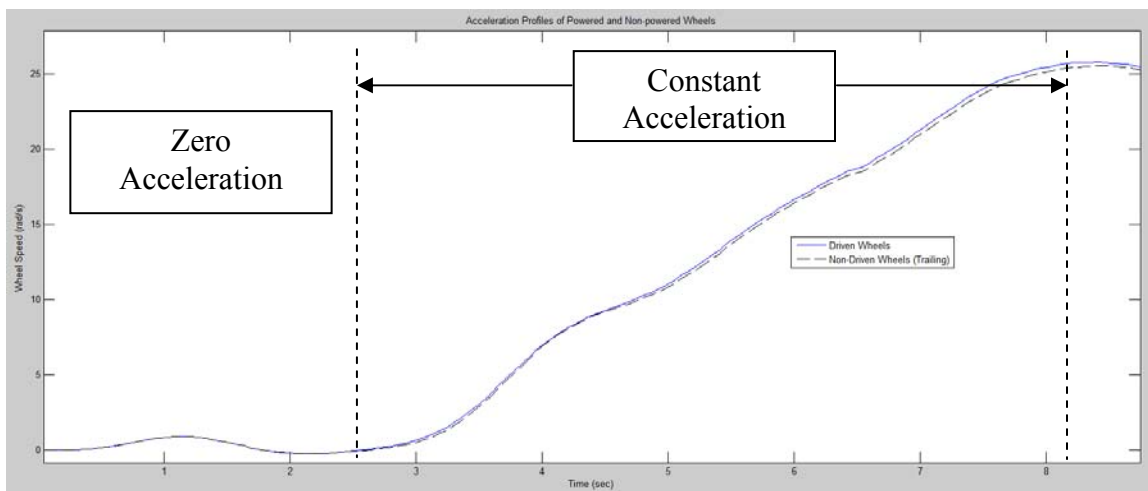


**Figure 4-3 Example Velocity Profile Used to Calculate Slip Ratio**

The forces estimated from the acceleration tests were a summation of forces. The air and rolling resistance had to be added to the net acceleration force. (Actually a subtraction of a resistive force) This solves for the forces exerted by the tires while accelerating.

The acceleration of the chassis was estimated from the derivative (slope) of the wheel-speed graph. The acceleration multiplied by the vehicle mass yields the approximate tractive force being generated that is accelerating the vehicle. The Slip is calculated using the difference between the powered and non-powered wheels as

explained above. By fitting a curve to the data in *Figure 4-4*, the tire characteristic during longitudinal acceleration was approximated.

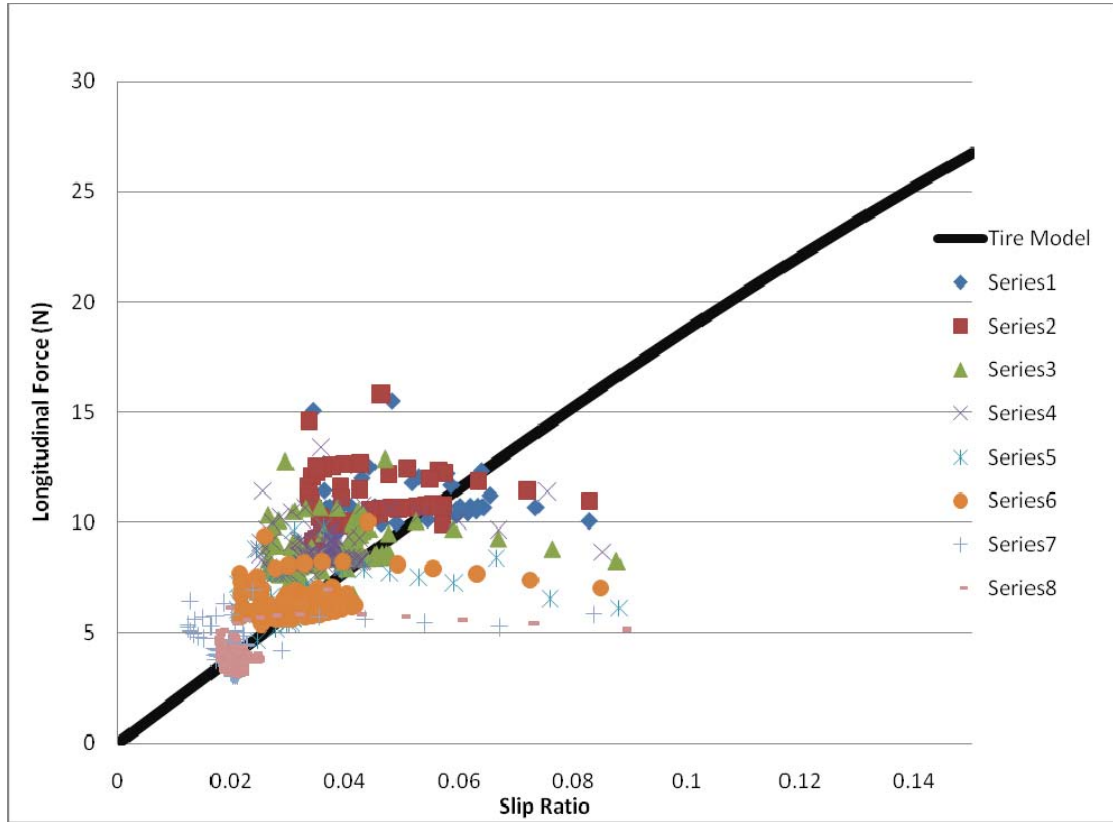


**Figure 4-4 Slip Ratio versus Accelerating Force**

The tire model was designed to fit the available data under the limitation of a maximum five volt command to the motors in torque-control mode. The closed-loop function has adjustable potentiometers which can control the acceleration rate of the vehicle. The current potentiometer is set to the highest setting allowing the vehicle to reach top speed in minimum time. This acceleration level is consistent with the maximum rate experienced when operating in speed-control mode.

The curve fitted to acceleration data employed Pacejka's Magic Formula Tire Model which can be seen in Equation 4-2 [14] [24] [26] [27].

$$F(x) = D \sin(C \arctan(Bx - E(Bx - \arctan(Bx)))) \quad (\text{Eq. 4-2})$$

Parameters  $D$ ,  $C$ ,  $B$ , and  $E$  are all constants that help describe the tire's shape, profile, and static characteristics. By altering the parameters in Equation 4-2, the shape/profile of the tire model can be adjusted to closely fit experimental tire data.

In Equation 4-2,  $x$  is the independent variable and represents longitudinal slip. However,  $x$  can be various independent variables depending on the parameter of the tire in which the modeler is interested. These parameters can include but are not limited to slip angle or steering angle.  $F(x)$  represents the output which is longitudinal force in the case of Equation 4-2. This could also represent lateral force or self aligning torque based on if  $x$  was slip angle or steering angle, respectively.

The longitudinal tire model is bound between a slip ratio of 0 and 1. Although, slip ratios of one never occurred during dynamic testing, the tractive force experienced at high-levels of slip was estimated by performing a test on the stationary vehicle. Specifically, a wheel was twisted by introducing a torque, manually, until the tire broke traction. Just as the tire lost adhesion to the floor, a force transducer recorded maximum force. This force was multiplied by the length of the moment arm on which the force was applied. The result is the torque required to break traction between the tire and the floor. The force at the point of contact between the tire and the floor can be found by dividing the torque required to brake traction by the radius of the tire. This is the force generated at a slip ratio of one. *Figure 4-5* shows the fitment of Equation 4-2 to data taken from the vehicle between slip ratios of 0 and +1. Forces generated between slip ratios of -1 and 0 are the negative of the forces generated between slip ratios of 0 and +1. This is shown in *Figure 4-5*.

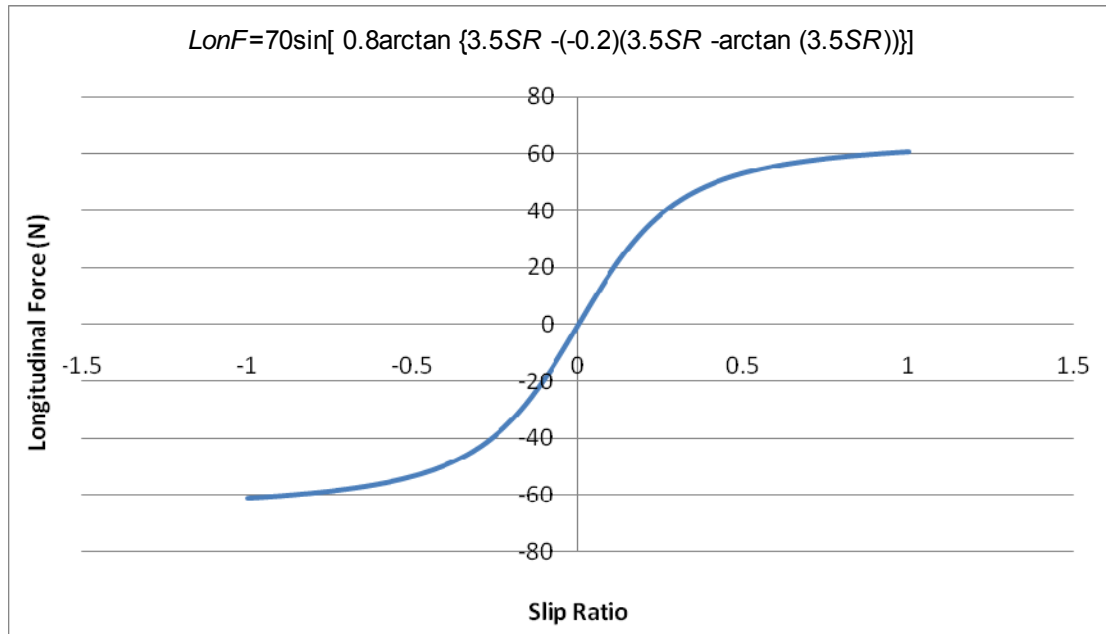


**Figure 4-5 Complete Longitudinal Tire Model**

#### **4.2.3 Lateral Tire Forces**

Lateral tire forces are generated in the process of turning. Therefore, a simulation model that closely predicts the vehicle's behavior in turning must model lateral tire forces. Experience with the vehicle has demonstrated that control is particularly necessary during turning maneuvers of the vehicle. Therefore, a simulation environment that can assist with controller development must be able to simulate turning maneuvers.

Modeling the lateral forces of the tire is done in a similar manner to how the tire was modeled for longitudinal forces. Whereas tractive force was modeled as a function of slip ratio, lateral forces are modeled as function of slip angle. *Figure 4-6* shows the way the lateral tire force is generated and how slip angle  $\lambda$  is defined [23] [26].

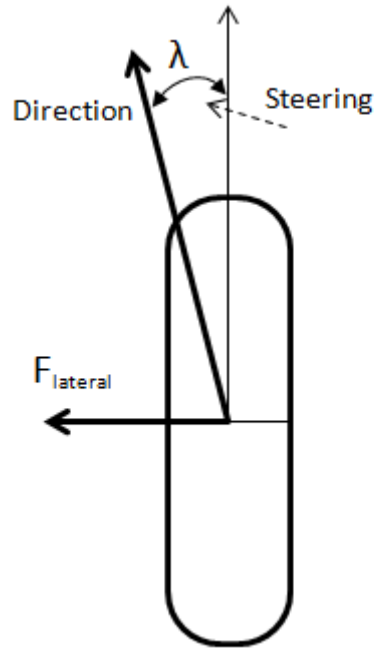


**Figure 4-6 Lateral Tire Force Generation**

As with longitudinal tire forces, Pacejka's Magic Formula can also be utilized and developed to fit experimental data of lateral force versus slip angle [14] [24] [26].

It is difficult and expensive to access tire testing equipment that can test for lateral force generation. Therefore, lateral force curves for the vehicle were estimated by dragging the vehicle across the surface on which the vehicle will be run. A force transducer was attached to the chassis and pulled at a constant angle in relation to the chassis at a steady speed. The encoders attached to the pods were utilized to maintain various angles at which the pods can be pulled. This represents the various slip angles of which the vehicle may operate. The force needed to balance the tire force and maintain a constant speed was measured using the force transducer at each slip angle. *Figure 4-7* shows an example test set-up.

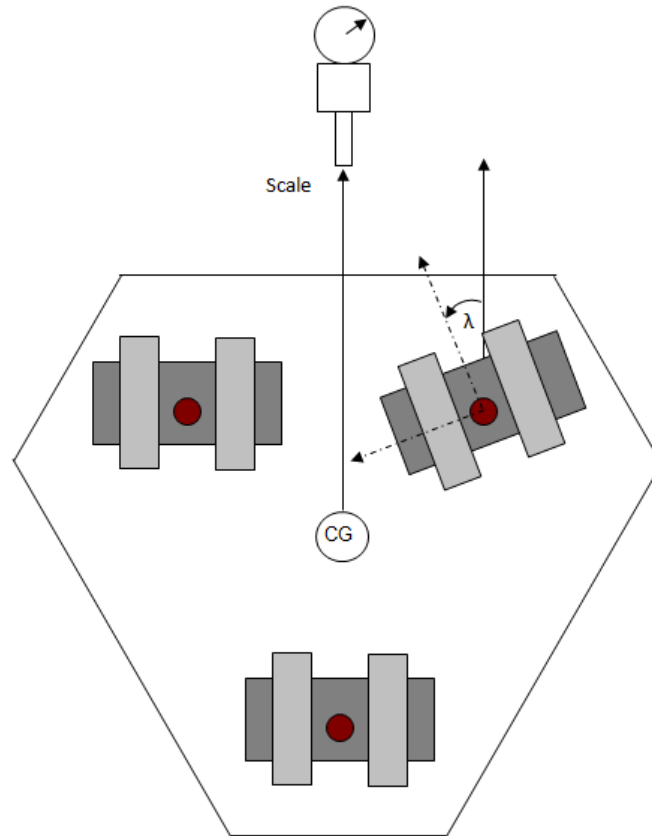


**Figure 4-7 Experimental Set-up for Measuring Lateral Force**

The results of the lateral tire force estimation tests are shown in *Figure 4-8*.

Similar to the longitudinal force estimation, Pacejka's tire model was fitted to this data for use in the simulation. This tire model can also be seen in *Figure 4-8*.

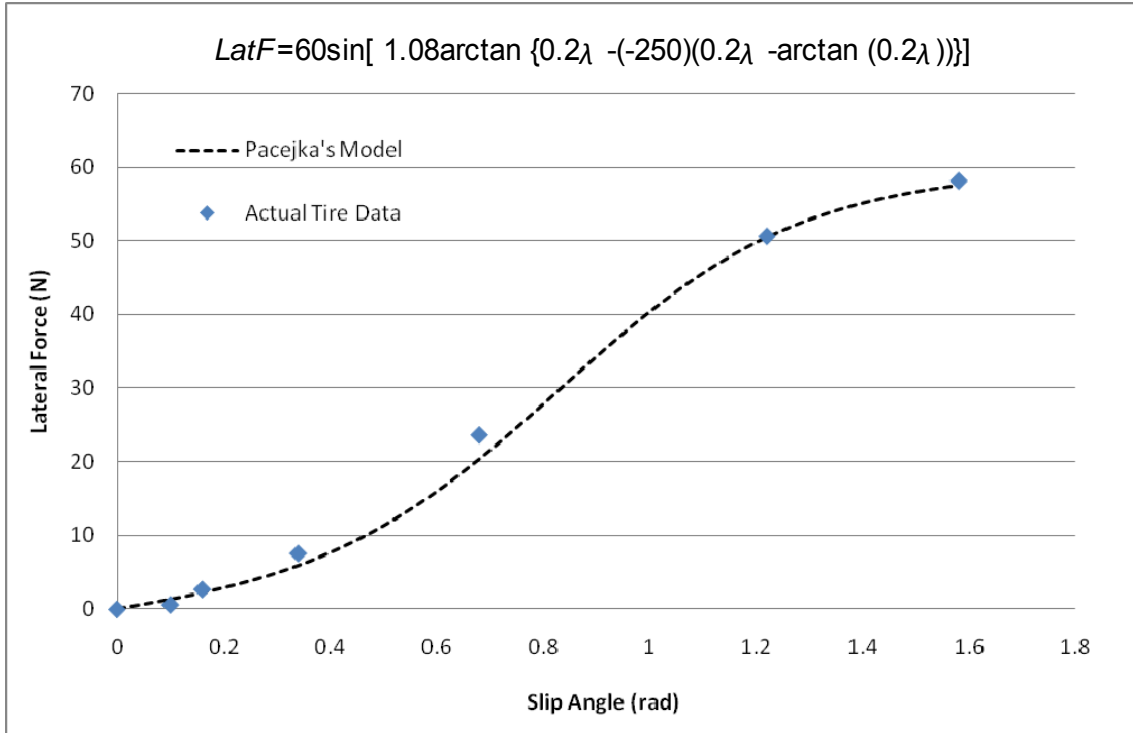


**Figure 4-8 Lateral Tire Force Data and Model**

### 4.3 Air Resistance

The test conducted to find rolling resistance was also used to determine air resistance. The linear coefficient of the average best-fit line is the drag force constant that will be used for simulation purposes.

Air resistance is normally proportional to the square of the vehicle velocity. However, the shape of the data sets shown in *Figure 4-1* does not show this relationship between force and velocity. This may be attributed to the noise in the data or because the vehicle is being run at such low speeds. The impact of air resistance may not clearly be seen due to the operating speeds being under 8 m/s. Even so, there is a definite resistive

force from the air which is modeled as the linear coefficient in the curve fit to the data and discussed in Section 4.2.1.

These resistance forces are significant enough that it is necessary that they be identified and included in the simulation. One thing that is important to realize is that the linear coefficient (here equal to 5.602 Ns/m) of the best-fit curve in *Figure 4-1*, shown in Section 4.2.1, is strictly speaking not the drag coefficient. This linear coefficient represents the total effect of vehicle geometry and air properties as shown in Equation 4-3. Our empirical data showed a linear relationship between the drag force and velocity which is in contrast with the more commonly assumed quadratic relationship.

$$Fd = \frac{1}{2}Cd * \rho * A * v^2 = 5.602 * v \quad (\text{Eq. 4-3})$$

It was decided that the time and effort needed to find the specific air drag coefficient,  $Cd$ , was too great. Furthermore, even if an air drag coefficient could have been estimated, it was felt that too many assumptions would have been taken, leading the estimate of the coefficient to be inaccurate at best. Furthermore, it was estimated that the cross sectional area,  $A$ , of the vehicle would not change greatly as the chassis rotates about the vertical axis. Air density,  $\rho$ , is more than likely constant for any given day, but may vary from day to day depending on atmospheric pressure and air temperature. As mentioned before, the vehicle is run indoors which will cut down on some of the day-to-day variation. Though the constant found from the coast down test is not representative of all driving conditions, the estimated constant should be sufficiently accurate for most driving scenarios.

#### 4.4 Closed-loop Motor/Wheel Speed Control Characterization

Though a tire model has been estimated, this is only one step in estimating how the vehicle will accelerate. It was decided to fit a “black-box model”, through the use of transfer functions, to describe the way the vehicle will accelerate. Transfer functions will capture how the vehicle accelerates when the motor controllers are in closed-loop speed control mode. Furthermore, this approach was taken since the motor and motor controller characteristics were unknown and because it prevents the use of complex calculations.

The idea is to use the transfer functions to capture the wheel / motor dynamics without spending a great deal of time trying to test, calculate, and validate how controllers and motors interact with each other and the rest of the vehicle. The input to the transfer function is a voltage (Volts) with the output being a wheel speed (rad/s). This acceleration model is responsible for generating the slip ratio. That slip ratio is responsible for generating a longitudinal tire force; the force that accelerates the vehicle.

For this test, the vehicle was accelerated and allowed to hit top speed. The vehicle was accelerated at several times at one volt intervals up to a maximum of five volts, applied as a step input. From there, acceleration profiles, a response to each step input, (for each voltage level) were averaged to generate one profile that should account for relatively little variations in road surface and various other test conditions. The actual result from that test, primarily the shape of the acceleration profile of the real vehicle, was used to calculate the transfer functions representing the motor / wheel dynamics. The result of real vehicle acceleration profiles and the transfer functions fitted are shown in *Figures 4-9 and 4-10*.

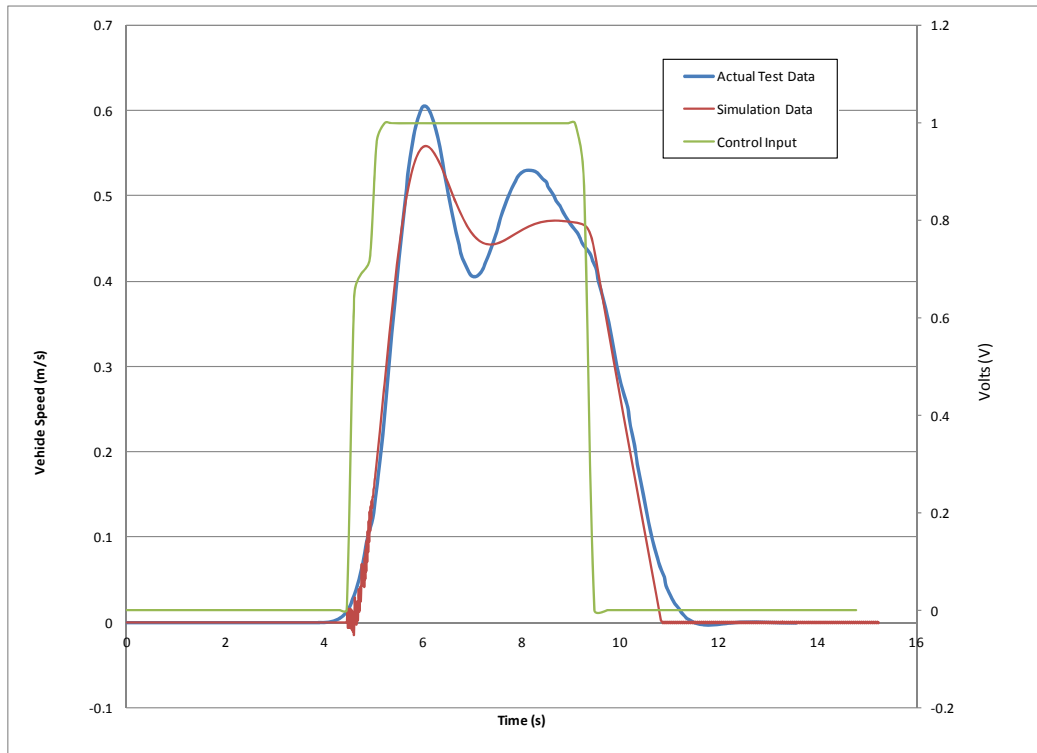


**Figure 4-9 1-Volt Straight-Line Acceleration Transfer Function (Step Input Response)**

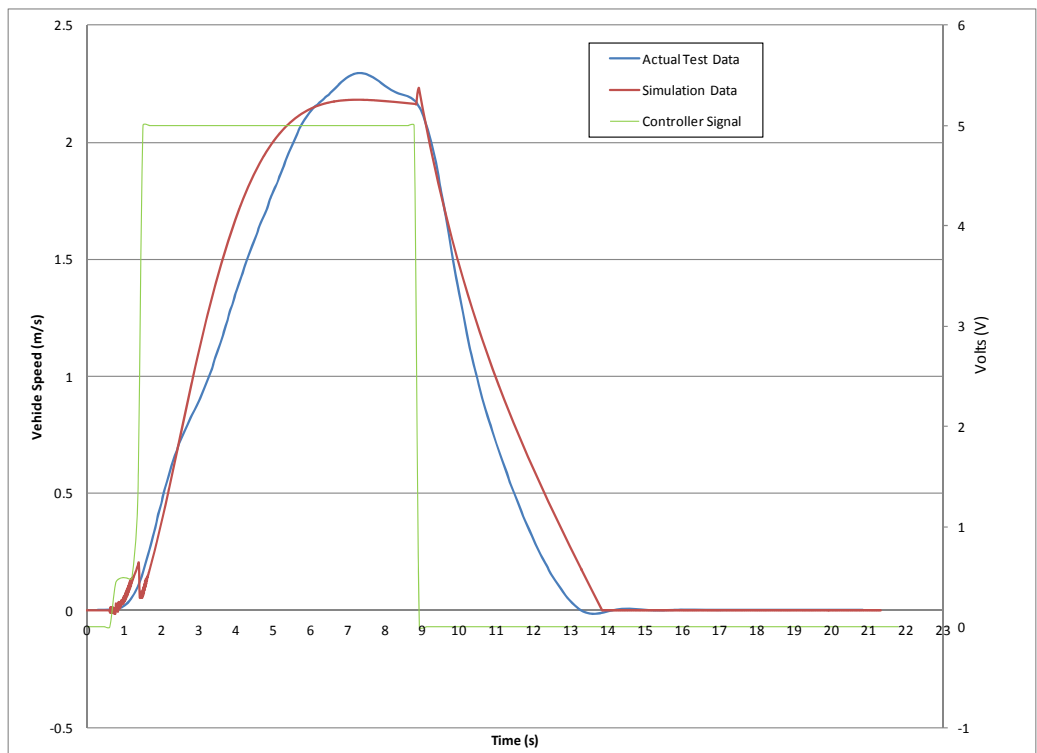


**Figure 4-10 5-Volt Straight-Line Acceleration Transfer Function (Step Input Response)**

It is important to keep in mind that the transfer functions do not fit the data perfectly. Instead, the transfer functions are designed to fit a variety of voltage inputs and therefore fit an average of voltage ranges. The reason these were not fit to a larger variety of inputs is due to the sheer number of possible inputs into the system. Though it would definitely increase the accuracy of the simulation, the benefit was thought not to outweigh the time requirement needed to determine every transfer function needed. After all, even slight variations in air pressure can affect how the vehicle accelerates.

As you can see, the way the vehicle accelerates depends on the voltage fed to the motor controllers. There are even slight differences between velocity profiles of one volt increments. The major difference between lower voltage velocity profiles and the higher velocity profiles is the overall shape of the profile and ultimately the order of the transfer function fitted to the data.

The velocity profiles exhibit second-order characteristics at lower voltage inputs while higher voltages tend to make the vehicle's acceleration profile look like a first-order system. Therefore, two transfer functions were fitted to the profile for use in the simulation. The switch between the two types of profiles happens at approximately 2.5 Volts. Again, the motor controller and the motor characteristics are unknown which is why the black-box approach was used to describe how the vehicle accelerates. The final transfer functions are shown in Equations 4-4 and 4-5.

$$TF(LV) = \frac{WheelSpeed(s)}{VoltInput(s)} = \frac{5.1 * 2.6302^2}{s^2 + (2 * 0.4107 * 2.6302)s + 2.6302^2} = \frac{rad / s}{Volt}$$

**Lower Voltage Transfer Function (Below 2.5 V) (Eq. 4-4)**

$$TF(HV) = \frac{WheelSpeed(s)}{VoltInput(s)} = \frac{s + 5}{1.5s^2 + 1.9s + 1} = \frac{rad / s}{Volt}$$

**Higher Voltage Transfer Function (2.5 V and above) (Eq. 4-5)**

The result of the multiplication in the numerator and denominator in Equation 4-4 was intentionally left incomplete. This better illustrates the dynamic characteristics associated with the second-order transfer functions. For example, the gain,  $K$ , is 5.1, the natural frequency,  $\omega_n$ , is 2.6302 rad/s, and the damping ratio,  $\zeta$ , is 0.4107.

## 4.5 Slip-ring Friction

Between the slip-ring plates are metallic tabs and concentric, circular metallic tracks which conduct electricity. These are meant to be in contact with one another as to allow signal flow between the top and bottom plates. This is what enables the pods to rotate 360 degrees without loss of signal and without tangling the electric wires.

Unfortunately, the contact between the upper and lower plates causes friction and induces a torque which resists the rotation of the pods. In order to accurately model the vehicle in simulation, this torque needed to be quantified. Recall that the torque that induces a pod to rotate is caused by the difference in road forces generated between the right and left wheels. The torque needed to rotate the pod must be higher than the resistive torque caused by the friction in the slip-rings. Therefore, tuning the control system, especially at the pod level, requires a fairly accurate model of the slip-ring friction.

To find this friction, a test was run that closely resembles the coast down procedure discussed in Section 4.3 regarding air resistance. An electric drill was used to

rotate a pod up to an angular speed of about 60 RPM. At this speed, the drill was removed and the pod was allowed to coast to a stop. The encoders were used to track the angular position in relation to the chassis as the pods coasted to a stop. The results of these tests are shown in *Figure 4-11*. The start time (0 sec) is the point at which the drill was removed from the pod.

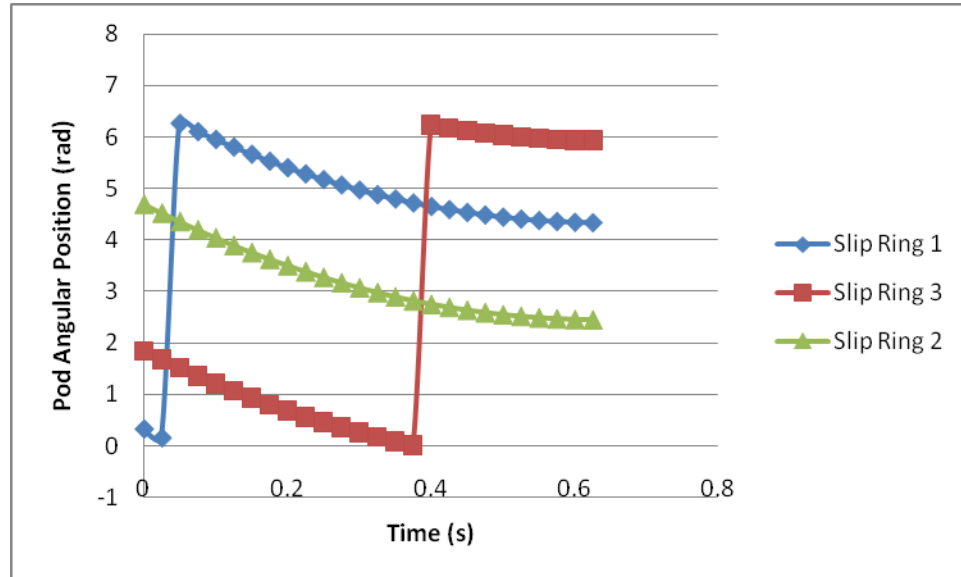


**Figure 4-11 Pod Coast-down Test Results**

As seen in *Figure 4-11*, a few of the tests ran through the “0” degree point during the test. That is why the graph shows a sudden jump in the angular position. For the two data sets that had recorded the encoder going through zero degrees, a portion of the graph was shifted vertically to meet with the rest of the data. From there, the pod’s angular position data was numerically differentiated to generate an approximate velocity graph for each of the pods. The result of these derivations can be seen in *Figures 4-12* through *4-13*.

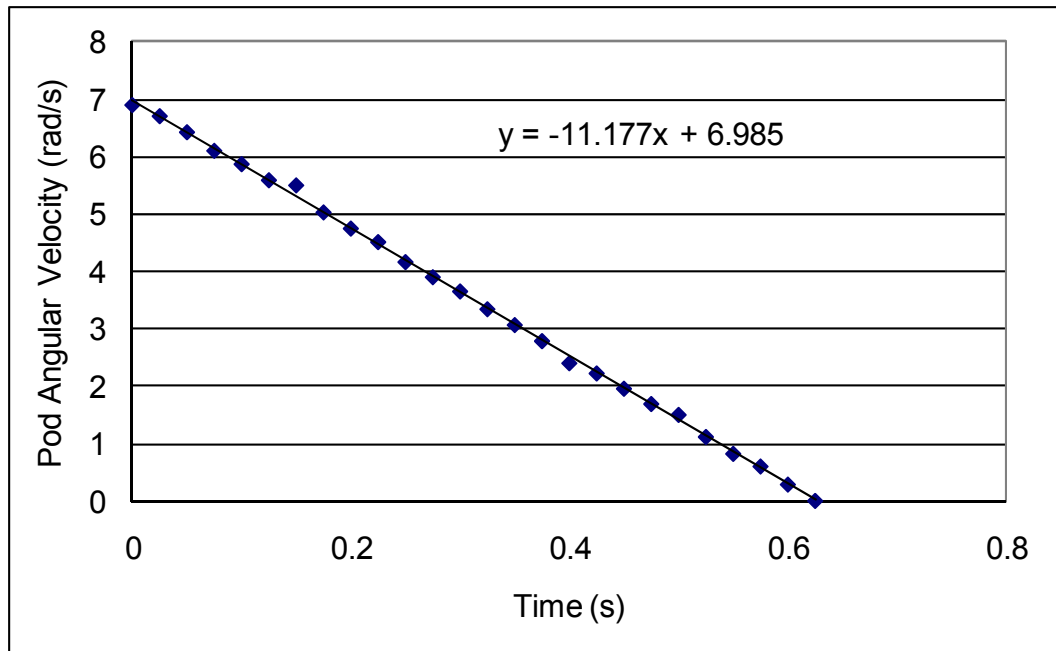


Figure 4-12 Pod 1 Coast-down Velocity Profile

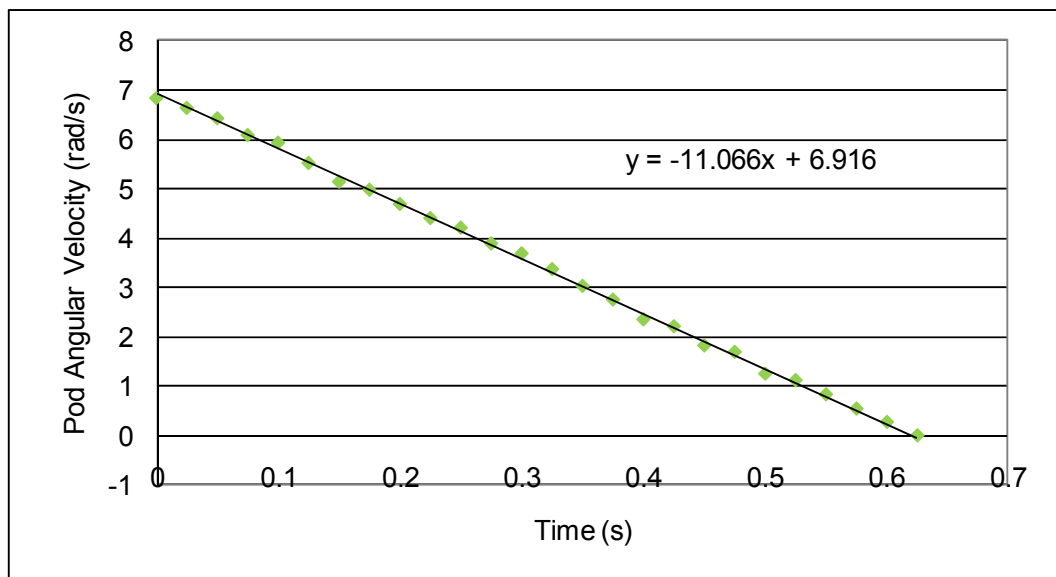
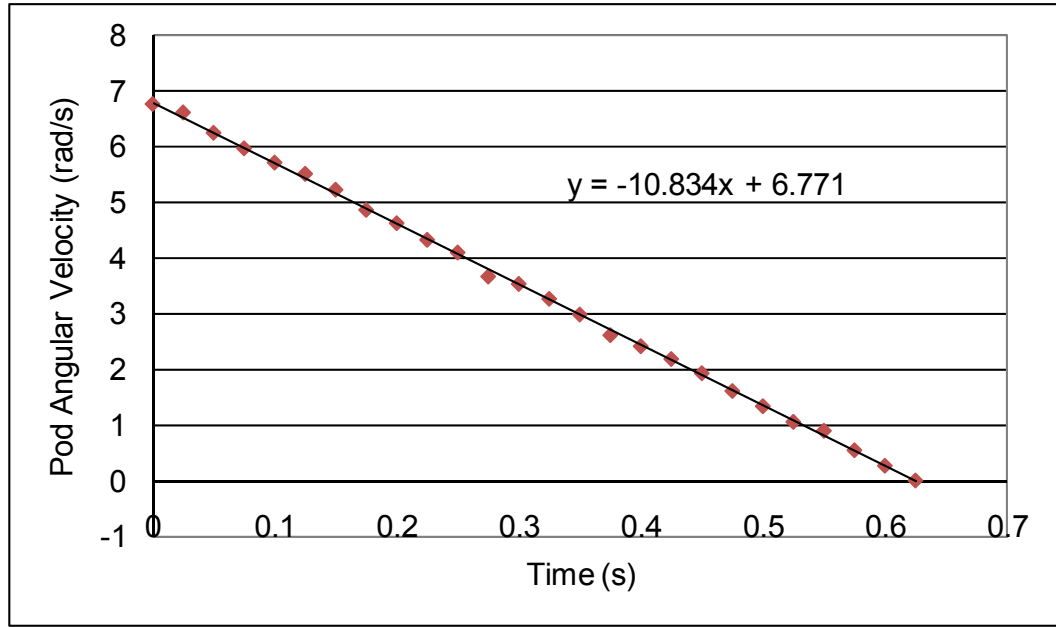


Figure 4-13 Pod 2 Coast-down Velocity Profile



**Figure 4-13 Pod 3 Coast-down Velocity Profile**

The velocity profile of each pod clearly shows a linear relationship which is a result of constant deceleration. The slope, determined by a best-fit line, for each pod's velocity profile is the deceleration for that particular slip-ring. Since angular deceleration was constant, the resistive torque was also constant and could be found using Equation 4-6.

$$T = I \ddot{\theta} \quad (\text{Eq. 4-6})$$

In Equation 4-6,  $T$  is the resistive torque generated by the slip-rings.  $I$  is the moment of inertia of one pod assembly and  $\ddot{\theta}$  is the angular acceleration. The moment of inertia is known from Section 2.7 which is approximately  $0.07238 \text{ kg-m}^2$ . The angular deceleration from each of the pods was averaged together for use in Equation 4-6. The angular deceleration multiplied by the moment of inertia of the pod yields the resistive torque in the slip-rings. Therefore, the resistive torque in the slip-rings is approximately

equal to the constant 0.8 Nm and changes sign to always oppose the direction of rotation of the pods.

## ***5. Simulation and Control***

### **5.1 Simulation and Control Overview**

In an attempt to save time, some aspects of the simulation vehicle were not modeled. A simulation that modeled all aspects of the vehicle would greatly increase both the time needed to develop the simulation and the time needed to run tests on the actual vehicle. It is also important to note that any test done on the vehicle while it is not equipped with a control system automatically increases the risk of premature failure of some component of the vehicle. This leads to increased cost and development time. Therefore it was decided to model the vehicle in one plane. In particular, the vehicle was modeled in the x-y plane as shown in *Figure 2-1*. This means that no pitch or roll characteristics are modeled in the simulation.

The simulation models the reaction forces of the tires and the vehicle's reaction to the summation of those tire forces. In particular, the simulation performs an analysis of the forces generated by each of the tires under both longitudinal and lateral slip conditions. The concept of how the tires generate forces in the longitudinal and lateral directions was discussed in Chapter 4.

All of the forces are only modeled in the x-y plane and are separated into its global x- and y-components. Each tire's summation of forces in both the global x- and y-components are applied directly at the point of contact of the tire with the floor. At this point, the forces are converted from the global coordinate frame to the local coordinate system of the tire. This ensures that the forces are applied either parallel (longitudinally) or perpendicular (laterally) to the tire.

The summation of forces at each tire creates an acceleration on each pod that can result in translational movement, rotational movement, or both. Chassis movement is a result of each pod's individual movement. At this point, wind forces are modeled and applied to the center of gravity of the chassis. The drag forces are a result of any movement of the chassis in the global x- and/or y-direction.

With all forces accurately modeled in the x-y plane, a control system could then be developed to help achieve the desired movement of the vehicle. Many approaches could have been taken for the control of the vehicle, but this particular approach concentrates on the control of each pod. The control of each individual pod was easier to implement into both the simulation and the real vehicle than the overall yaw rate and angular position of the chassis. The pods respond much quicker than the chassis by comparison and indirectly affect the movement of the chassis. In short, by controlling the pods, the chassis can also be controlled.

## **5.2 Control Strategy and Simulation Architecture**

The development of this simulation is motivated by a couple of applications. One reason for the simulation is that it provides a controlled environment in which to develop the control algorithms. Each given test in simulation can be run much more quickly than on the actual vehicle and does not expose the vehicle and its hardware to possible harm especially when conducting extreme maneuvers. Furthermore, the simulation can be adjusted to help isolate problems more easily than in the complex environment of the real world. A second reason for the simulation is that it allows testing of different vehicle

geometries and hardware. Such experimentation would require lengthy and expensive construction of hardware if it had to take place on a physical vehicle.

The structure of the simulation is consistent with the closed-loop control system structure described in Chapter 2. *Figure 5-1* again illustrates the overall structure of the vehicle system with control.

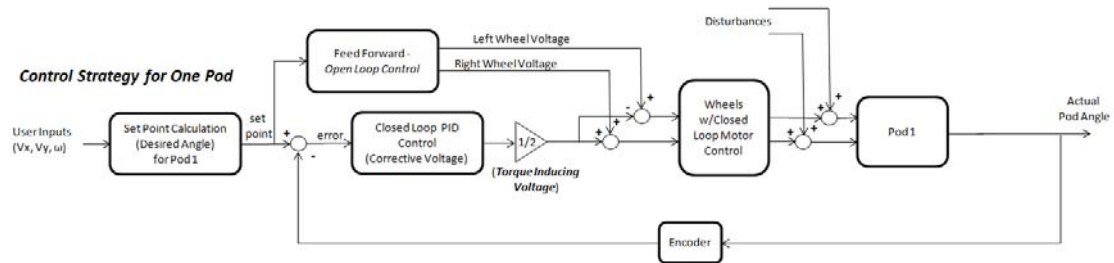


**Figure 5-1 Overall Vehicle Control Block Diagram w/ Control System**

The simulation is structured similarly to that of the Overall Vehicle VI presented in Chapter 3. This was done to assist with the co-development and maintenance of the simulation and the vehicle control software. This way any changes made to one can be easily implemented on the other since they share a similar structure. Again, the overall strategy is to take user inputs from the gaming controller and calculate desired pod angles based on those inputs. Each of the three pod angles is compared to its respective actual pod angle. The difference becomes the error which is then used in the feedback portion of the control system. This results in the correct alignment of the pods.

The feedforward portion of the control system uses just the desired pod angles to create movement in the chassis. When used together, the feedback and feedforward portions of the control system correctly aligns the pods and therefore helps the chassis move in a path closely resembling to that of the desired path of the user.

The work done in Chapter 4 provides the foundation for the simulation in providing the physical data on which to base the simulation models. The software package Simulink from MathWorks provides the simulation environment. Simulink is a multi-domain simulation software that interfaces with the software MATLAB, also from the MathWorks. The simulation as constructed makes extensive use of the SimMechanics extension to Simulink that is a tool for modeling mechanical systems. Use of the SimMechanics extension includes a blockset of mechanical components and characteristics and has the ability to handle physical signals on a system level. This implemented the majority of the dynamic equations. If not for this extension, the author have needed to generate the majority of the mathematical relationships in Simulink. This sped up the simulation build time and makes it easier to debug and understand. SimMechanics also makes the simulation more robust and less prone to algebraic loops. The finished simulation is shown *Figure 5-2*. This shows the overall simulation and the various sub-models. As this chapter progresses, each block or sub-model in the simulation will be discussed.



The presence of the M-file for use within the simulation allows the ability to easily alter vehicle parameters. This allows for rapid and inexpensive qualitative testing of the vehicle without the risk of harming the actual vehicle. This will be particularly useful for optimizing the performance of future builds of this type of vehicle.

### 5.3 Desired Pod Angles – Setpoint Generation

The user command signals (the desired x- and y-components of velocity and the desired angular velocity) are first sent to the Desired Pod Angles Sub-model. In this sub-model, the same mathematics and matrix operations laid out in Section 3.5, Equation 3-1 are performed. The result is a setpoint or desired angle for each pod based on the dimensions of the chassis and the control inputs from the user.

The difference between this Desired Pod Angles Sub-model in the simulation and the sub-model in LabVIEW is the way the calculation is performed. In LabVIEW, the matrix calculations are performed via a built-in block. In Simulink, the desired pod angle sub-model is implemented by Simulink's ***Embedded MATLAB Function*** block. Here, the mathematical operations as described in Section 3.5, Equation 3-1 can simply be typed out in the same manner they would be in the MATLAB command window (MATLAB can perform matrix operations). *Figure 5-4* shows where this sub-model is implemented in the overall simulation architecture.



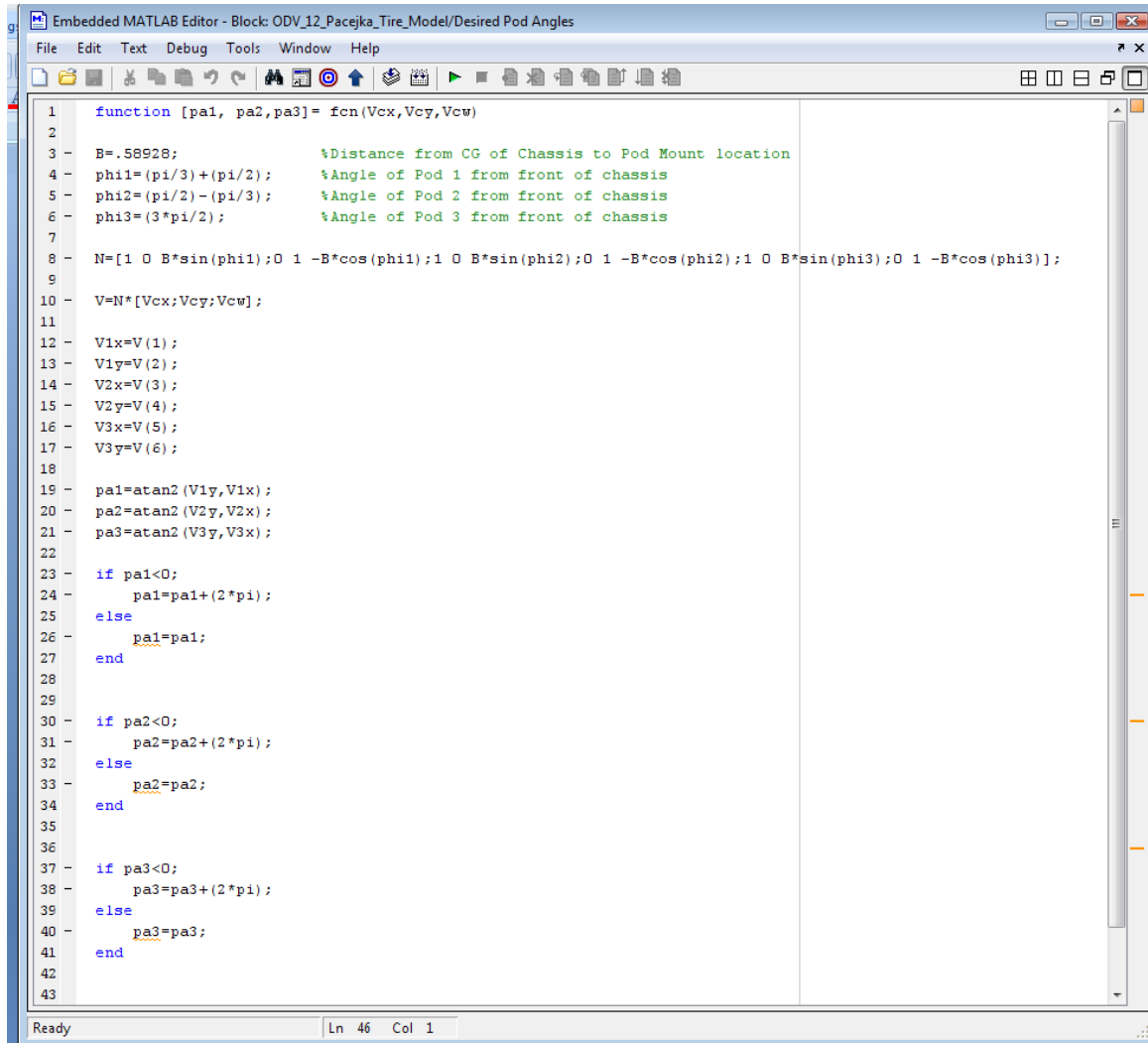


Figure 5-5 Desired Pod Angles Sub-model Contents

## 5.4 Inverse Kinematics Model - Feedforward Control

The Inverse Kinematics Sub-model is very similar to the Desired Pod Angles Sub-model. This sub-model constructs the 6x6 *J-matrix* (which includes the *N-matrix*) described in Section 3.6, Equations 3-2 and 3-3. The *J-matrix* is based on the physical dimensions of the pod and transforms the x- and y-components of the velocity of each pod into left and right wheel speeds (which are proportional to the voltages commanded

to the corresponding motors). Along with  $J$ -matrix, these voltages are calculated based on the desired pod angles, the  $N$ -matrix, and the user inputs.

The pod angles are input from the Desired Pod Angles Sub-model. This forces the Inverse Kinematics Sub-model to output wheel voltages that are not dependent on the current angle of the pods. This means that the sub-model will produce output commanded wheel speed that is independent of the current position of pod in relation to the chassis. This sub-model, therefore, adds a feedforward element to the overall vehicle control. Constructing the  $J$ -matrix based on the desired pod angles, rather than the actual pod angles, helps to decouple the feedforward controller from the feedback controller and makes the control system easier to tune. *Figure 5-6* shows where this sub-model is located in the overall simulation.

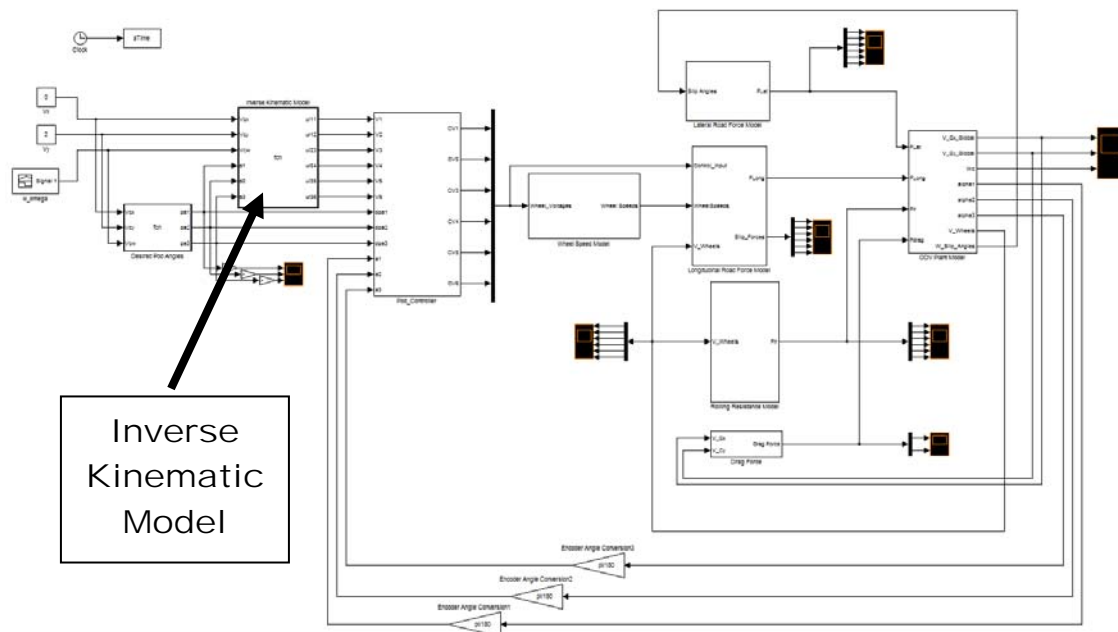
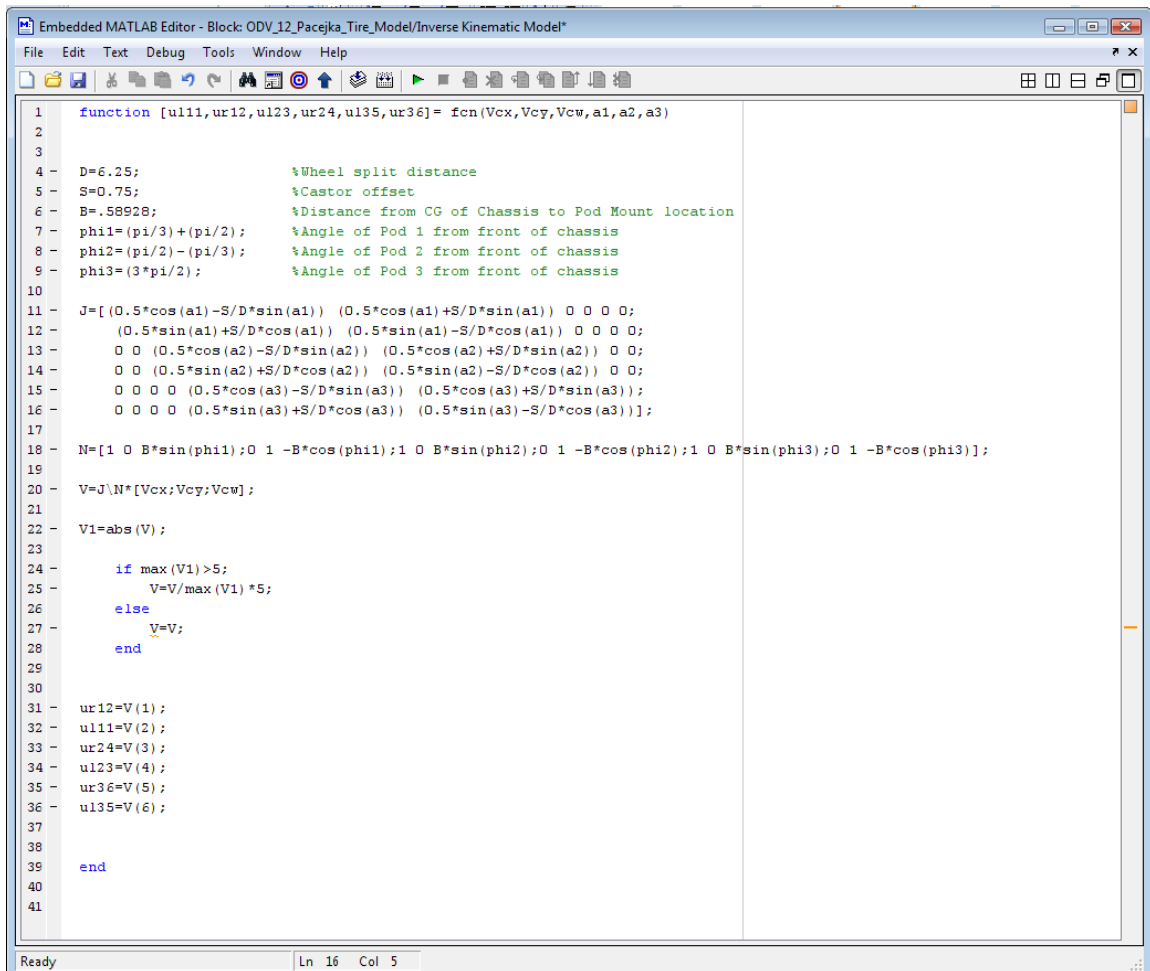


**Figure 5-6 Inverse Kinematics Sub-model Location**

In a similar manner to how the Desired Pod Angles Sub-model was implemented, the Inverse Kinematics Sub-model is also constructed using Simulink's *Embedded*

**MATLAB Function** block which allows the equations to be written using MATLAB syntax. The functionality of this sub-model is similar to the Open-Loop Control System VI (feedforward portion of the control system) discussed in Section 3.6, but is not carried out in the same way. Instead, the Inverse Kinematics Sub-model is written as a function rather than set up as a block diagram. *Figure 5-7* shows the contents of the Inverse Kinematics sub-model.



```

1 function [ul11,ur12,ul23,ur24,ul35,ur36]= fcn(Vcx,Vcy,Vcw,a1,a2,a3)
2
3
4 D=6.25; %Wheel split distance
5 S=0.75; %Caster offset
6 B=.58928; %Distance from CG of Chassis to Pod Mount location
7 phi1=(pi/3)+(pi/2); %Angle of Pod 1 from front of chassis
8 phi2=(pi/2)-(pi/3); %Angle of Pod 2 from front of chassis
9 phi3=(3*pi/2); %Angle of Pod 3 from front of chassis
10
11 J=[(0.5*cos(a1)-S/D*sin(a1)) (0.5*cos(a1)+S/D*sin(a1)) 0 0 0 0;
12 (0.5*sin(a1)+S/D*cos(a1)) (0.5*sin(a1)-S/D*cos(a1)) 0 0 0 0;
13 0 0 (0.5*cos(a2)-S/D*sin(a2)) (0.5*cos(a2)+S/D*sin(a2)) 0 0;
14 0 0 (0.5*sin(a2)+S/D*cos(a2)) (0.5*sin(a2)-S/D*cos(a2)) 0 0;
15 0 0 0 (0.5*cos(a3)-S/D*sin(a3)) (0.5*cos(a3)+S/D*sin(a3));
16 0 0 0 (0.5*sin(a3)+S/D*cos(a3)) (0.5*sin(a3)-S/D*cos(a3))];
17
18 N=[1 0 B*sin(phi1);0 1 -B*cos(phi1);1 0 B*sin(phi2);0 1 -B*cos(phi2);1 0 B*sin(phi3);0 1 -B*cos(phi3)];
19
20 V=J\N*[Vcx;Vcy;Vcw];
21
22 V1=abs(V);
23
24 if max(V1)>5;
25 V=V/max(V1)*5;
26 else
27 V=V;
28 end
29
30
31 ur12=V(1);
32 ul11=V(2);
33 ur24=V(3);
34 ul23=V(4);
35 ur36=V(5);
36 ul35=V(6);
37
38
39 end
40
41

```

**Figure 5-7 Inverse Kinematics Sub-model**

## 5.5 Pod Control - PID Controller

In general, the closed-loop controller is meant to be used in conjunction with the feedforward controller. With this control structure, however, the vehicle drives best when the pods are close to their setpoints. That is why the control software, for both the simulation and the real vehicle, gives the option to turn the feedforward control “off,” especially when there is a large difference between the actual pod angles and their setpoints. Once the pods are close to their setpoints, the feedforward controller (the inverse kinematics) can be turned back “on.” *Figure 5-8* shows where the Pod Control Sub-model is positioned in the simulation.

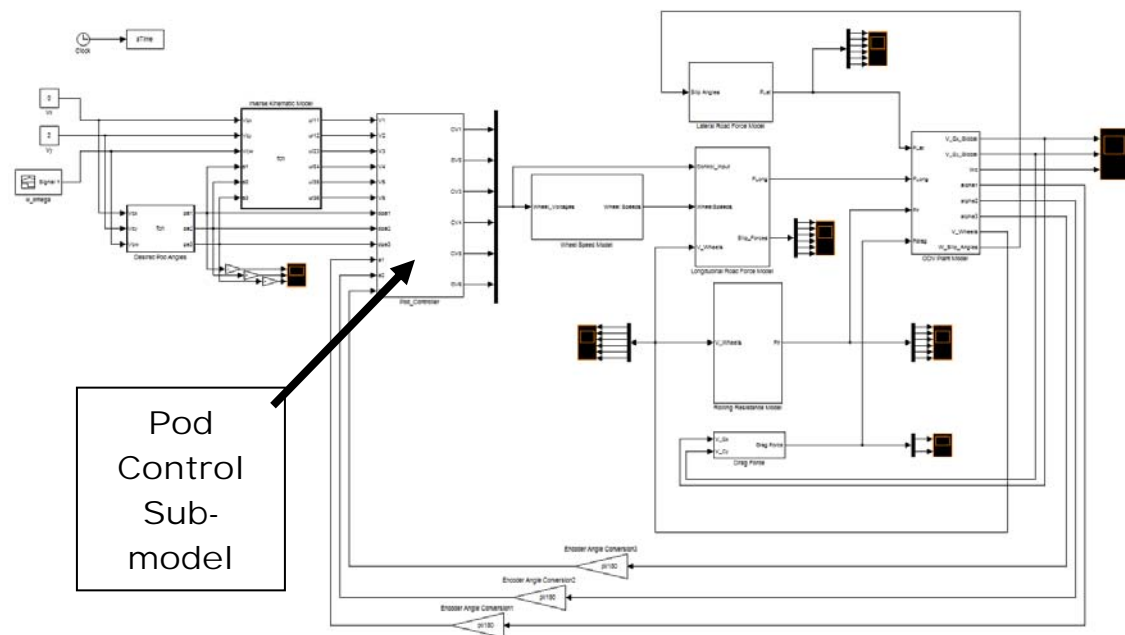


**Figure 5-8 Pod Control Sub-model Location**

The Pod Control Sub-model first reads in the setpoints, actual pod angles, and the feedforward control voltages. Each pod angle error, the difference between a setpoint and the corresponding actual pod angle, is conditioned so that the input-output relationship is linear. This is a much more robust system for calculating control effort

and direction than using the raw error alone. The method employed is the same as described in Section 3.7.

The Pod Control Sub-model has a similar structure to the Closed-loop Control VI in LabVIEW and operates in the same manner. The Pod Control Sub-model is shown in *Figure 5-9*.

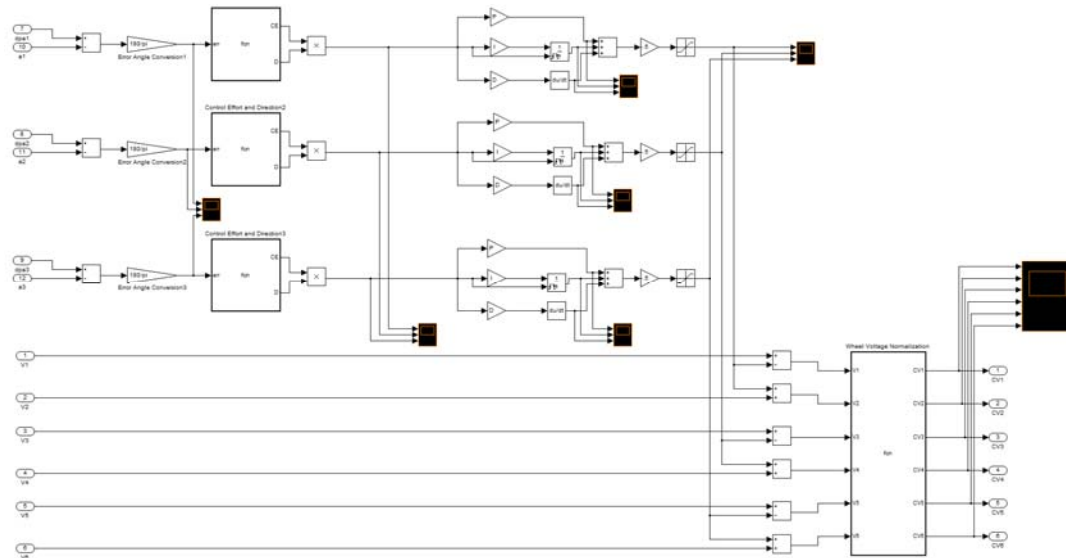


**Figure 5-9 Pod Control Sub-model**

In the Pod Control Sub-model, the errors are used to calculate for each pod a control effort and a direction, clockwise or counter-clockwise, that drive how each pod rotates. As described in Section 3.6, the maximum control effort is achieved when a pod is 180 degrees from its setpoint. The pods, as a default, are to turn clockwise when the pods are 180 degrees from a setpoint.

The feedback control effort for each pod is divided by two and added to the corresponding feedforward control command. Half of the control effort is subtracted from the left wheel and the other half is added to the right wheel. This induces a torque in the pod which will cause it to rotate. The feedback dynamics are a result of the

proportional, integral, and derivative terms at the top, middle of *Figure 5-9*. Built-in Simulink ***Integrator*** and ***Derivative*** blocks were employed for implementing the control logic. The ***Integrator*** block is configured to reset the integrated error once the actual angle has passed the setpoint.

A proportional-integral-derivative (PID) controller was chosen rather than a PI or PD controller. Early iterations of the controller only included the proportional and integral terms. The integral term was necessitated by the desire that the pod angles have zero steady-state error. The integral term helps to overcome the slip-ring friction present in all of the pods.

As both the vehicle and the simulation were tested, it became evident that the derivative term was necessary. The derivative term had the effect of adding damping to the system. This proved important since the position of the pods suffered severe overshoot in early iterations of the controller, thereby making the vehicle difficult to drive.

As a starting point, the gains were tuned based on the Ziegler-Nichols method, which is shown in *Table 5-1*, and were later finely tuned through trial and error.

Control Method	$K_p$	$K_i$	$K_d$
PID	$K_u/1.7$	$P_u/2$	$P_u/8$

**Table 5-1 Ziegler-Nichols Method for Tuning Control Gains [28]**

With the Ziegler-Nichols method, the proportional gain,  $K_p$ , is increased (with  $K_i$  and  $K_d$  set to zero) until the system (pods) begins to oscillate with constant amplitude. This proportional gain is then called the ultimate gain,  $K_u$ .  $K_p$  is then calculated by dividing the ultimate gain,  $K_u$ , by 1.7. The period of oscillation is labeled as  $P_u$  and is used in the calculation of the integral gain,  $K_i$ , and the derivative gain,  $K_d$ . Again, it is important to

keep in mind that this method was used as a starting point and these gains were not the ones ultimately used on board the vehicle.

All additional tuning was done in simulation prior to testing the gains on the real vehicle. In general, the vehicle was tuned to have as little overshoot as possible. Tuning the vehicle with as little overshoot as possible was chosen because it was thought that the vehicle would be more predictable to drive. This means that the derivative term ended up being higher and the integral and proportional terms both ended up being lower than chosen by the Ziegler-Nichols method.

The derivative term was a balancing act between finding enough damping in the system and not creating an excessive amount of “kick” when the setpoint suddenly changes. The proportional term was chosen based on what brought the pod to its setpoint as quickly as possible without resulting in a large amount of overshoot. The integral term was tuned to eliminate steady-state error within a reasonable amount of time and without causing a great deal of oscillation in the system.

Again, a numerical or standardized method associated with tuning the gains was not used because of the nature of the system. Instead, gains were chosen based on what made the vehicle drive well in regards to the preference of the user. Of course this means that the gains may change depending on the needs/wants of the driver. If a standardized set of gains are required for the vehicle, then an in-depth study on the preferences of several users is recommended.

The last operation of the Pod Control Sub-model is to make sure that the motors do not saturate. Therefore, the corrected wheel voltages go into another ***Embedded MATLAB Function*** block where the commanded voltages (proportional to wheel speed)

are normalized to five volts or less. The ***Embedded MATLAB function*** block is in the lower right hand corner of the Pod Control Sub-model as shown in *Figure 5-9*. The content of the Wheel Voltage Normalization block is shown in *Figure 5-10*. After the wheel voltages are normalized, they are output to the main simulation block diagram and are routed to the Chassis and Wheel Dynamics sub-models.

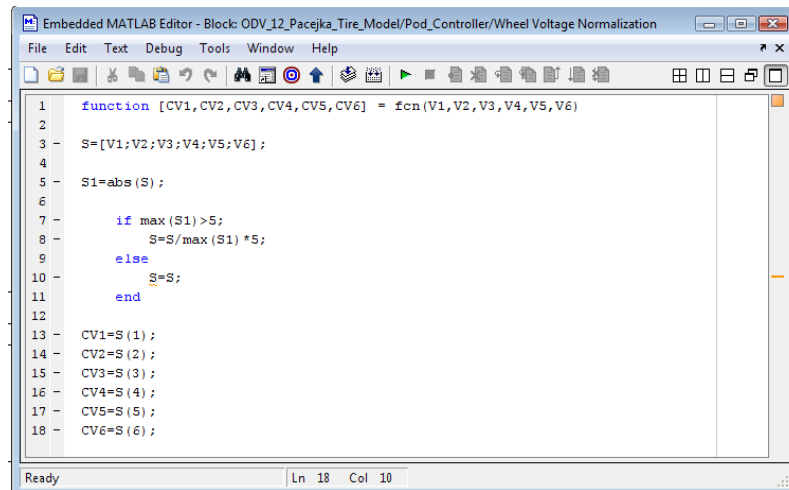


**Figure 5-10 Wheel Voltage Normalization Function**

Currently, the only way to change the weighting between the feedforward control and feedback control voltages is to alter all of the PID gains by a given factor. The voltage level was fairly consistent during actual vehicle and simulation testing. Therefore, the weighting of the feedforward and feedback control was not necessary. However, as the representative operating voltage levels increase or decrease, the weighting (proportion) of the feedforward to the feedback control voltages may need to be changed. This topic is discussed in Chapter 7.

## 5.6 Wheel Speed Model Sub-model - Transfer Functions

The corrected motor voltage commands (proportional to speed) are sent from the Pod Control Sub-model directly to the Wheel Speed Model Sub-model. This model is located approximately in the upper middle of the simulation main screen as shown *Figure 5-11*.

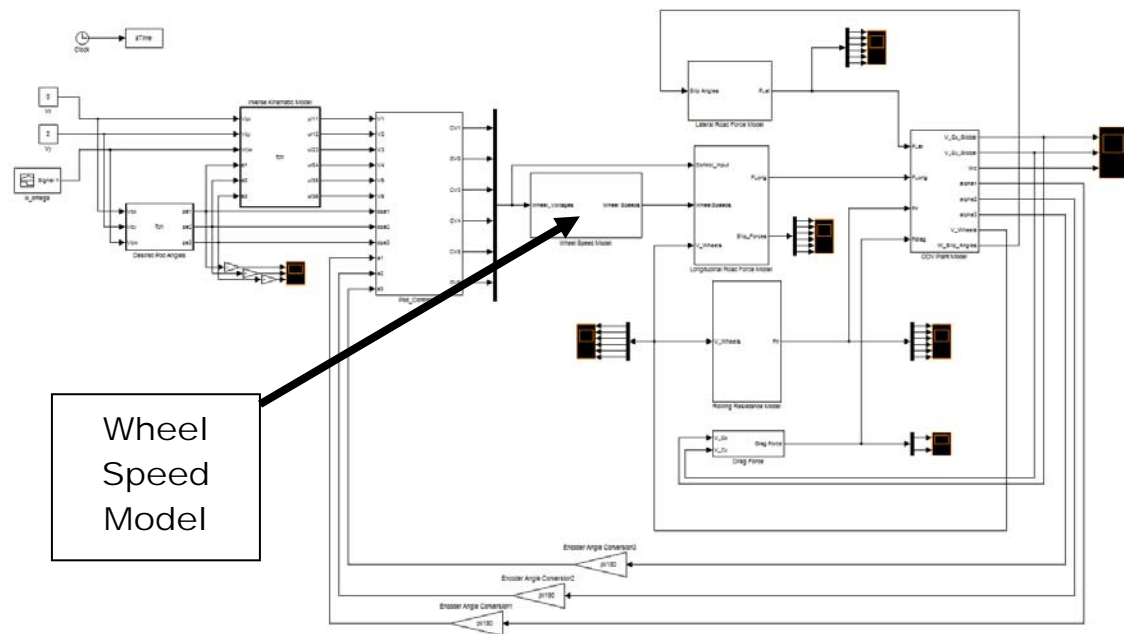


**Figure 5-11 Wheel Speed Model Sub-model Location**

The Wheel Speed Model Sub-model houses two transfer functions. The transfer functions, one low voltage and one high voltage, are responsible for characterizing how the wheels accelerate. The two transfer functions are covered in detail in Section 4.4. In the Wheel Speed Model Sub-model, there are a total of 12 transfer function blocks, two for each wheel. If the control signal to the motor is less than 2.5 volts, the low-voltage transfer function, as mentioned in Section 4.4, Equation 4-4, is utilized. The high-voltage transfer function, stated in Section 4.4, Equation 4-5, is used if the voltage is 2.5 volts

and above. *Figure 5-12*, shows how the block diagram is set up in the Wheel Speed Model Sub-model.

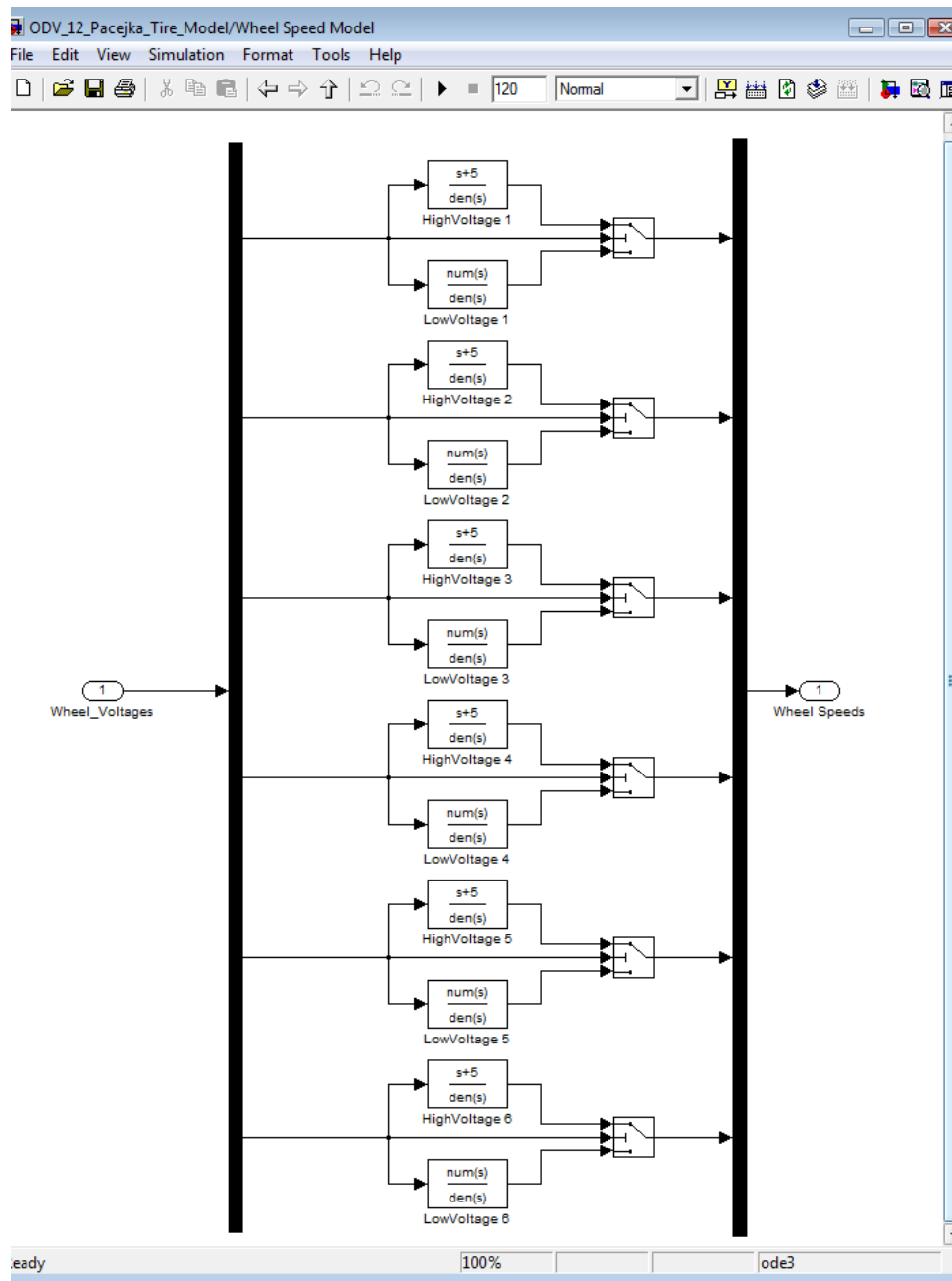


**Figure 5-12 Wheel Dynamics Sub-model Block Diagram**

The inputs to the sub-model are the six wheel voltages which are bundled as one signal. They are split into individual wheel voltages through the use of Simulink's

**Demux** block (which *unbundles* combined signals running on a single Simulink “wire”) and then routed to the transfer functions of the individual wheels. The input to the transfer function is a corrected motor voltage, from the closed-loop controller. The output is a wheel speed in rad/s. The six signals go into a **Mux** block (which *bundles* multiple Simulink signals into a single “wire”) just before being routed back into the vehicle-level portion of the simulation. The **Mux** and **Demux** blocks are employed to make the simulation easier to understand and clear of too many individual signal wires. The sub-model could have just as easily been set up with six inputs and six outputs on either side of the sub-model.

The corrected motor voltages, besides flowing into the Wheel Speed Model Sub-model, are also input to the longitudinal tire model. The reason for this is due to the nature of the transfer functions. Both the high- and low-voltage transfer functions describe how the wheels are driven (accelerate), but they do not capture how they decelerate when not being driven. Instead, the air drag and rolling resistance elements affect how the vehicle decelerates and these forces yield the resulting deceleration profile. Therefore, when the longitudinal tire model sees that the control signal is set to zero volts, it automatically switches the longitudinal tire force to zero. This is done because when the wheels are not driven (or braked) the level of slip and the resulting longitudinal force is approximately zero. Under these conditions, the vehicle will coast to a stop under the rolling resistance and air drag forces. This is further explained in Section 5.7.1

## 5.7 Tire Model

The purpose of the tire model is three-fold. The tire model includes two functions and a signum function. This affects how the vehicle accelerates longitudinally and corners laterally. Of course, the vehicle is always opposed by rolling resistance. Each function of the tire model is divided into its own sub-model. This adds a higher level of understanding and made altering the overall model easier. Each sub-model outputs six forces, one for each wheel, that ultimately affect the movement of the vehicle.

Eventually, all of the forces are routed to the plant model. Inside the plant model each of the forces are input to their respective wheel model. The longitudinal and resistive forces act parallel to the direction in which the tire rolls, while the lateral force acts perpendicular to the other two forces. The longitudinal tire model, the lateral tire model, and the rolling resistance model are shown in *Figure 5-13*.

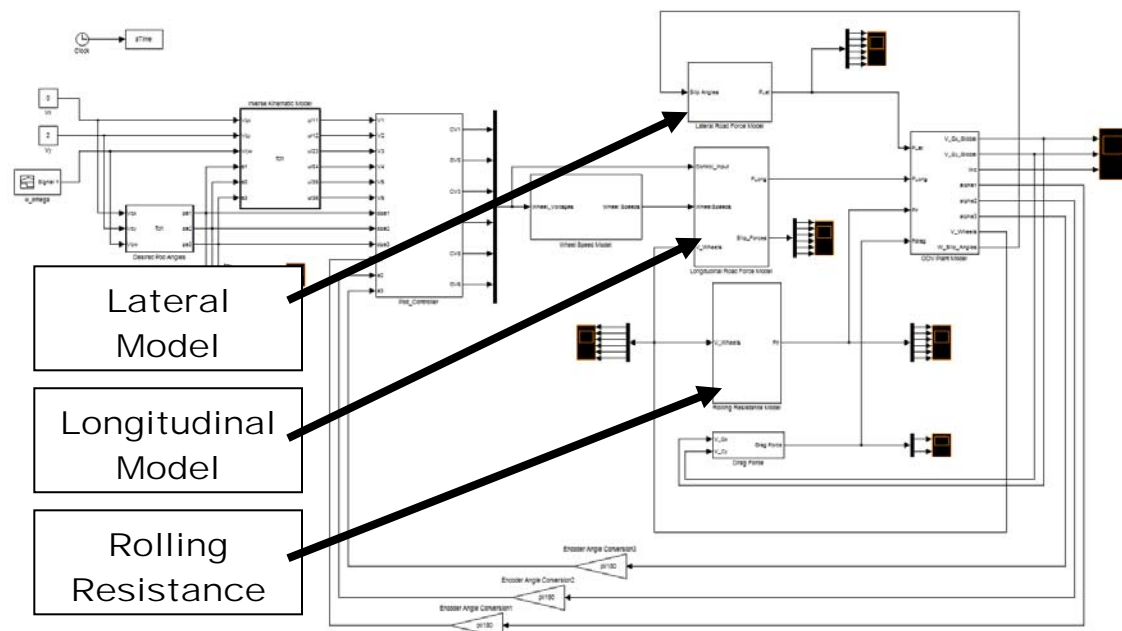
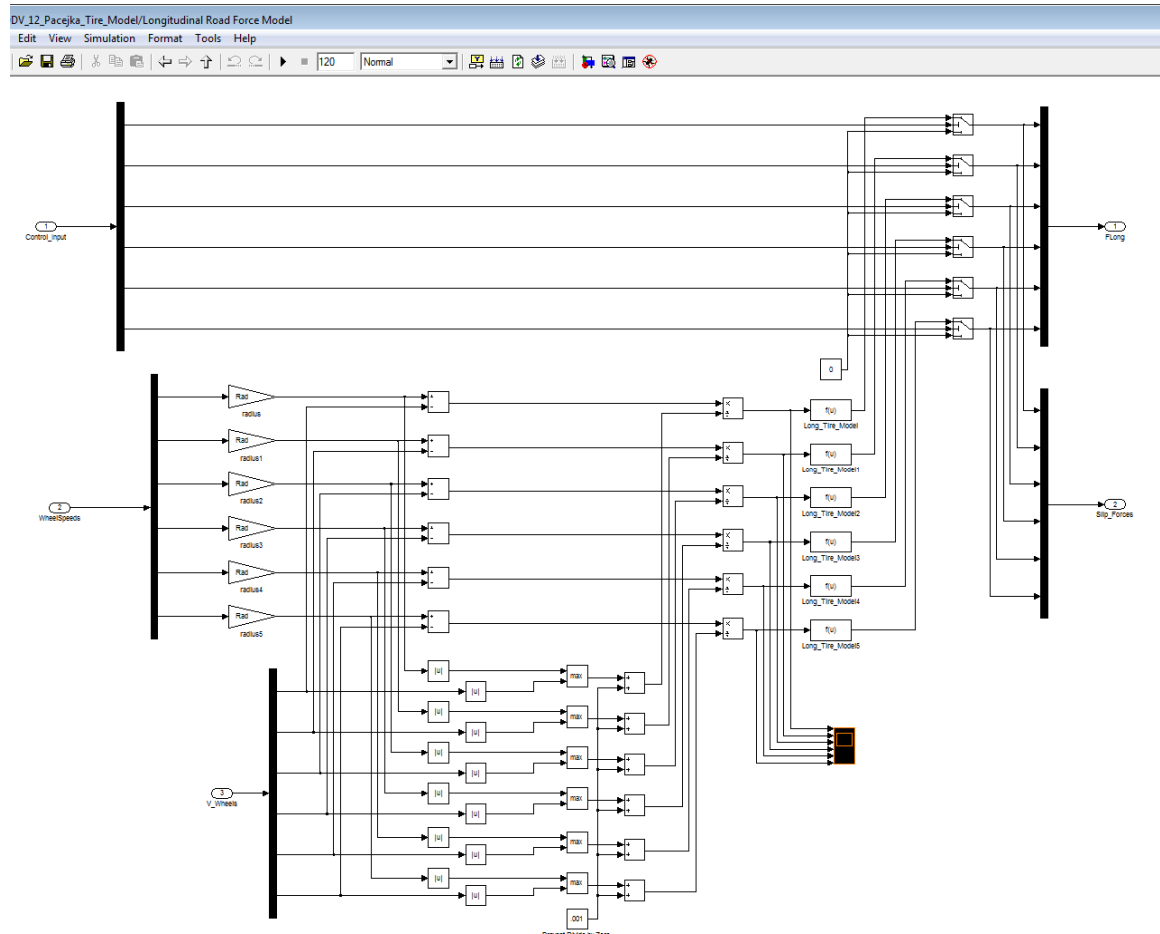


Figure 5-13 Tire Sub-model Locations

### 5.7.1 Longitudinal Tire Model

As discussed in Section 4.2.2, the Longitudinal Tire sub-model is the reason why the model is able to accelerate and translate in the longitudinal direction. The tire model in the simulation is a block diagram representation of Equation 4-1 in Section 4.2.2. The longitudinal model is shown in *Figure 5-14*.



**Figure 5-14 Longitudinal Tire Sub-model**

In the sub-model, the corrected voltage commands, the angular wheel speeds from the Wheel Speed Model Sub-model, and the actual translational speeds of the wheels from the ODV Plant sub-model are all inputs. The control command is at the top of the sub-model and is there to trigger the longitudinal force to be set to zero. As described in

Section 5.6, when the wheels are not driven (or braked) the level of slip and the resulting longitudinal force is approximately zero, hence the vehicle decelerates due to wind resistance and rolling resistance.

If a corrected voltage of zero volts was given to the transfer functions, the wheel speeds would coast down in a way that is similar to how the wheels accelerate. This is not correct, particularly in the case of a second-order transfer function. Either the high- or low-voltage transfer function interprets a zero voltage as a step input and will respond as such. For example, a second-order transfer function would simulate a coast down maneuver as having a wheel speed profile that oscillates around 0 m/s. In the real vehicle, this would not be possible unless the actuators, motors, forced the vehicle to do so. Furthermore, a wheel deceleration profile based on transfer functions might resemble a brake force from the tires. Again, this is not possible since the actual vehicle has no braking function.

The wheel speeds from the transfer functions are brought in on the middle, left side of the sub-model. Just below the angular wheel speeds from the transfer functions, the translational wheel speeds from the ODV Plant Sub-model, are also read into the sub-model. The block diagram represents Equation 4-1 in 4.2.2. The difference between the angular speed and the translational speed divided by the translational speed gives the slip ratio for an individual wheel.

Ultimately, the tractive force the tire generates is a function of the slip ratio. The tire model was found experimentally and fitted with a Pacejka's magic tire formula, Equation 4-2 in Section 4.2.2. In section 4.2.2, it was mentioned that Pacejka's magic tire formula was based on a minimum of 4 constants,  $B$ ,  $C$ ,  $D$ , and  $E$ . For this particular

tire,  $B$  is 3.5,  $C$  is 0.8,  $D$  is 70, and  $E$  is -0.2. Pacejka's tire model, in conjunction with the aforementioned constants, creates a force versus slip ratio relationship that fits the actual tire data, shown in *Figure 4-5*. In the sub-model, this is represented by a user defined function, labeled Long\_Tire\_Model, which treats the slip ratio as the independent variable and outputs the longitudinal tire force. This force is then routed to the ODV Plant Sub-model.

### 5.7.2 Lateral Tire Model

The lateral tire sub model, shown in *Figure 5-15*, is simpler than the longitudinal model.

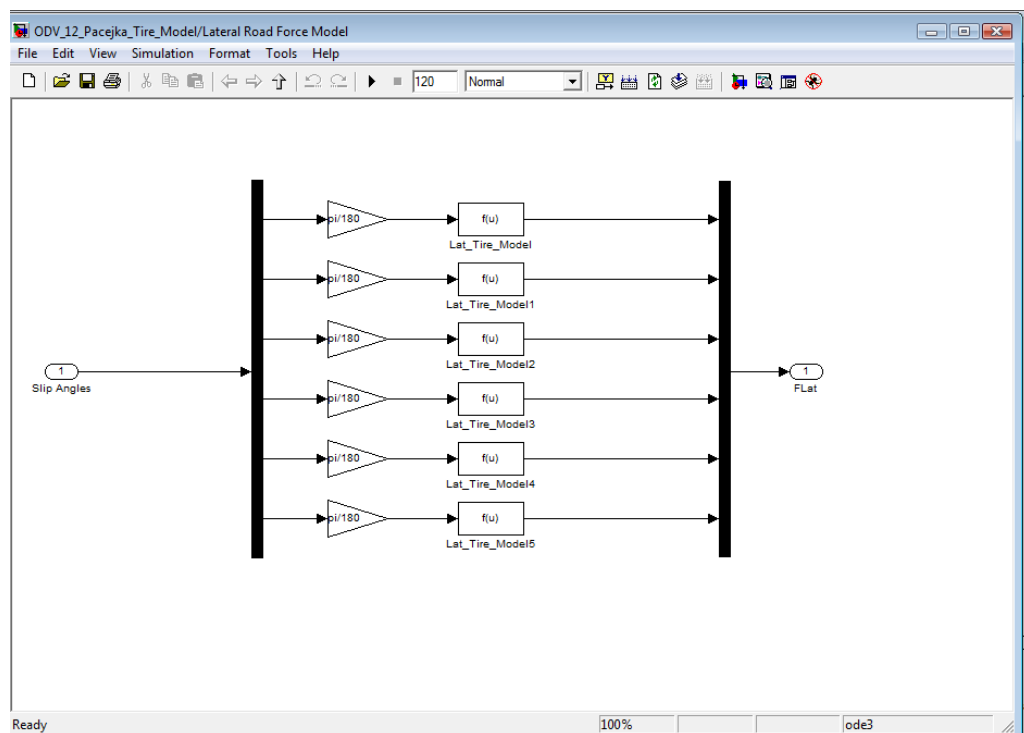


**Figure 5-15 Lateral Tire Sub-model**

Similar to the longitudinal tire model, the lateral tire force was found experimentally. This experiment is described in Section 4.2.3. Pacejka's magic tire formula was used to

fit the experimental data. The formula fitted to the data was placed into an ***Embedded MATLAB Function*** within the simulation, labeled Lat\_Tire\_Model.

The overall shape of the data is the same as the longitudinal tire model, but the constants,  $B$ ,  $C$ ,  $D$ , and  $E$  are slightly different.  $B$  is 0.2,  $C$  is 1.05,  $D$  is 60, and  $E$  is -250. Unlike the longitudinal tire model, the independent variable in the lateral model is a slip angle calculated in the ODV Plant Sub-model. After the lateral force is calculated with the ***Embedded MATLAB Function***, the force signals are output to the high-level model and routed to the ODV Plant Sub-model.

### **5.7.3 Rolling Resistance**

The rolling resistance was found by measuring the deceleration of the vehicle during a coast-down maneuver. The deceleration is a result of resistive forces which can be calculated using the mass of the vehicle. The force registered just before the velocity falls to zero is the rolling resistance. This was described in detail in Section 4.2.1. The rolling resistance is represented as a signum function multiplied by the rolling resistance constant found in the experiment conducted in Section 4.2.1. The rolling resistance is modeled to resist the direction of motion of the tires which is why the rolling resistance constant is shown as negative (-) 2.564 in *Figure 5-16*. *Figure 5-16* shows the block diagram representation of the rolling resistance model.

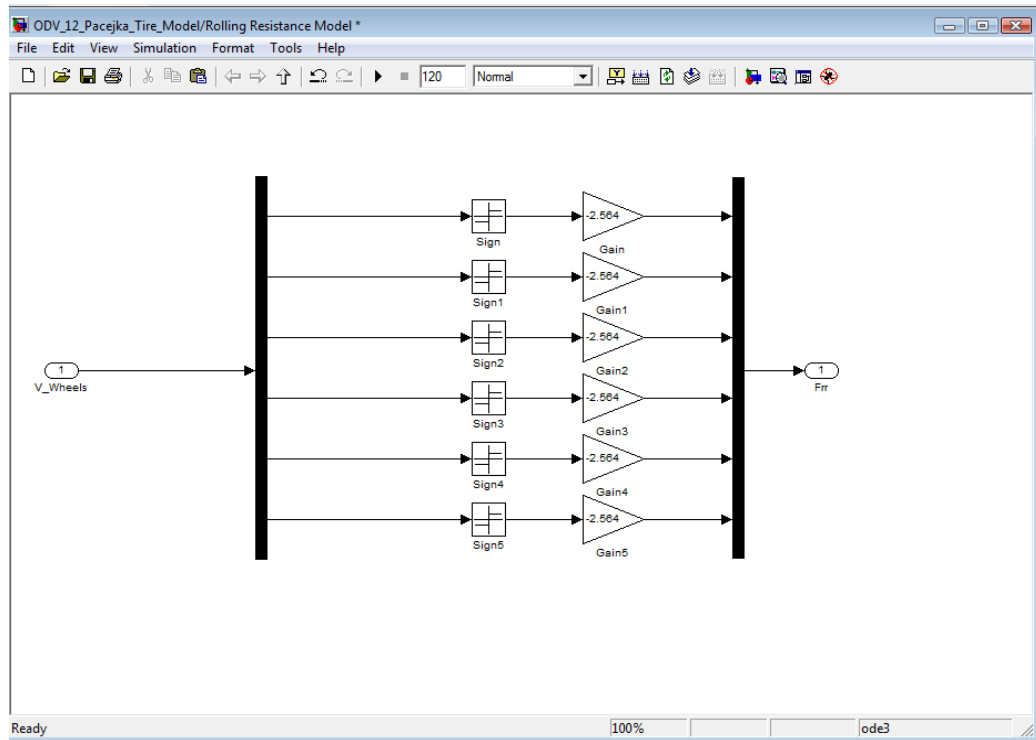


**Figure 5-16 Rolling Resistance Sub-model**

The translational wheel velocity, routed in from the ODV Plant Sub-model, is the independent variable. This velocity is fed into the signum function and is multiplied by the rolling resistance constant which generates the resistive force. This force is then routed back to the higher-level of the simulation. Like the longitudinal tire model and the lateral tire model, the output forces are output to the ODV Plant model.

## 5.8 Air Drag Model

The air resistance model was also determined experimentally from coast-down data. This method was explained in Section 4.2.1 and Section 4.3. The resistance exerted, like rolling resistance, is a function of velocity and opposes the motion of the vehicle. Where air resistance and the tire models differ is the location of the application

of the forces. The tire forces are applied at the location of the individual wheels. The air resistance force is applied at the center of gravity of the chassis. Air resistance also increases as a function of vehicle velocity. This is different from rolling resistance which stays constant as long as the vehicle is moving. The block diagram representation of Equation 4-3 in Section 4.3 is shown in *Figure 5-17*.

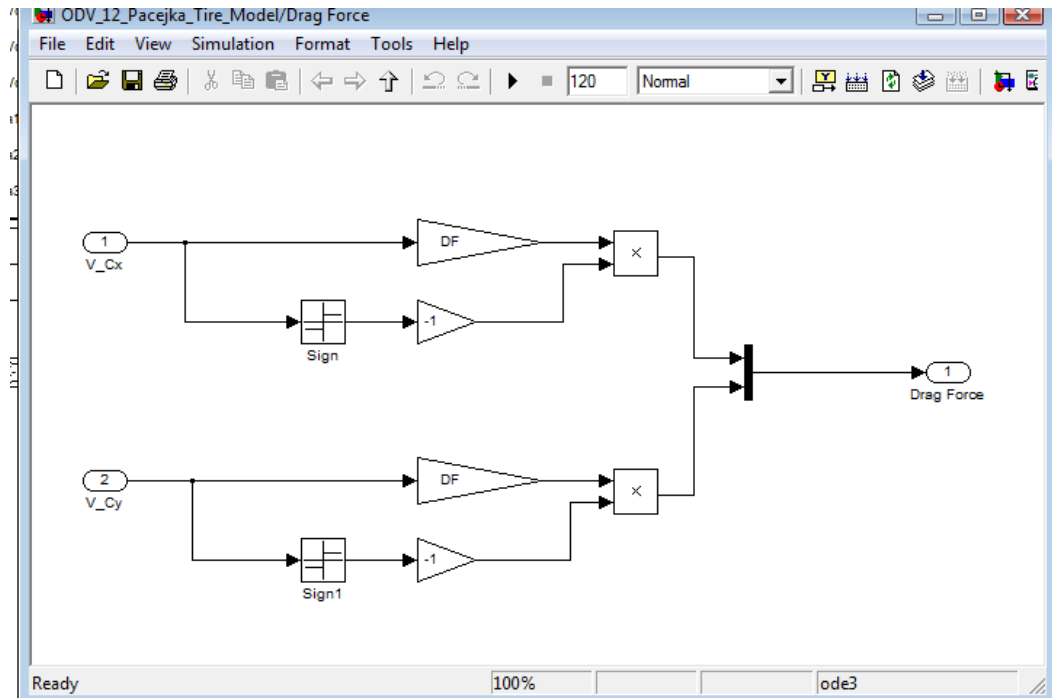


**Figure 5-17 Air Resistance Sub-model**

Since the vehicle is able to move in the x- and y-direction globally, the application of the air resistance force needs to be decomposed into components as shown. This was not necessary for the tire models because the application of the forces were always parallel or perpendicular to the tire. In other words, the tire models are already set-up with their components generated separately.

The velocities of the chassis in the x- and y-direction are the inputs to the sub-model. The velocities are output directly from the ODV Plant Sub-model. In the Air

Resistance Sub-model, the drag force constant found in Section 4.3 is multiplied by the negative of the velocity for both the x- and y-components. The two force signals are fed into a **Mux** block and then routed back to the higher-level of the simulation. These forces are input to the ODV Plant Sub-model where they are applied to the center of gravity of the chassis.

## 5.9 ODV Plant Sub-model

The ODV Plant Sub-model is a combination of the chassis and the three pods attached to the chassis. This sub-model was created employing the SimMechanics extension to Simulink. The SimMechanics extension makes modeling physical devices much easier to create and understand. The ODV Plant Sub-model still utilizes the three tire force signals and the air drag force signals which were generated using the base Simulink blockset. Signals in SimMechanics have physical meaning (and units) as forces, or velocities, etc.; Simulink signals are purely numbers with no associated units. When signals transition between the ODV Plant Sub-model (SimMechanics) and the rest of the simulation (Simulink) a conversion must take place. This conversion is performed within the ODV Plant Sub-model. *Figure 5-18* shows the location of the plant sub-model within the overall simulation.

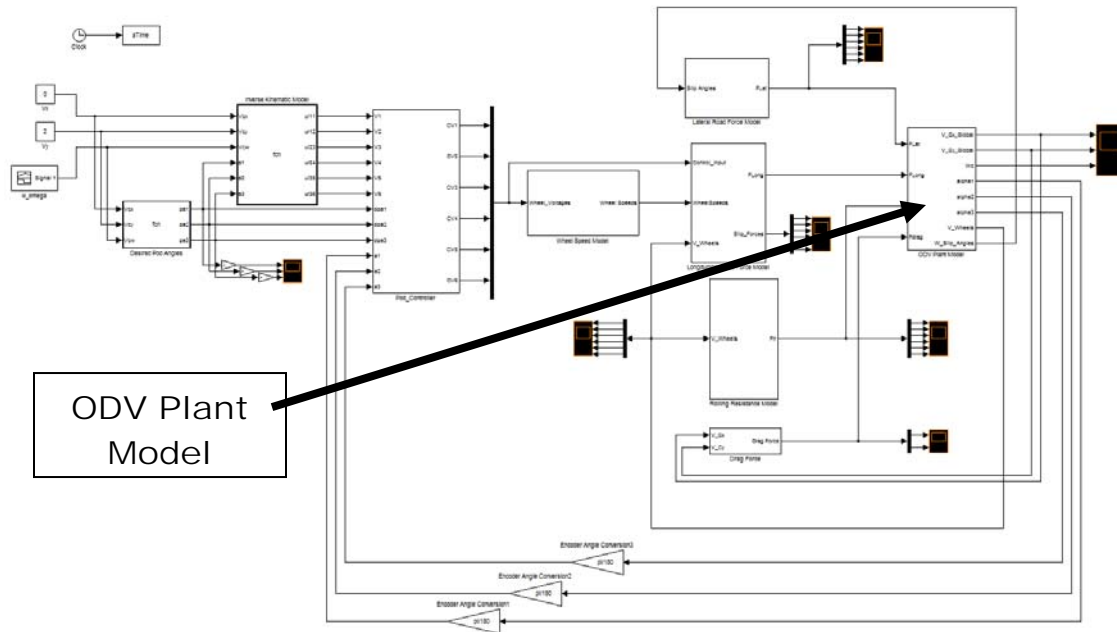


**Figure 5-18 Plant Sub-model Location**

The longitudinal and resistive tire forces are added within the ODV Plant Sub-model before being introduced into each of the pods. These forces come in as a single bundle and are separated by a **Demux** block. Each wheel's respective longitudinal force and resistive force are added to each other after they are separated by the **Demux** block because they are in the same direction.

**Signal Builder** blocks can be added from the Simulink library along with the longitudinal force and rolling resistance force. The one shown was added for modeling different types of disturbances. For example, creating an impulse force at this location will resemble the left wheel of Pod 1 going over a bump. This is used to evaluate how the control system handles outside disturbances. This is highlighted in *Figure 5-19*.

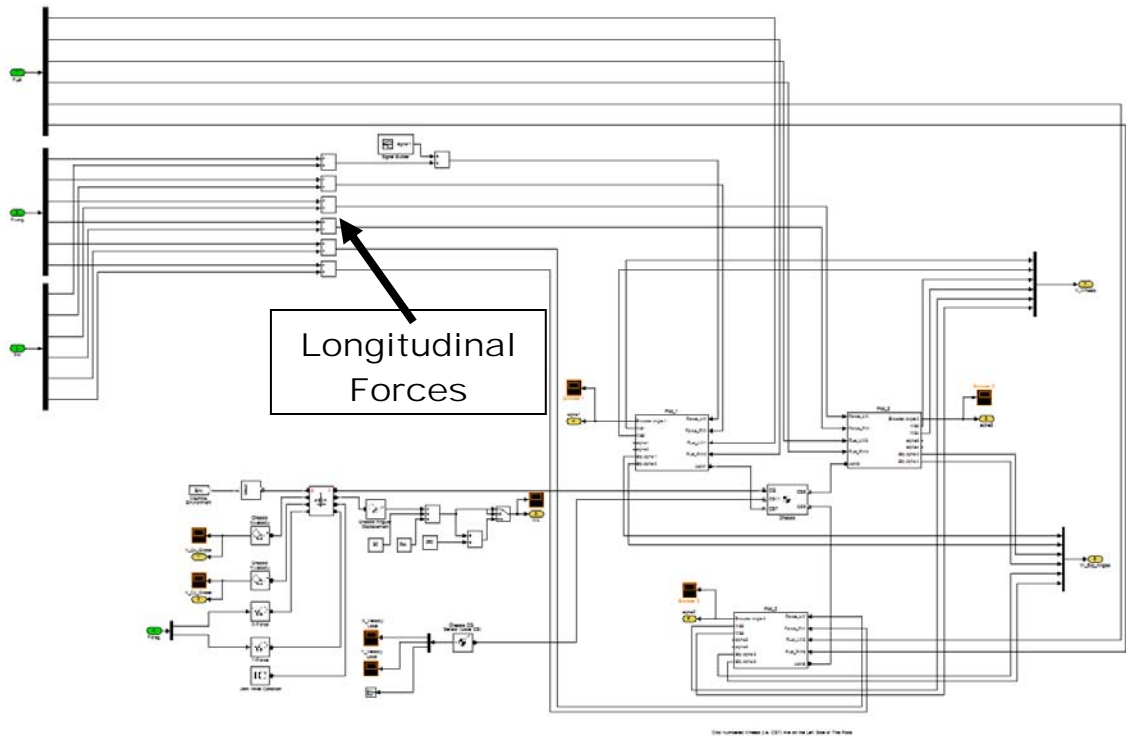


**Figure 5-19 Summation of Longitudinal Forces within the ODV Plant Sub-model**

Just above the longitudinal forces are the lateral forces. These are based purely on the slip angles and are not added to anything else. Once inside the plant model, the group of lateral tire forces is separated by a **Demux** block. Each tire force is then routed to its respective wheel. The location of the lateral force signals and pods are shown in *Figure 5-20*.

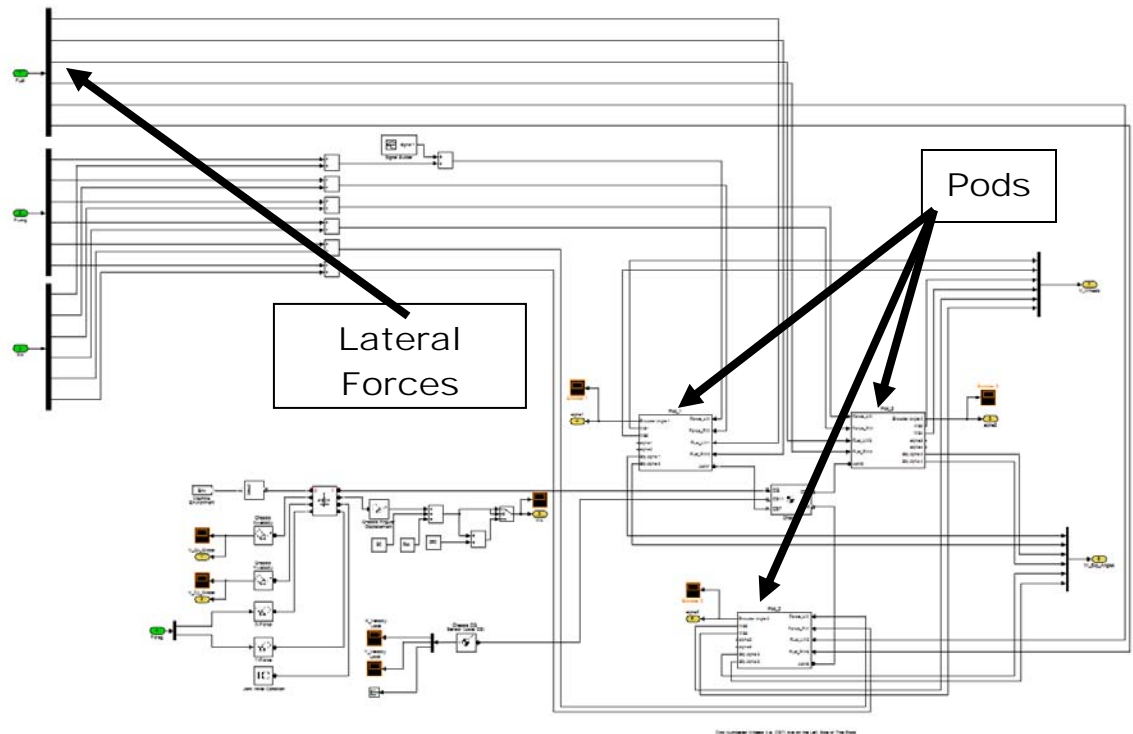


**Figure 5-20 Lateral Tire Force and Pod Location within the Plant Model**

The x- and y-components of the air resistance force are introduced towards the bottom, left side of the ODV Plant sub-model. They are applied directly to the center of gravity of the chassis. To accomplish this, *Joint Actuator* blocks from the SimMechanics blockset allow the components of the air drag force to be applied in their respective directions. A *Planar Joint* is used to allow relative motion between the chassis and the global coordinate system. The chassis and air resistance forces are shown in *Figure 5-21*.

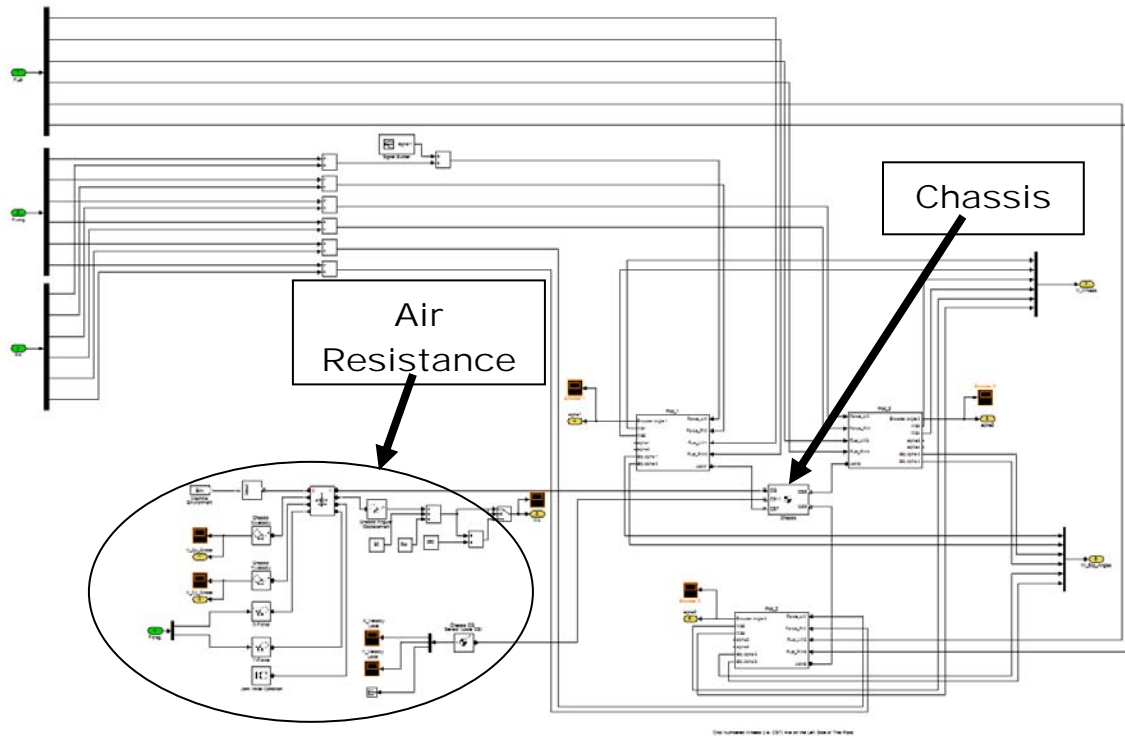


**Figure 5-21 Air Resistance Forces and Chassis Location within the ODV Plant Sub-model**

The chassis itself is modeled employing a **Body** block. Inside the chassis block, the vertex points of each corner of the chassis, attachment points for the pods, and the dynamic characteristics of the vehicle (mass and inertial tensor from Section 2.7) are all specified. Using a **Joint Sensor** block, the chassis angle, in relation to global coordinates can also be measured / monitored. The chassis block is shown in *Figure 5-22*.

**Block Parameters: Chassis**

Body

Represents a user-defined rigid body. Body defined by mass  $m$ , inertia tensor  $I$ , and coordinate origins and axes for center of gravity (CG) and other user-specified Body coordinate systems. This dialog sets Body initial position and orientation, unless Body and/or connected Joints are actuated separately. This dialog also provides optional settings for customized body geometry and color.

Mass properties

Mass: 25.885 kg

Inertia: [0 0 0; 0 0 0; 0 0 18.78512] kg\*m^2

Position Orientation Visualization

Show Port	Port Side	Name	Origin Position Vector [x y z]	Units	Translated from Origin of	Component Axes
<input checked="" type="checkbox"/>	Left	CG	[.3683 -.373939 0]	m	CS10	CS10
<input checked="" type="checkbox"/>	Left	CS11	[.3683 -.373939 0]	m	CS10	CS10
<input type="checkbox"/>	Left	CS1	[0 0 0]	m	CS10	CS10
<input type="checkbox"/>	Left	CS10	[0 0 0]	m	World	World
<input type="checkbox"/>	Right	CS2	[.7366 0 0]	m	CS10	CS10
<input type="checkbox"/>	Right	CS3	[.8763 -.241968 0]	m	CS10	CS10
<input type="checkbox"/>	Right	CS4	[.508 -.879882 0]	m	CS10	CS10
<input type="checkbox"/>	Left	CS5	[.2286 -.879882 0]	m	CS10	CS10
<input type="checkbox"/>	Left	CS6	[-.1397 -.241968 0]	m	CS10	CS10
<input checked="" type="checkbox"/>	Left	CS7	[.089629 -.213059 0]	m	CS10	CS10
<input checked="" type="checkbox"/>	Right	CS8	[.646971 -.213059 0]	m	CS10	CS10

OK Cancel Help Apply

**Figure 5-22 Chassis Information Block**

Once all the data points are entered into this block, SimMechanics can project an image of the chassis in a separate window. Once the simulation is run, the image will look and react like the real chassis, based on the provided vertex points and the dynamic characteristics. At this point, it is important to note that every machine within a SimMechanics simulation must include exactly one **Environment** block. This establishes the gravity vector within the simulation. Under different circumstances, the gravity vector would have been established as  $-9.81 \text{ m/s}^2$  in the z-direction. However, since the simulation does not account for pitch or roll in the vehicle's chassis, the gravity vector was not needed. The longitudinal, lateral, and rolling resistive tire forces have already been handled by Pacejka's tire model and by the sigum function, respectively. Therefore, in this simulation, the tire forces are independent of the gravity vector.

The option to turn on the visualization within the simulation is found under the ***Simulation → Configuration Parameters*** menu. Under the SimMechanics sub-folder, the “Show animation during simulation” box needs to be checked in order to see the vehicle animate during the simulation. Simulink’s graphical representation of the chassis and pods is shown in *Figure 5-23*.

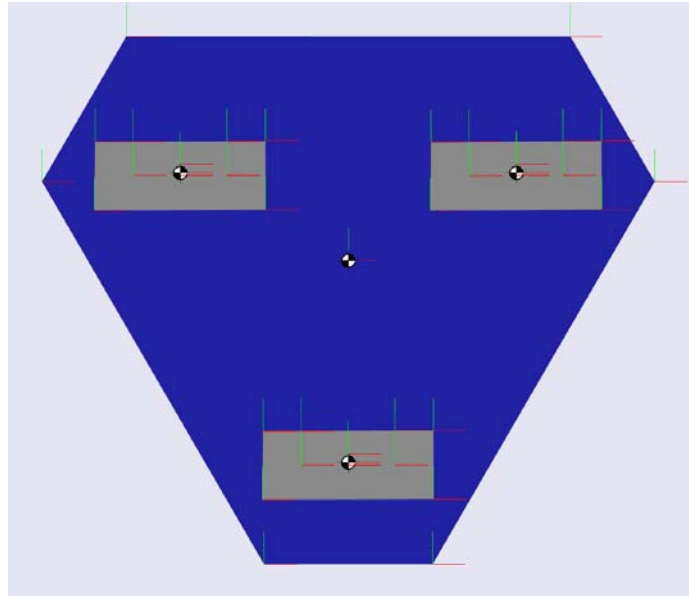


**Figure 5-23 Simulink’s Chassis (blue) and Pod (gray) Graphical Representation**

## 5.10 Pod Models

The chassis has three joints, one for each pod, implemented using ***Revolute Joint*** blocks. These joints connect each pod to the chassis. Just like the real vehicle, the ***Revolute Joint*** limits the motion of the pods relative to the chassis to rotational motion about the vertical z-axis. At this point, the friction of the slip-ring is modeled and shown in *Figure 5-24*. Refer back to Section 4.5 for detailed information on the characterization of the slip-ring friction. Each pod, similar to the chassis, must include a ***Body*** block. In

short, a joint must be connected to either a **Body** or a **Ground** block. The **Body** block for the pod is the same as it is for the chassis with the mass and inertial tensor parameters set specific to the pod. Those parameters were discussed in Section 2.7 and shown in Table 2-4.

In order to allow for application of the tire forces to the vehicle, each Pod Sub-model also has to be connected to the ground via four **Planar Joints**, one for each of the lateral and longitudinal tire forces for each wheel. The lateral and longitudinal forces cannot be applied at the same **Planar Joint** because these two forces are perpendicular to one another. The location of these joints can also be seen in *Figure 5-24*.

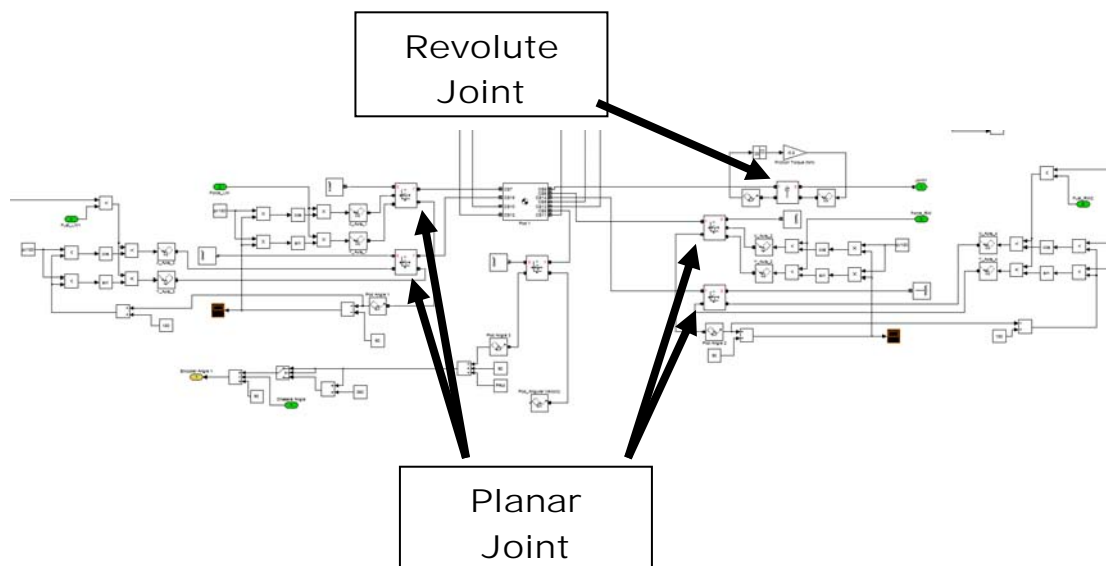


**Figure 5-24 Inside a Pod Sub-model (Planar and Revolute Joints)**

In the Pod sub-models, there are two angle signals employed to track the angle of the pod relative to the chassis. A **Joint Sensor** block is attached to the pod body and measures the angle of the pod relative to the global coordinate frame. The other angle signal is the angle of the chassis, in relation to global coordinates, which was measured in

the ODV Plant Sub-model. Subtracting the chassis angle from the pod angle (globally) gives the pod angle relative to the chassis. This angle is then used to determine the control effort and direction in the closed-loop controller. The global angle of the pod, by itself, is used to ensure that the longitudinal and lateral tire forces are always applied parallel or perpendicular, respectively, to the wheel.

For both the lateral and the longitudinal tire force, the force could be applied in either a positive or negative direction. Longitudinal tire forces that propel the vehicle forward are considered positive, while, lateral tire forces that cause the vehicle to turn to the right (clockwise) are considered positive.

Determining which direction is positive is not as easy as seeing if the vehicle is displaced in the positive x- or y-direction of the global coordinate system. Rather, what is “forward” depends on the orientation of the vehicle. In order to determine polarity for the forces, a series of dot and cross products are used to calculate the velocity and direction, both laterally and longitudinally, of the wheels of the pods. Additionally, the measured velocity and position vectors of the chassis and wheels aid in the calculation of slip ratios and slip angles.

Longitudinally (for calculation of wheel velocity and direction), the velocity vector for each wheel,  $\mathbf{V}$ , is dotted with a vector forward facing and parallel to each wheel, vector  $\mathbf{A}$ . This gives the magnitude of the component of the velocity parallel to the wheel. This will eventually be used to calculate slip ratios and ultimately longitudinal tire forces. The velocity vector,  $\mathbf{V}$ , is a direct measurement (of point  $N$ ) from the ***Joint Sensors*** in the Pod Model. Vector  $\mathbf{A}$ , is a result of subtracting the vector position of point  $N$  (in the global frame) from the vector position of point  $M$  (in the global frame).

Both position vectors were measured from the *Joint Sensors* within the pod. Lastly, vector **B** is found by subtracting the vector position of point *O* from the vector position of point *N*. *Figure 5-25* shows these vectors.

Vector **B** is perpendicular to motion of the pod and faces out toward the left side as shown in *Figure 5-25*. To calculate the correct direction of travel (positive or negative) of the pod, the velocity vector, **V**, is crossed with vector **B**. Multiplying  $(\mathbf{V} \cdot \mathbf{A})$  with the sign  $(+/-)$  of  $(\mathbf{V} \times \mathbf{B})$  yields a wheel velocity that is correct in magnitude and direction. Ensuring the velocity magnitude and direction is correct at this stage ensures that the net longitudinal forces are always applied in the correct direction.

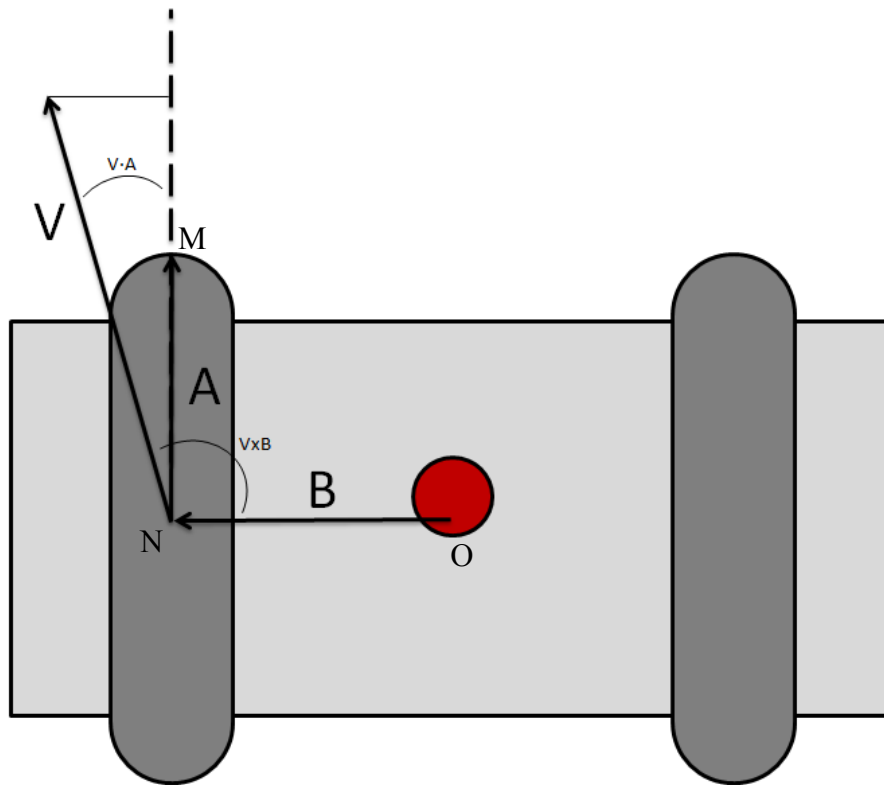


**Figure 5-25 Longitudinal Velocity and Direction Calculation**

Laterally (for calculation of slip angles and the direction of the applied lateral force), the inverse cosine of the vector  $\mathbf{V}$  dotted with the vector  $\mathbf{A}$ , normalized, gives the magnitude of the slip angle for each wheel. Again, slip angle is the measured angle difference between a tire's orientation and direction of travel. The slip angle,  $\lambda$ , is also used to calculate a lateral force. This calculation is shown in *Figure 5-26*.

The slip angle for the right wheel can be found by completing the same steps taken for the left wheel. The direction (positive or negative) of the applied force is calculated by crossing vector  $\mathbf{V}$  with the vector  $\mathbf{A}$  which is also shown in *Figure 5-26*. A positive result from  $(\mathbf{V} \times \mathbf{A})$  means the pod is turning right. The pod is turning left if  $(\mathbf{V} \times \mathbf{A})$  is a negative result. The force calculated from the Lateral Road Force Sub-model (a function of slip angle, Pacejka's tire model) is then multiplied by the direction calculation (from  $\mathbf{V} \times \mathbf{A}$ ) to ensure the force is applied in the correct direction (perpendicular to vector  $\mathbf{A}$ ).

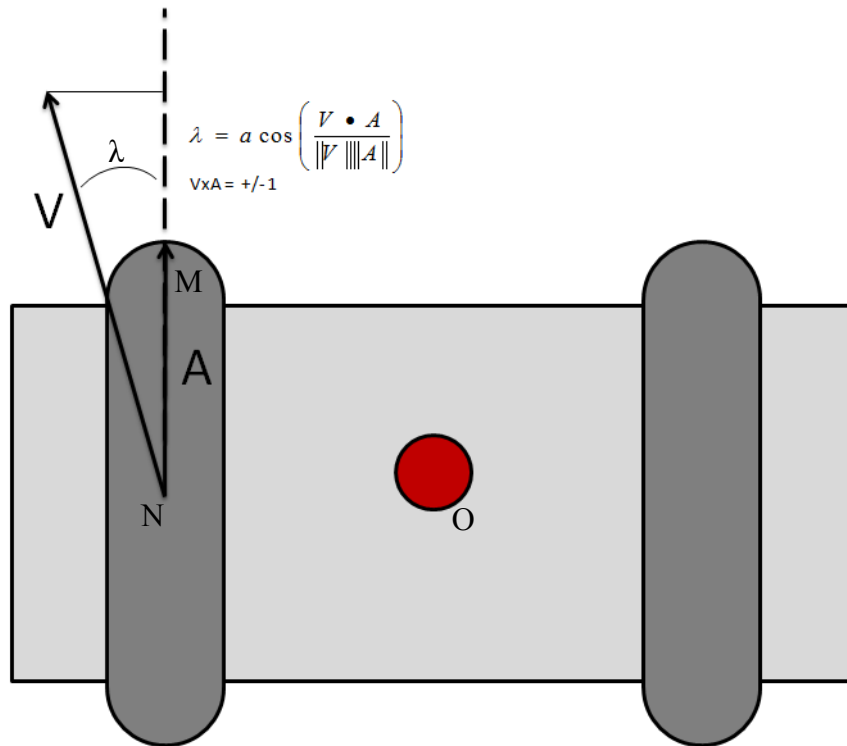


Figure 5-26 Lateral Slip Angle and Direction Calculation

## ***6. Simulation to Actual Vehicle Comparison***

### **6.1 The Comparison of the Actual ODV to the Simulation**

Chapter 6 discusses how the actual vehicle compares to the simulation qualitatively and quantitatively. To be able to compare the actual vehicle to the simulation, the actual vehicle was driven through a series of tests. For each test, the vehicle was given control signals from the driver via the gamepad controller. Those control signals,  $V_x$ ,  $V_y$ , and  $\omega$ , were recorded during the actual vehicle tests. The vehicle's response to those controller signals (resultant chassis heading, pod angles, and/or wheel speeds) was also recorded along with control signals for each vehicle test.

The control signals from each test were then used as the control signal inside of the simulation. Using the control signals, given to the actual vehicle, inside of the simulation allows the direct comparison between the simulation and the actual vehicle. For each test, the measurements recorded during actual vehicle tests were also recorded in the simulation. Once again, this includes chassis heading (angle; global coordinate system), pod angles (in relation to the chassis), and wheel speeds.

Chapter 6 also discusses the tests conducted and proceeds to show how the results from the physical vehicle compared with the results from the simulation. Under the influence of closed-loop control at the pod level, the first test shown is a series of acceleration and deceleration profiles given to the vehicle and to the simulation. This test helps to assess the accuracy of the longitudinal tire model, the vehicle mass estimate, the motor/wheel system transfer function, and the models of the drag-producing elements (air and rolling resistance).

The second test shows how the simulation compares to the actual vehicle system during a turning maneuver under closed-loop control. Specifically, this test demonstrates how the controller on both the actual vehicle and the simulation reacts to a user specified command. This test also shows the accuracy of the lateral tire model employed in the simulation.

The last test illustrates how the simulation vehicle and the actual vehicle compare when being driven through a predetermined test course. This test validates the longitudinal and lateral tire models used in simulation, along with the estimates of many other various physical parameters. This test also demonstrates the performance of the control systems onboard both the simulation and the actual vehicle. Each of these tests and the corresponding results are described in the following sections of this chapter.

## **6.2 Longitudinal Comparison**

As mentioned in Section 6.1, this section discusses the results of the tests subjecting the vehicle and the simulation to varying acceleration and deceleration profiles using signals received from the gamepad controller. For these tests, the pods were locked in a forward facing position (at  $\pi/2$  radians or  $90^\circ$  degrees in relation to the chassis). Furthermore, the  $V_x$  and  $\omega$  commands were disabled allowing only the  $V_y$  command to be given to the vehicle. Allowing only the  $V_y$  command ensures that the vehicle is only allowed to go straight ahead during the course of the test

The longitudinal comparison involves accelerating the vehicle at 20, 40, 60 and 100 percent of top speed. These voltage levels were chosen in an attempt to capture the varying acceleration profiles shown in preliminary testing. In other words, it had already

been discovered that the vehicle shows different acceleration characteristics at low-voltage levels (low speed) than it does at high-voltage levels (high speed). The change between low speed and high speed characteristics is at approximately 2.5 volts of input. This is especially evident when the vehicle reaches its maximum speed for a given voltage. The comparison between the simulation and actual vehicle is shown in *Figures 6-1 and 6-2*. This shows how the vehicle changes acceleration characteristics between high- and low-voltage commands. Note that for *Figures 6-1 and 6-2*, vehicle speed was calculated by multiplying wheel speed by the wheel radius (utilizing the Hall-effect sensors to measure wheel speed for non driven wheels where slip is minimal).

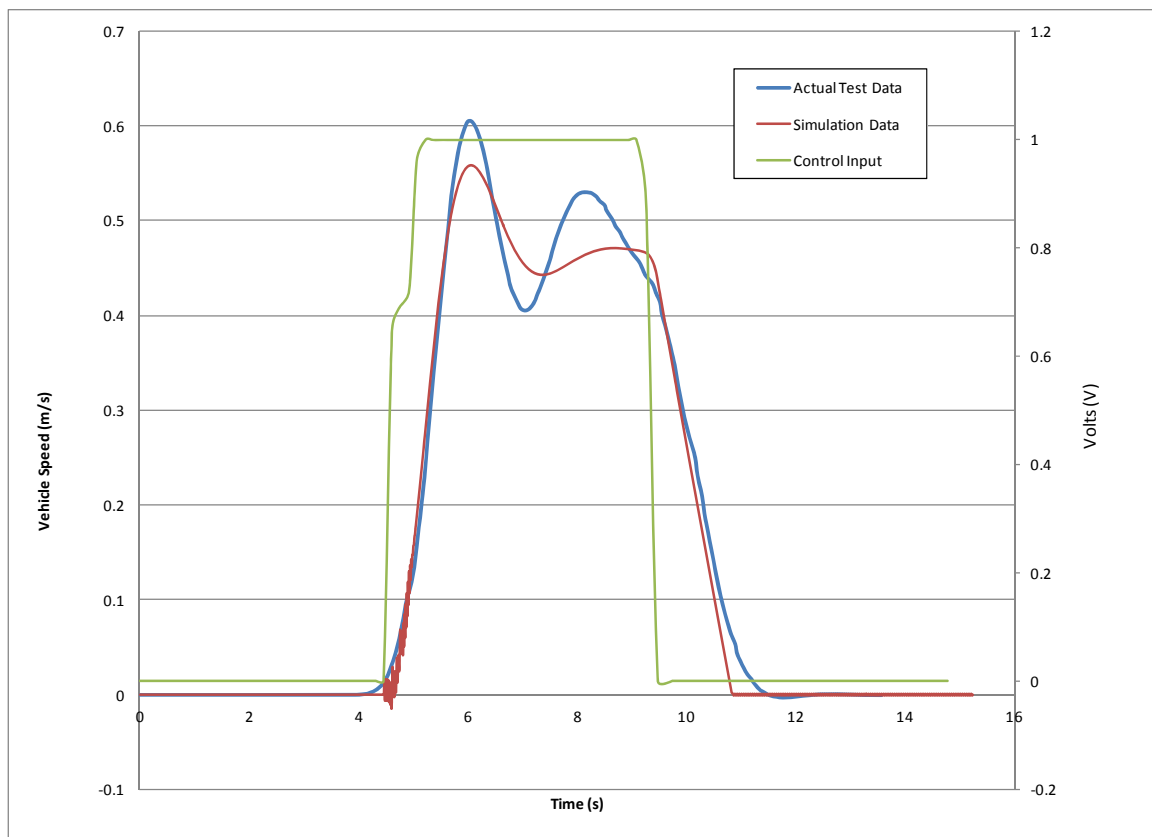


**Figure 6-1 1-Volt Acceleration Profile for the Simulation and Actual Vehicle**

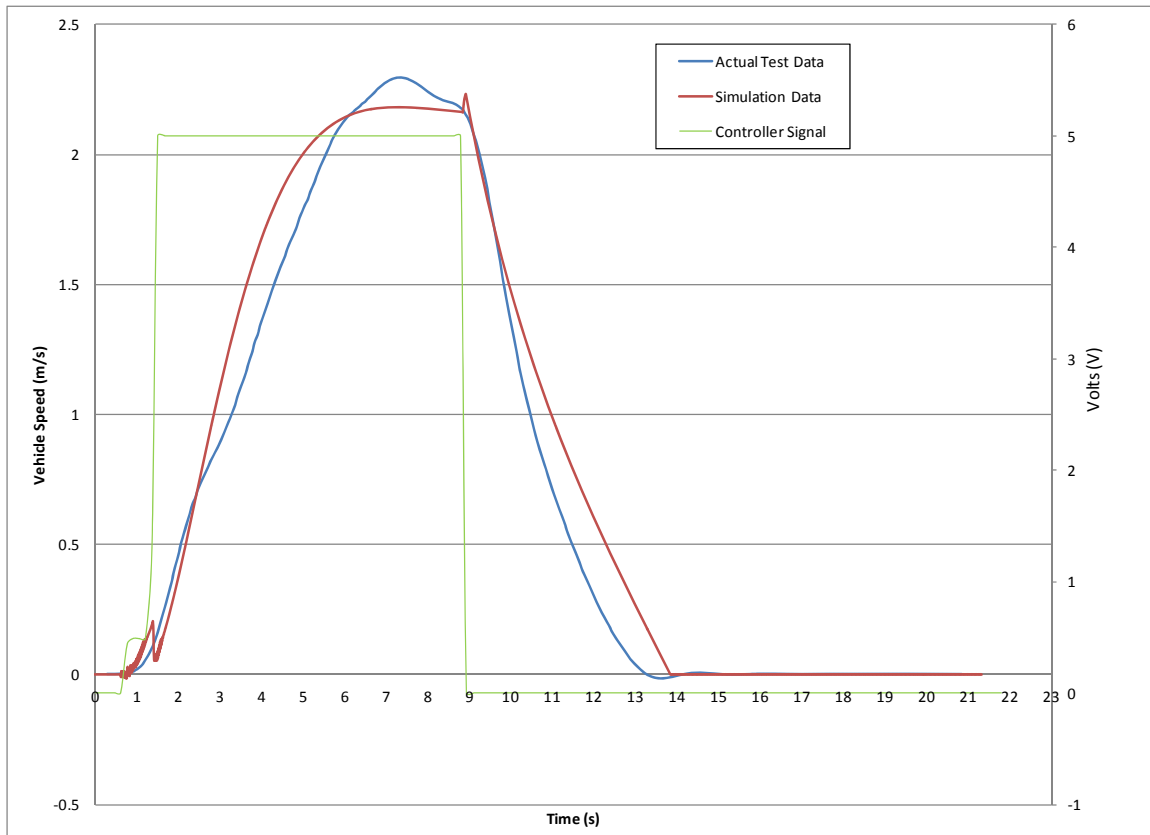


**Figure 6-2 5-Volt Acceleration Profile for the Simulation and Actual Vehicle**

For the test shown in *Figures 6-1* and *6-2*, the vehicle was accelerated until the vehicle hit the commanded speed and then immediately allowed to coast to a stop. The purpose of *Figures 6-1* and *6-2* is to show how the simulation compares to the actual vehicle tests. In particular, this shows how well the longitudinal tire and acceleration characteristics of the vehicles were captured during vehicle testing. *Figures 6-1* and *6-2* clearly show that the vehicle tends to show more of a second-order (oscillatory) acceleration profile at a lower voltage command while the vehicle exhibits more of a first-order acceleration profile at higher voltage commands. These attributes are directly related to the choice of motor controllers. Again, the acceleration characteristics of the vehicle are captured, through the use of a transfer function, which characterizes the wheel

/ motor dynamics. These motor / wheel dynamics interact directly with the weight of the vehicle, air and tire drag, bearing drag, etc., which passively affect how the vehicle accelerates.

The actual vehicle data shown in *Figure 6-1* has 7.7% higher maximum speed when compared to the simulation. *Figure 6-2* shows the actual vehicle having 5% higher maximum speed when compared to the simulation. In the response profiles shown in *Figure 6-1*, the actual vehicle has a 30.1% overshoot while the simulation exhibits an overshoot of 18.9%. Overshoot is not considered a characteristic of the first-order responses shown in *Figure 6-2*. Therefore, overshoot was not analyzed for the simulation or the actual vehicle acceleration profiles shown in *Figure 6-2*.

In *Figure 6-1*, the data in both the real vehicle and the simulation exhibit second-order characteristics with similar frequency and speed of response. For the actual vehicle, the damped natural frequency,  $\omega_d$ , is approximately 3.27 rad/s while the simulation has a damped natural frequency of 2.53 rad/s. The actual vehicle has a damping ratio of approximately 0.132 while the simulation has a damping ratio of approximately 0.170. The damping ratio,  $\zeta$ , along with the natural frequency,  $\omega_n$ , is a major contributor to the length of time a system takes to reach a steady-state speed. The product of the damping ratio with the natural frequency is also known as sigma,  $\sigma$ . The real vehicle has a slightly lower sigma value, when compared to the simulation, which will lead to a higher settling time. Since the real vehicle has a lower damping ratio and a higher damped natural frequency when compared with the simulation, more oscillations with regards to wheel speed can be expected. This is confirmed in *Figure 6-1*.

The data in *Figure 6-2* shows both the simulation and the actual vehicle response having the shape of a first-order profile with similar speed of response. The speed of response of a first-order response is characterized by the time constant,  $\tau$ . The time constant of the actual vehicle is 3.3 sec which is slightly higher than the simulation's time constant of 2.55 sec. This means that, again, the actual vehicle will take a bit longer to reach steady-state than predicted by the simulation.

The quantitative results explained in *Figures 6-1* and *6-2*, will vary depending on the actual level of velocity commanded to the vehicle. The simulation attempts to capture this variation by changing the wheel/motor model characteristics from a second-order system to a first-order system when the motor command falls below a threshold of 2.5 V. However, the actual vehicle characteristics will vary more than the simulation varies throughout the entire voltage input range.

The last item of interest to take away from *Figures 6-1* and *6-2* is how the vehicle decelerates. This portion of the graph shows how well the air and rolling resistance was captured in the vehicle model. *Figures 6-1* and *6-2* shows that the simulation is closer to the actual vehicle particularly after the initial drop in voltage from the gamepad (i.e. as the input steps from 1 volt to 0 volts). The simulation begins to differ from the actual vehicle in the later stages of deceleration especially when near a velocity of 0m/s. When decelerating, the most interesting portion of the deceleration period was around a velocity of 0m/s. Both *Figures 6-1* and *6-2* shows that actual vehicle actually coasts backwards slightly before coming to a stop. This can be recognized by the negative velocity recorded just before the vehicle comes to rest. This was also physically seen during the coast down tests. One possible explanation can be attributed to the stored energy in the

suspension (due to weight transfer during deceleration) which releases due to the rebound and spring forces in the suspension. The simulation, in contrast, simply comes to a rest.

The last type of longitudinal comparison is a series of acceleration and deceleration events representing random periods of full, partial, or no “throttle.” *Figure 6-3* shows one such varying acceleration and deceleration profile with a maximum motor command of 1V and the corresponding simulation and actual vehicle response to that input.

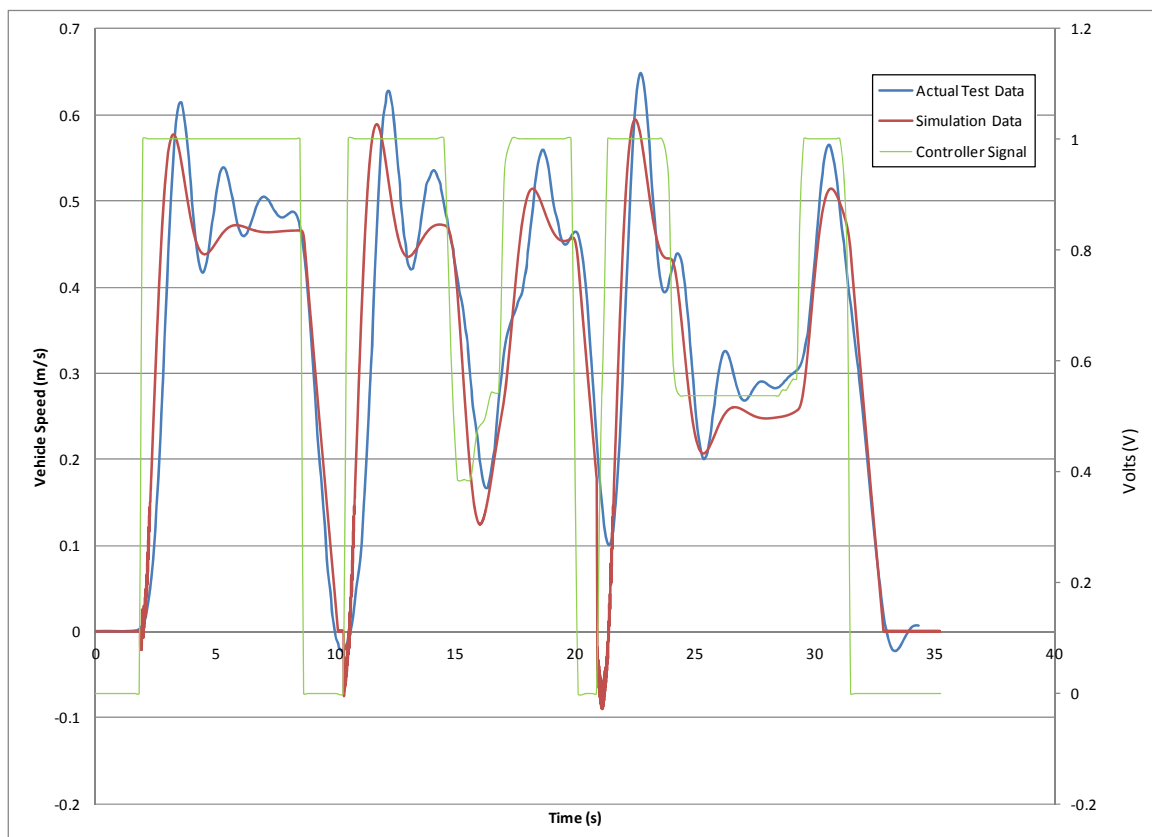


**Figure 6-3 1-Volt Various Acceleration and Deceleration Profile Comparing the Simulation to the Actual Vehicle**

Here again, the simulation has lower overshoot (peak max speed) and reaches steady-state top speed quicker than the simulation. In general, the simulation is damped

more than the actual vehicle. The transfer function responsible for the motor/wheel behavior could have been altered to better fit the actual data shown in *Figures 6-1* through 6-3. The transfer function, however, was chosen to fit a range of voltage levels. That is why the wheel/motor model is separated into two categories (high and low). The response does give slightly different results for variations in voltage command, but the major change seen during vehicle testing is the transition between first-order and second-order type response that occurs between high- and low-voltage motor commands. For example, the vehicle accelerates differently even when various voltage levels show a second-order acceleration characteristic. Comparing *Figures 6-1 and 6-4* illustrates this phenomenon.

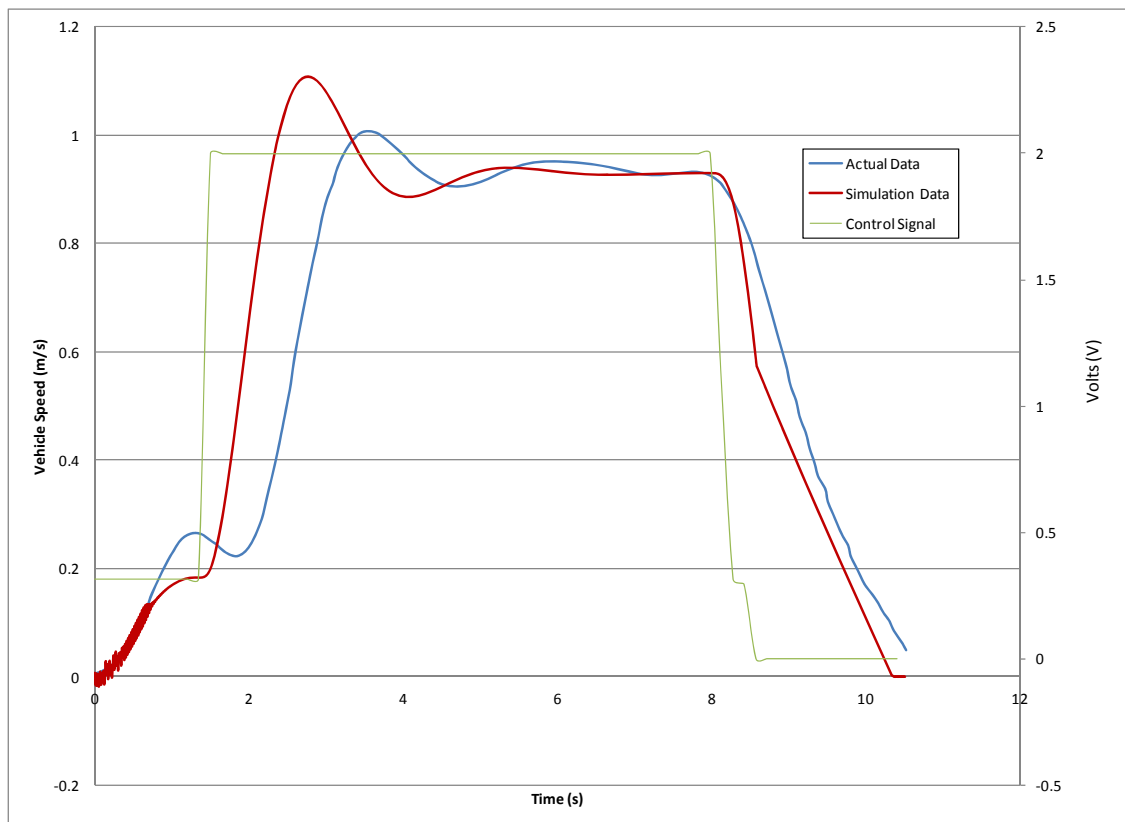


**Figure 6-4 2-Volt Acceleration Profile for the Simulation and Actual Vehicle**

*Figure 6-1* and *6-4* shows how the vehicle can have different acceleration characteristics even though the actual vehicle still exhibits a second-order profile. In *Figure 6-1*, the simulation had less overshoot (peak max speed) than the simulation. *Figure 6-4* shows the simulation having a higher overshoot than the actual vehicle. The simulation still has 18.9% overshoot while the actual vehicle now only has 6.2% overshoot.

On another note, the simulation still reaches steady-state speed quicker than the actual vehicle. For this test, the simulation reaches steady-state maximum speed quicker than the actual vehicle primarily as a result of the shorter rise time. Regardless, the simulation has a damping ratio of 0.170 which is still higher than the real vehicle's damping ratio of 0.057. Even if the simulation had the same rise time as the actual vehicle, the simulation would still reach steady-state before the actual vehicle. The actual vehicle's damped natural frequency did decrease from 3.27 rad/s shown *Figure 6-1* to 2.68 rad/s, but is still higher than the simulation's damped natural frequency of 2.41 rad/s. Therefore, the actual vehicle's speed can be expected to oscillate more when compared to the simulation for the same period of time.

The steady-state speed of the simulation shown in *Figures 6-1* and *6-4* is of particular interest. In *Figure 6-1*, the simulation had a lower steady state-speed in relation to actual vehicle. In *Figure 6-4*, the steady-state speed is now equivalent to the actual vehicle. This simulation characteristic is directly related to making the transfer function usable for a wider range of voltage inputs.

### 6.3 User Defined Turn and Vehicle Controller Comparison

In order to assess the lateral model of the vehicle and its control, the actual vehicle needed to be subjected to a user defined turn. For this test, the vehicle was initially set with the pods facing at  $\pi/2$  radians or  $90^\circ$  (in preparation to move straight ahead) in relation to the chassis. The initial chassis angle (in global coordinates; measured by the Inertial Measuring Unit, IMU) is arbitrary, but was initially set at  $90^\circ$  just for the ease of comparison between the simulation and the actual vehicle.

This test began with the driver commanding 40% of the vehicle's maximum speed (2V) in the  $V_y$  direction which would be straight ahead since the pods were initially aligned at  $90^\circ$  in relation to the chassis. Shortly thereafter (at around 2.2 seconds), the driver commanded a small turn,  $\omega \approx +0.06$  rad/sec while maintaining a  $V_y$  command of 2V. At 6.4 seconds, the commanded  $\omega$  was increased from +0.06 rad/sec to +0.50 rad/s while still commanding a  $V_y$  of 2V. All commands were disabled at approximately 10 seconds into the run. The vehicle and simulation response to the described driving profile is shown in *Figure 6-5*.

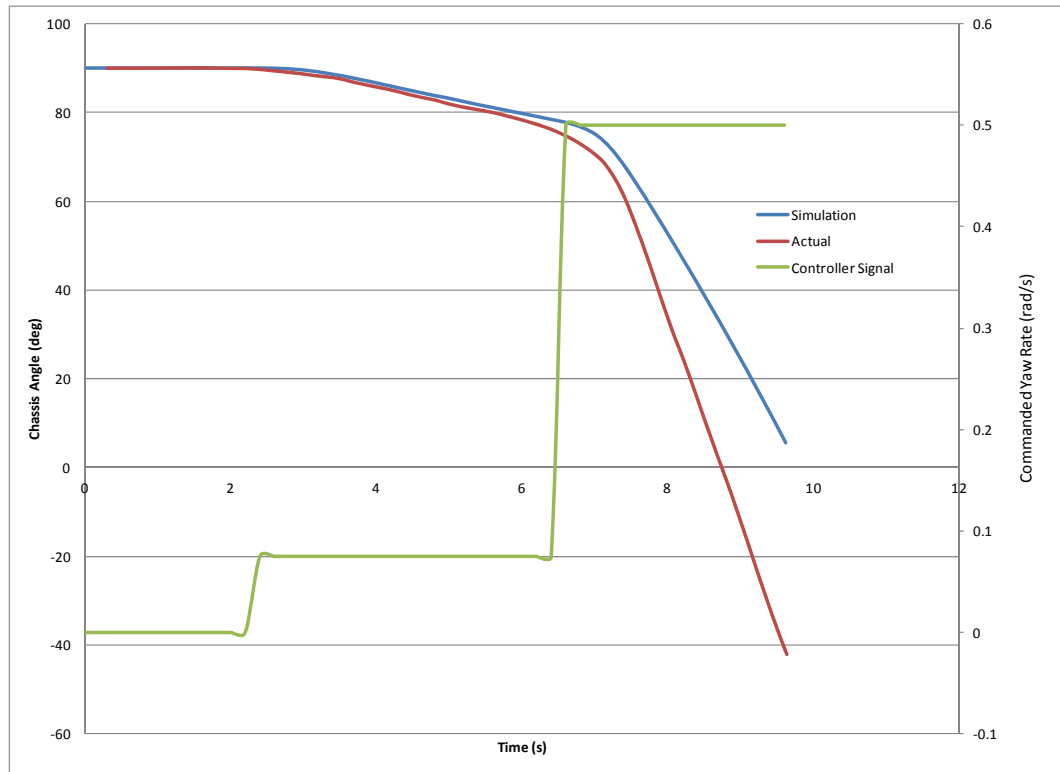


**Figure 6-5 Commanded Turn Profile  $V_y = 2V$ ,  $\omega = +0.06$  to  $+0.50$  rad/s**

Qualitatively, the actual vehicle seems to turn sharper and more gradually than the simulation. During the first portion of the turn, the actual vehicle turned sharper (with a higher absolute yaw rate) than the commanded  $+0.06$  rad/s yaw rate ( $\omega$ ). The actual vehicle turned with a yaw rate of approximately  $+0.066$  rad/s. As expected, the simulation's yaw rate was closer to the commanded yaw rate. The measured yaw rate of the simulation was  $+0.058$  rad/s.

During the later stages of the turn, the commanded yaw rate increased (absolute) from approximately  $+0.06$  rad/s to approximately  $+0.50$  rad/s. At this newly commanded yaw rate, the simulation responded with a yaw rate of  $+0.496$  rad/s. The simulation's measured yaw rate is within 1% of the commanded yaw rate which should be expected. Similar to the first portion of the turn, the actual vehicle also turned more sharply than

commanded during the second portion of the turn. In this portion of the turn, the vehicle turned with a yaw rate of about  $+0.814$  rad/s. This is approximately 63% higher than commanded.

There are three possible explanations for why there is such a high difference in measured yaw rate versus commanded. They include, the slip-ring friction, the motor dynamics, and the controller.

The slip-ring friction contributes in part due to the controller. The slip-rings require that there be a minimum torque present before the stiction in the slip-rings can be overcome and the pods will begin to rotate in relation to the chassis. If the net torque on the pods is under this minimum, then the slip-rings act as if they are locked. Due to this fact, the controller's integral gain will continue to add control effort as long as there is error present in the system (the difference between the actual pod angle and the desired pod angle). Therefore, the controller will continue to increase the control effort until there is enough net torque to break the top and bottom plates of the slip-rings free of each other. At this point, the integral has built up significant control effort which can send the pod past its setpoint (desired pod angle). This will make the vehicle turn sharper than originally desired.

Though the slip-ring friction may be the initial cause of the overshoot, the controller does not help with the situation. As mentioned before, the presence of an integral term will cause a build-up in control effort until the pod angle reaches its setpoint. Unfortunately, the integral term will continue to add to the control effort even as the pod is approaching its setpoint. This leads to an overshoot condition (where the pod rotates past its setpoint). The derivative term and the friction of the slip-rings cause

the pods to stop rotating just past the setpoint. The system will not correct back to the desired setpoint until the controller's integral term builds up enough control effort to, again, break the slip-ring friction. It is true that the controller should eventually correct the yaw rate back to the desired yaw rate. However, the physical constraints of the engineering highbay prevented the test from being run for a long enough duration to see this phenomenon.

Though the integral gain can be decreased to reduce overshoot, this slows the time it takes the vehicle to break free of the slip-ring stiction. This is why there is no particular set of gains that will make the vehicle satisfy both goals.

The last contributor is the motor dynamics. Please note that the  $V_y$  command was 2 volts (40% of maximum speed). As seen from *Figures 6-1, 6-3, and 6-4*, actual vehicle voltages below 2.5 volts result in the vehicle having a second-order acceleration profile. An acceleration profile showing second-order characteristics also means the wheel speeds will overshoot past the commanded wheel speed. All of these items can contribute to the vehicle having a higher (absolute) yaw rate than initially commanded.

Even with the explanations provided, the chassis yaw rate should eventually return to the initially commanded yaw rate. Perhaps the test was not run for the duration of time needed to clearly show this phenomenon. The physical limitations of the engineering highbay did not lend itself for a longer duration test which could have possibly shown the phenomena just described. Another likely explanation is that the loop is not yet closed on the chassis angle which could lead to better control of chassis attitude and yaw rate especially when combined with closed-loop pod control.

## 6.4 Test Course Comparison

Similar to the test setup of Section 6.3, the pods were aligned to  $\pi/2$  radians or  $90^\circ$  in relation to the chassis. To make things easier for comparison purposes between the simulation and the actual vehicle test, the chassis heading was also initially set to  $90^\circ$  in the global coordinate frame. In this test, chassis heading along with  $V_x$ ,  $V_y$ , and  $\omega$  were recorded. This data was used when comparing data recorded from the simulation test run.

*Figure 6-6* shows the course used for both the simulation and the actual vehicle tests. The dotted path is the desired course for the vehicle in both cases. *Figure 6-6* also shows the approximate size and layout of the test course.

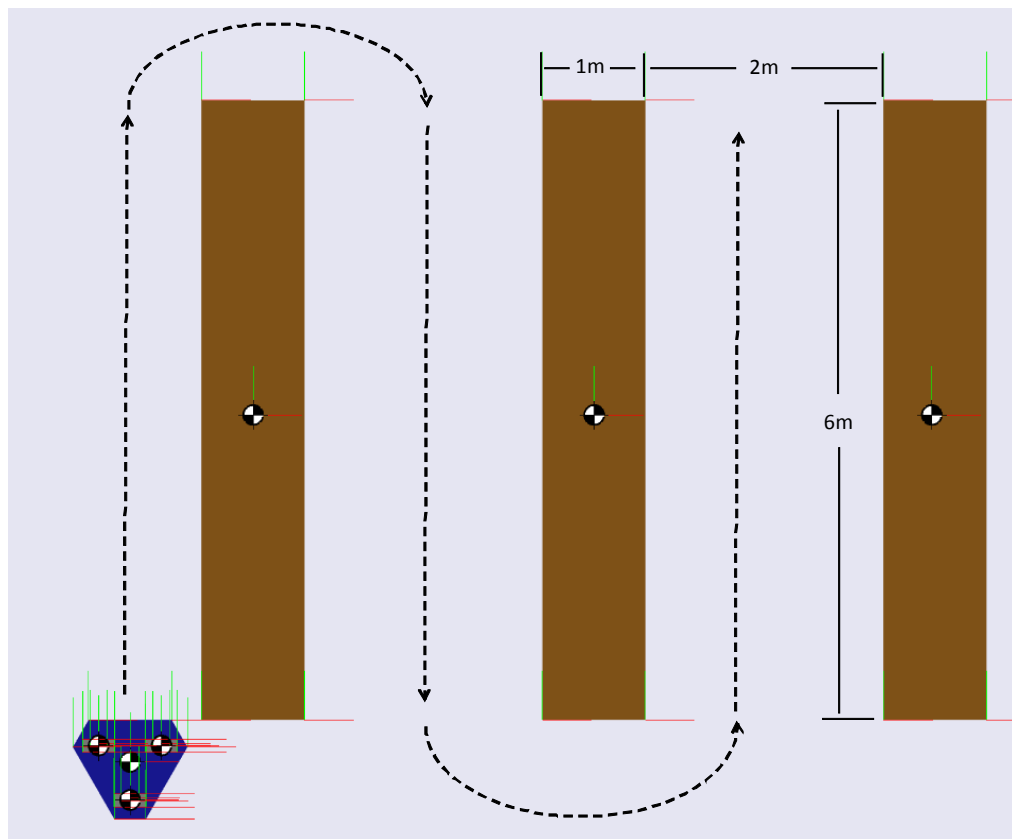


Figure 6-6 Test Course Layout and Desired Path

For comparison purposes, only the control signals were used to compare how (qualitatively) the vehicle drove through the course. In this test, both the real and simulation vehicle run straight first and then turn right (rotating the chassis 180° clockwise). It is desired that the vehicle come fairly close to the “boxes”, shown in *Figure 6-6*, and should not come in contact with them. The vehicle should then re-enter the test course without hitting either of the “boxes.” The vehicle should then proceed downward (with a chassis heading of approximately 270°) where the vehicle is then commanded to turn left. Again, the vehicle should stay in close proximity to the “boxes” without coming in contact with either of the two right-most “boxes.” During this turn, the vehicle should rotate counter-clockwise towards a chassis heading of 90°. The last segment of the course is simply a straight path between the two right-most “boxes.”

The comparison of the simulation to the actual vehicle data makes it very clear that the control algorithms take much longer to run onboard the actual vehicle than they do in simulation. This test also demonstrates the large amount of friction present in the real vehicle’s slip-rings.

This became evident when providing the simulation the same control signals supplied to the actual vehicle. With these signals, the simulation vehicle did *NOT* replicate the path. Therefore, in order to get a fair comparison of the controller and physical parameters, the times at which the vehicle was commanded to turn was adjusted in the simulation accordingly. However, the overall run time for the test, forward velocity, and commanded yaw rate remained consistent between the simulation and the actual vehicle tests.

The forward velocity was commanded to be approximately 1.1m/s (1V in the  $V_y$  direction). At the point of the turn, the vehicle was commanded to turn with a yaw rate of  $\pm 0.45$  rad/s depending on whether the vehicle was turning toward the right or toward the left. The total run time for the vehicle through this test course was approximately 48.8 seconds (recorded when the front of the chassis passed the end of the “boxes”). Again, all of these values remained consistent between both the simulation and the real vehicle test.

In order to get the simulation to run the same path as the real vehicle, the point in time at which the vehicle was commanded to turn had to be later than the actual vehicle. This is due to the lag in computer computation time and the time it took to overcome the slip-ring friction of the real vehicle. For the same reasons, when commanding the vehicle to continue straight through the “boxes,” the command to go straight (a yaw rate of 0 rad/s) was given later than the real vehicle. *Figure 6-7* pictorially displays the difference in time at which the vehicle was commanded to turn. Please note that the actual vehicle’s actions were commanded at an earlier point in time than the simulation.

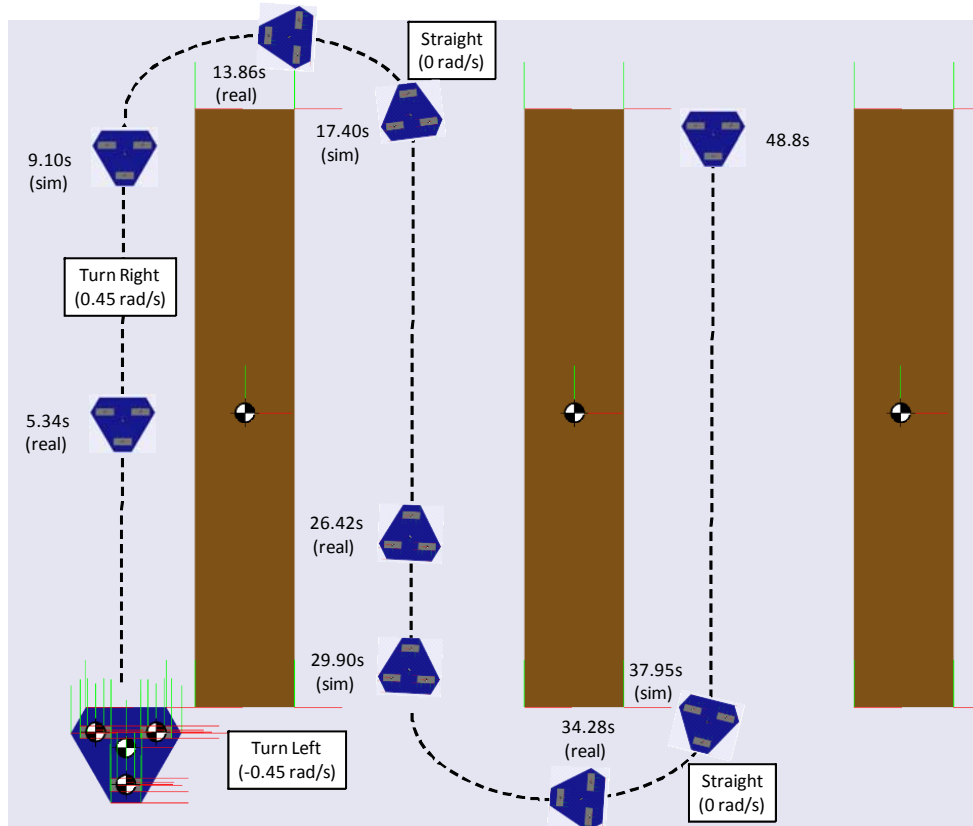


**Figure 6-7 Simulation and Actual Vehicle Turn Command Timing**

To get a closer look at what the two vehicles (actual and simulation) are doing, the yaw rate command timing is tabularized in *Table 6-1*. This table shows, side by side, when the vehicles were commanded to turn or to go straight. The difference between the timing is also calculated.

Action	Actual Vehicle	Simulation Vehicle	Time $\Delta$
Right Turn	5.344s	9.100s	3.756s
Straight 1	13.859s	17.400s	3.541s
Left Turn	26.422s	29.900s	3.478s
Straight 2	34.281s	37.950s	3.669s

**Table 6-1 Command Timing Comparison**

*Table 6-1* shows that on average, the driver needed to react to the course 3.611 seconds before the simulation. Again, this only points out the lag time in the computer

computation and the relatively high friction present in the onboard slip-rings of the actual vehicle.

The 3.611s average lag time is quite large and makes the vehicle difficult to drive. Remedying this deficiency is the number one area that must be addressed in future iterations of the vehicle. Though the lag time is large, it remains reasonably consistent with a standard deviation of 0.125s. Therefore, driving the actual vehicle is possible, even in the presence of such a large delay. Had, the deviation in lag time been much higher than 0.125s, the vehicle undoubtedly would not have been drivable, especially through a course such as the one shown in *Figure 6-6*.

The last piece of information to compare is the chassis heading for the entire run. The chassis heading of the actual vehicle and the simulation vehicle is compared in *Figure 6-8*. Although *Figure 6-8* does not show the vehicle's desired path, the figure can be used to compare the actual and simulation attitude and yaw rates.

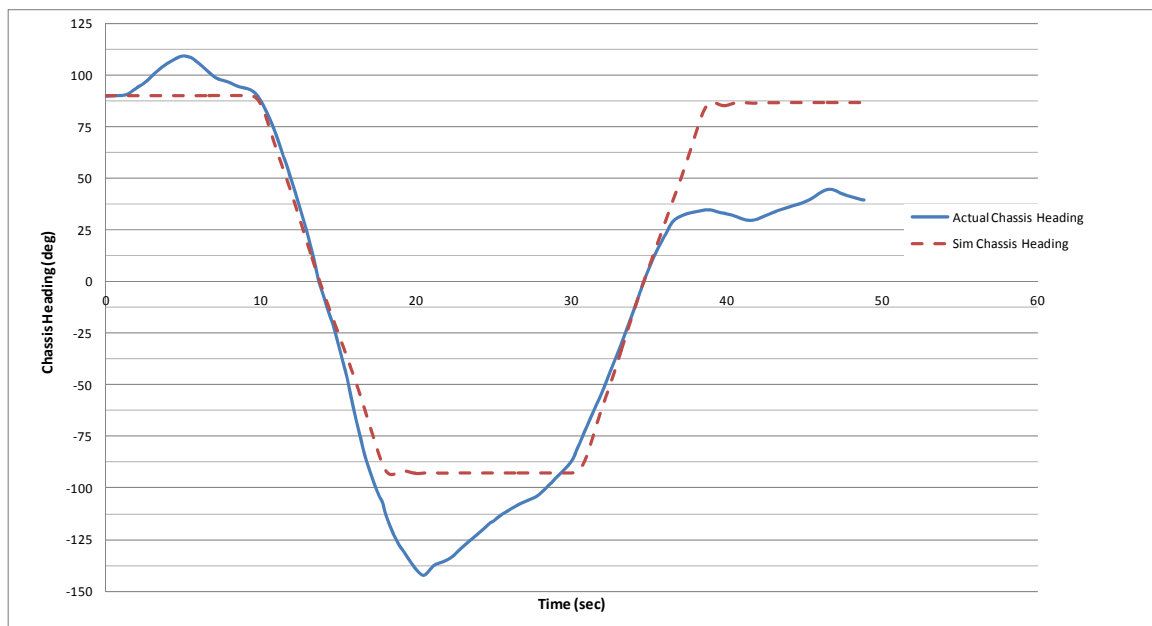


**Figure 6-8 Chassis Heading Comparison**

In *Figure 6-8*, the points in time at which the chassis headings cross zero ( $0^\circ$ ) are when the vehicles hit the center of their turns. These points were adjusted in the simulation to match the real vehicle's inflection points in the turns by adjusting the time at which the vehicle initiated its turn. This is the method in which the lag time of the actual vehicle is calculated (detailed in *Table 6-1*).

The chassis heading of the simulation is depicted in *Figure 6-8* as having a more consistent look when compared to the actual vehicle. This can be attributed to the lack of physical characteristics in the simulation that are present in the actual vehicle. For instance, a misalignment in one of the pods of two degrees ( $2^\circ$ ) can result in a chassis heading difference of 10 degrees between the actual and simulation vehicle during even straight-line motion. This can be seen in the first 24 seconds of the chassis heading comparison shown in *Figure 6-8*.

The second half of the test course included some minor disturbances (height differences in the highbay floor). This could have altered the alignment of the pods and caused uneven loading leading to differences in traction in each of the six wheels. These are things that are not considered in the simulation.

It is true that the simulation did not react in the exact same way as the actual vehicle when given the same commands. However, it is important to note that only the timing of when the simulation vehicle was commanded to turn or to go straight changed. Everything else remained the same including the forward velocity, commanded yaw rate, and PID controller gains. The paths of the two vehicles are remarkably similar and demonstrated the same characteristics throughout the course. Therefore, the simulation is deemed to be adequate for future testing of new vehicle features. The visualization

feature of the SimMechanics expansion of MATLAB will be especially useful for qualitative analysis of future testing.

## ***7. Project Reflection and Future Work***

### **7.1 Summary of Project**

From the start, the goal of this project has been to create a robotic vehicle that exhibits omni-directional characteristics. Furthermore, it was desired that the drivetrain lend itself to be more efficient and more agile than alternative existing designs. As a proof of concept, the design of this vehicle compares favorably to other existing architectures. Six wheels versus a minimum of three, in conjunction with an independent suspension, allows for more available traction at all times. The use of standard pneumatic tires versus mecanum wheels allows for more overall compliance in a variety of situations and terrains. Lastly, the three pod and chassis layout versus the tank drive train achieves true omni-directionality and comes without the scrubbing losses and inefficiencies presented by the dual track systems of a tank.

The scope of this thesis was quite large encompassing the modeling of the vehicle, the development of a control algorithm and software for controlling the vehicle, and the development of a dynamic simulation of the vehicle. Each of these individual areas could have been chosen as the focus of a thesis or capstone project. Instead, it was chosen to invest less depth in each individual area in order to get to the point of a working vehicle and simulation that could serve as a complete proof of concept and could provide a framework for future research. This approach allows for a more thorough and broad understanding of the project without loss of information and understanding during the transfer of each piece of the project.

## **7.2 The Progression of the Project**

The mechanical design and kinematic analysis of the vehicle was primarily complete at the commencement of the work of this thesis. The inspiration for the vehicle came from existing work on the Active Split Offset Castor (ASOC) architecture [11]. The specific characteristics of this vehicle, such as castor offset, wheel split, and the pod joint spacing in relation to the chassis, were chosen based on the needs of the vehicle by Professor Nassif Rayess and the University of Detroit Mercy's senior engineering class of 2007 [1]. The construction of the vehicle's chassis and pods were also completed as part of the aforementioned senior design project. This represents the point at which the work of this thesis commenced.

The remainder of the mechanical assembly was performed in the fall of 2009. This included the installation of the slip-rings onto the pods and, finally, installing the pods onto the chassis. Once mechanical assembly was completed, all electrical work followed suit. This included the installation of the motor controllers, data acquisition devices, batteries, and the routing of the wiring connecting the electrical components. The completion of the electrical wiring concluded the physical construction of the vehicle.

Aside from the physical portion, work was done simultaneously to complete a first instantiation of the control software (LabVIEW VIs) which serves as the interface between the human driver and the vehicle hardware. Specifically, the software was implemented to perform the underlying calculations (inverse kinematics) necessary for converting driver inputs into motor commands. This eventually came to serve as the feedforward portion of the overall pod controller.

Special consideration was taken to make sure the driver could safely and confidently control the vehicle. The solution was a gamepad (handheld remote control) from a modern day gaming console. Such a device provides excellent wireless signal, allows for customizability of numerous control inputs, and provides an intuitive interface for this generation of would-be drivers. Most importantly, LabVIEW also recognized and allowed the use of the Windows-based gamepad with minimal specialized setup required.

In order to make the vehicle usable at speeds above 1m/s, a closed-loop controller had to be developed. This is where the development of the simulation became necessary. Creating a simulation that qualitatively portrays how the physical vehicle acts was necessary for the proper development of the PID control system currently in place on the actual vehicle. This required conducting a series of tests to capture the physical characteristics of the vehicle's various components. This included a tire model, a black-box motor/wheel model, wind- and tire-drag models, and slip-ring models. Testing was, of course, also performed in order to develop the controller (including both a feedback and feedforward portion).

A working simulation allowed for the tuning of the control system. This proved to be an effective method in the development of the vehicle control system as the structure developed in simulation is currently employed on the actual vehicle. Tuning techniques used on the simulation were directly carried over to real vehicle as the simulation proved able to approximately predict the behavior of the actual vehicle. A simulation was also an effective tool when developing future iterations of the project. It will allow physical changes to the virtual vehicle where the behavior of such changes can

be quickly implemented and studied. Furthermore, all of this could be done while having zero concern for the wear and tear on the actual vehicle. This will reduce costs and speed up development time for future builds.

## **7.3 Reflection and Future Builds**

The reflection and future work in regards to this vehicle can be separated into a few categories the majority of which pertain to the physical components of the vehicle. The remaining few are attributed to the control of the vehicle. These reflections and suggestions are mentioned in the following few subsections.

### **7.3.1 Build Quality, Manufacturing, and Materials**

It quickly became evident that there existed some quality issues with the construction of the wheel assemblies. The connection interface between the motor/transmission output shaft and the axle was drilled off center for all six wheel axles. This forced the use of non-rigid mounting structures in each of the motor mounts. This may have also attributed to the premature wear consistently observed on all of the motors. To remedy this situation, concentricity requirements should be placed on the inner hole diameter (motor output shaft interface) and the outer diameter of the axle.

The chassis itself seemed to be a very heavy component of the vehicle which also negatively impacted the chassis's rotational inertia. Though the material has a great impact on the weight of the chassis, special consideration on the chassis's geometry and tubing layout is suggested. It is commonly understood that cost is an important driver in the choice of materials. However, the use of aluminum tubing is still suggested.

If the strength of the chassis is among the top priorities of the build, along with cost, then this again circles back to reconsidering the chassis geometry and layout. It was noticed that the chassis consistently used box tube throughout the build. The use of box tube will make mounting additional hardware to chassis easier, but will increase weight when compared to a similar strength round tube. Instead of using box tube throughout the entire chassis, round tube can be used for the vertical portions of the chassis. The level of skill required for welding vertical circular tubes to horizontal box tubes will be approximately equivalent. This will also reduce weight while maintaining strength.

Additionally, the wall thickness of tubes used in non load bearing locations can be reduced. There also appears to be several tubes that do not contribute to the overall strength or ease of assembly to the overall vehicle. In short, more time needs to be spent on FEA and minimizing the amount of material used in the vehicle.

Future builds could also be used to investigate and confirm the effects of changes in caster angle, wheel offset, and control / drive strategy (one pod leading versus two). These changes should first be tested, optimized, and confirmed in simulation prior to testing with the real vehicle (see section 7.3.6). This will provide an understanding of predicted vehicle behavior while preventing additional and un-needed cost and time from being spent on the real vehicle.

### **7.3.2 Motors, Gearboxes, and Batteries**

In conjunction with the weight of the vehicle, the motors used on the vehicle seem to be underrated for this particular application. They simply do not provide the necessary power to prevent them from constantly being overworked. These motors do last if care is taken to not drive the vehicle at high speeds for extended periods of time, but

countermeasures need to be taken in order to prevent the motors from being permanently damaged. In future builds, if similarly rated motors are used, an internal shutoff protecting against overheating should be standard. Internal or external cooling fans are also highly suggested.

In replacement of the current motors, RC car motors (those professionally built for racing applications) provide better performance and come paired with speed controllers (offering customizability to throttle response) at a fraction of the cost of the motors and controllers used on this project. The motor controllers also allow for the existence of a braking profile without using additional wiring channels on the slip-rings. The motors also have several options for external heat sinks and cooling fans. Additionally, the lithium ion battery packs currently used in professionally built RC cars offer great performance, long battery life, fast recharge, better packaging, and maintain cost competitiveness with the current batteries used in this project. Of course given other space constraints, there are other options available for a choice of motor, controllers, and batteries. This is just one combination that has a known reliability, offers off-the-shelf availability, maintains or exceeds performance and cost competitiveness with the current components.

The gear boxes also caused several problems during the mechanical assembly. It was discovered that one of the internal gears was made of plastic. This gear eventually prematurely wore out in all six of the gear boxes used in the project. Future use of this gear box should include metal gears for increased durability. However, the problems seen in these gear boxes may have been compounded by the heavy chassis/vehicle. Future gear boxes should also include output shafts that are keyed to the axle rather than

using set screws. This will make the connection more rigid thereby reducing losses in the drivetrain.

The gearboxes, along with motors, were determined to be underrated for their application. Another suggestion is the use of a planetary gearbox which allows for a higher application of load versus a standard gear box. Given the appropriate package constraints, this type of gearbox, when coupled with a higher rated motor, should provide ample performance for the vehicle.

### **7.3.3 Suspension**

Though the layout of the suspension seems to be very adequate for the vehicle, more time needs to be spent tuning the suspension for better overall control of the vehicle. The vertical bearings (which allow the independent motion of each wheel) need to allow only the vertical motion of the wheel. During several tests, rotational movement of the wheels around the z-axis of the pod was noticed. This will reduce the effectiveness of the control system and allow for non-consistent compliance with road disturbances. Essentially the vertical bearings need to have tighter tolerances and be constructed of materials other than plastic. Aluminum may be a better choice in this situation.

The last note regarding suspension tuning is related to the damping characteristics and spring constant. Though the damping in compression seems to be particularly well suited for the application, there is too much damping in rebound, essentially not allowing the vehicle to return to a level condition after a bump or after the vehicle has shifted weight during acceleration, turn, or coast-down maneuvers. This problem could also be addressed by employing stiffer springs.

### **7.3.4 Slip-rings**

There is no doubt that the slip-rings were a necessary portion of the mechanical assembly. Without them, the vehicle simply cannot operate and be omni-directional at the same time. The slip-rings are needed so that electrical connectivity can be maintained through a full 360°-rotation of a pod (without tangling the wires).

However, the use of these devices cause some problems in the simulation and control of the vehicle. In particular, it is very difficult to model the stiction of the slip-rings in simulation. Several attempts to model the stiction phenomenon are still ongoing. A true stiction model was abandoned and replaced with a viscous and coulomb friction element in an attempt to reduce simulation run times. The viscous constant is set as high as possible to more closely resemble the stiction phenomenon. In the real world, stiction represents additional and un-needed frictional forces that only cause more work for the already underrated motors. Stiction also introduces instability in both the real and simulation control systems since stiction is difficult to predict and is inconsistent.

Future builds should utilize materials that, if possible, maintain electrical connection but with reduced static and kinetic friction. If the budget allows, wireless communication between the motors and controllers and the vehicle computer would be the best avenue, thereby eliminating the need for slip-rings altogether.

### **7.3.5 Tires and Wheels**

The wheels were constructed of some form of polymer thereby reducing weight. No complaints were offered from the strength of the wheel, but the shape of the air valve does provide difficulty in airing up the tires to their specified pressures. Unfortunately, the pod needs to be disassembled in order to air up the tires. This can be fixed either by

changing the structure of the pod or by altering the routing of the air valve. Since air valves are fairly standard, the recommended fix is the redesign of the pod's "U-shape". Changes in the "U-shape" are also believed to positively impact pod and, therefore, overall vehicle weight. Decreased inertias will also speed up the response from the controller.

The tires provide ample grip for this application. Not once was the vehicle observed to have lost longitudinal or lateral traction with the surface on which it was rolling. However, the tire characteristics found during testing lead to the conclusion that the tire generates the most grip at 100% longitudinal slip and/or at a 90° slip angle. Although this provides stability for the vehicle, this is greatly different from typical tires which typically yield the most grip at 10% longitudinal slip and/or at a slip angle of approximately 5° [14] [22]. Though this does not cause an immediate issue, typical tire models within the simulation do not work as accurately with this tire. Lastly, constantly operating the vehicle at high slip angles and slip ratios will cause premature tire wear and may lead to premature wear on suspension components and connection points to the chassis.

#### **7.3.6 Simulation and Software**

With all of the suggested changes to the physical hardware, changes in the simulation and software are also needed. Physical changes will alter the characteristics of the components and the overall vehicle. For instance, changing tires will lead to differences in how the vehicle accelerates, corners, and potentially coasts and brakes. Changes in the motors will alter how the overall vehicle accelerates and brakes. Chassis construction changes will lead to a change in aerodynamic forces and will change how

the vehicle accelerates and decelerates. Going to a wireless communication set-up in place of slip-rings will eliminate the slip-ring friction altogether which will change how the pods rotate.

For increased vehicle safety, and possibly its surroundings, more heuristic control strategies should also be developed. In the event that one or more pods become out of sync or under other extreme operating conditions, the stability of the vehicle must be maintained. The vehicle needs to have the ability to shut itself down if the vehicle is directly or indirectly being operated in an unsafe manner.

The first step in revalidating the simulation is to retest every aspect of the vehicle once more. This means more acceleration and deceleration tests to revalidate tire rolling resistance and aerodynamic forces. A black-box model could also be used to fit the new motor characteristics at this point, but an in-depth study on the motor characteristics is recommended. For example, the wheel and motor with off-the-shelf controller were modeled as a single unit for an input of voltage and an output of angular speed under driving conditions for a single road surface. A higher fidelity model would capture the wheel/motor characteristics separate from the controller and would model how the system responds not only to a voltage input (affecting motor torque), but also specifically to the road force input at the wheel. This will make the acceleration and deceleration characteristics much more accurate over a range of voltage inputs and road conditions.

A new tire model should include drum testing while the tire is being operated at speed rather than at speeds at which the vehicle will not be operated. This also means accounting for changes in tire pressure, surface temperature, load, and suspension

compliance (toe and camber effects). Perhaps the largest impact is the surface on which the tire is run, so several tests validating numerous surfaces is recommended.

Future iterations of the simulation should also model the effects of the suspension and finally introduce the third dimension. This will allow an in-depth analysis of suspension characteristics in response to vehicle loading and will thus allow the tuning of the damping and spring constants. Furthermore, the third dimension (in addition to a suspension model) will allow for the consideration of weight transfer which will in turn independently affect the available traction of all tires.

In light of all the physical changes, the last item to be tuned is the control system. Additional time must be spent recalibrating the control system to match the interaction and behavior of the new physical components. This should be done on the simulation first to get an idea of how the system will react to changes. The new PID gains can then be changed on the real vehicle to match those of the simulation. Additional fine tuning of the gains on the real vehicle may be necessary at this time. The current build also only includes one set of PID gains which will be adequate when operating the vehicle under 2 Volts (40% of top speed). Future work on the pod control system should include a gain schedule which alters the weight of the PID gains in relation to the feedforward portion to the controller. In short, the higher the voltage level, the higher the gains should be and vice versa.

Once a pod-level control system has been re-established, future work can include closing the loop at the chassis level. This will include the use of the IMU which measures chassis heading. By providing a feedback loop on the chassis angle, an additional layer of control can be offered to the driver especially since the driver is

ultimately primarily interested in chassis heading. The driver is also interested in controlling vehicle speed, but this can be effectively controlled by the driver without assistance from the vehicle control system. The current pod-control system, although adequate for the current build, only indirectly controls the chassis heading. The closed-loop control at the chassis level will allow active control over the chassis angle and will correct for errors in the kinematic models currently employed for relating pod angle to chassis heading. Use of the IMU will also allow for control of heading in the global reference frame, rather than the body-fixed frame attached to the vehicle. Please note, however, that the active control of the pod should still be maintained since it is hypothesized that the pod-level of control provides for faster response due to the smaller inertias of the pods and their relative proximity to the ultimate input for the controlling vehicle motion, the forces at the road/tire interface.

The last change on the software side should positively impact the computing speed of the laptop. Currently, loop iterations (time between each set of calculations [inputs to outputs]) take approximately 0.20 seconds to complete. This, simply, is too much time between calculations. This causes delays in a control system that needs to be operating as quickly as possible. The main reason for the reduction in loop iteration time is that most outside disturbances to the pods, wheels, and chassis, will be acting on a much quicker time scale than 0.20 seconds. Secondly, average human reaction time borders on 0.20 seconds. Therefore, in order to make the control system able to respond to disturbances quicker than a human would, the loop time needs to be reduced. Up-to-date computers, up-to-date software, and more efficient LabVIEW VIs are highly recommended. Additionally, it is thought that LabVIEW has the capability of compiling

a program as an executable to run outside of the Windows operating system, thereby increasing the speed of operation.

## **7.4 Conclusion**

In conclusion, this project serves as a proof of concept and should inspire future build iterations. The time invested in this project will greatly reduce time spent on future builds. This is a direct result of the high level of understanding taken away from this project and the simulation tools that have been developed.

Of all of the suggested changes offered, build quality and reduction of weight in conjunction with a lower loop iteration time will vastly improve the performance of the vehicle. From there, closing the loop on the chassis level will allow active control over the vehicle, thus allowing true omni-directionality capability. This vehicle should have no issues handling rough terrain given that the control system operates much quicker and given that the overheating issues with the motors are taken care of in future builds.

In short, numerous problems and challenges arose during this particular build, but it is considered to be very useful information. This knowledge quickly pointed out the strengths and weaknesses of the vehicle while also offering potential changes and improvements. The most difficult challenge is perhaps cost, but careful consideration of materials, overall size, and layout can keep costs low while maintaining strength and durability. Future builders/students must also be unafraid to think outside the box and try out ideas that go against the common practice.

## References

- [1] Rayess, Nassif. *Omni-directional Vehicle TARDEC Grant Report*. University of Detroit Mercy, Detroit, USA, January 2009.
- [2] ThanZaw, Maung, Denny Oetomo, Marcelo H. Ang, and Ng Teck Khim. *Kinematics and Dynamics of an Omnidirectional Mobile Platform with Powered Castor Wheels*. Technical Report. National University of Singapore. Sept. 2003.
- [3] Wada, Masayoshi, and Shunji Mori. "Holonomic and Omnidirectional Vehicle with Conventional Tires." *International Conference on Robotics and Automation* (1996): pp. 3671-3676.
- [4] Braunl, Thomas. "Omni-Directional Vehicles." *Robotics UWA*. Web. 14 July 2011. <<http://robotics.ee.uwa.edu.au/eyebot/doc/robots/omni.html>>.
- [5] Johns, W. E. "Notes on Tracked Vehicle Steering." *The Gizmologist's Lair*. 2003. Web. 14 July 2011. <<http://www.gizmology.net/tracked.htm>>.
- [6] *My 1/6th Scale M-1A2 Abrams Tank* |. 2008. Web. 14 July 2011. <<http://shootermike.webs.com/tracks.htm>>.
- [7] Diegel, Olaf, Aparna Badve, Glen Bright, Johan Potgeiter, and Sylvester Tlale. "Http://ftp.mi.fu-berlin.de/Rojas/omniwheel/Diegel-Badve-Bright-Potgieter-Tlale.pdf." *Australasian Conference on Robotics and Automation* (2002): pp. 117-121.
- [8] "Mecanum Wheel MK2 by Zaggo - Thingiverse." *Thingiverse - Digital Designs for Physical Objects*. MarkerBot Industries. Web. 14 July 2011. <<http://www.thingiverse.com/thing:2473>>.

- [9] Tlale, Nkgatho S. *On Distributed Mechatronics Controller for Omni-directional Autonomous Guided Vehicles*. Technical Report. University of Pretoria, 2007.
- [10] Doroftei, Ioan, Victor Grosu and Veaceslav Spinu (2007). *Omnidirectional Mobile Robot - Design and Implementation, Bioinspiration and Robotics Walking and Climbing Robots*, Maki K. Habib (Ed.), ISBN: 978-3-902613-15-8.
- [11] Yu, Haoyong, Adam Skwersky, and Steven Dubowski. "Omni-directional Mobility Using Active Split Offset Castors." *Journal of Mechanical Design* 126 (2004): pp. 822-829.
- [12] Lowe, A. J. "QFD Tutorial." *Webducate | Innovative Solutions for E-Learning*. 2000. Web. 24 Aug. 2011. <<http://www.webducate.net/qfd/qfd.html>>.
- [13] "Features & Design | HMMWV (Humvee)." *AM General LLC - Mobility Solutions for the 21st Century*. AM General LLC, 2011. Web. 5 Aug. 2011. <<http://www.amgeneral.com/vehicles/hmmwv/features.php>>.
- [14] "Pacejka Magic Formula." *Dolphinity Racer - Car and Racing Simulator*. Web. 15 Aug. 2011. <<http://www.racer.nl/reference/pacejka.htm>>.
- [15] "Index of  
/maxon/assets\_external/Katalog\_neu/eshop/Downloads/maxon\_motor\_control/1-Q-EC-Verstaerker/DEC\_50\_5/230572." *High Precision Drives and Systems Maxon Motor - Supplier of High-precision Drive Systems. The Product Range Is Comprehensive: Dc Motors, Brushless Motors, Planetary Gears, Spur Gears, Servo Amplifiers, Position Controllers, Wormgear. Maxon Motor*. Web. 10 Aug. 2009. <[http://shop.maxonmotor.com/maxon/assets\\_external/Katalog\\_neu/eshop/Downloads/maxon\\_motor\\_control/1-Q-EC-Verstaerker/DEC\\_50\\_5/230572/](http://shop.maxonmotor.com/maxon/assets_external/Katalog_neu/eshop/Downloads/maxon_motor_control/1-Q-EC-Verstaerker/DEC_50_5/230572/)>.

- [16] "Index of  
/maxon/assets\_external/Katalog\_neu/eshop/Downloads/Katalog\_PDF/maxon\_ec\_motor/EC-flat-programm/new/newpdf\_09." *High Precision Drives and Systems Maxon Motor - Supplier of High-precision Drive Systems. The Product Range Is Comprehensive: Dc Motors, Brushless Motors, Planetary Gears, Spur Gears, Servo Amplifiers, Position Controllers, Wormgear. Maxon Motor.* Web. 10 Aug. 2009.  
<[http://shop.maxonmotor.com/maxon/assets\\_external/Katalog\\_neu/eshop/Downloads/Katalog\\_PDF/maxon\\_ec\\_motor/EC-flat-programm/new/newpdf\\_09/](http://shop.maxonmotor.com/maxon/assets_external/Katalog_neu/eshop/Downloads/Katalog_PDF/maxon_ec_motor/EC-flat-programm/new/newpdf_09/)>.
- [17] National Instruments. *NI USB-621x User Manual*. 2009.
- [18] Callahan, Brian. "Multifilar Suspension Method for Measuring Mass." *Radio Control Nitro Engine R/C RC*. Jan. 2004.
- [19] Ogata, Katsuhiko. "Chapter 3: Mechanical Systems." *System Dynamics*. Fourth ed. Upper Saddle River, NJ: Pearson/Prentice Hall, 2004, pp. 82-83.
- [20] Porter22, Joshua. "Win an Xbox 360 Wireless Controller Just for Reading Bokardo! « Bokardo." *Bokardo*. 22 Nov. 2006. Web. 17 Aug. 2011.  
<<http://bokardo.com/archives/xbox-360-giveaway/>>.
- [21] Roper, Chris. "Xbox 360 Wireless Controller Tour - Gear Feature at IGN." *IGN Gear: Previews, Reviews, and News*. IGN, 13 May 2005. Web. 17 Aug. 2011.  
<<http://gear.ign.com/articles/613/613588p1.html>>.
- [22] Smith, Nicholas D. *Understanding Parameters Influencing Tire Modeling*. Technical Report. Colorado State University, 2003.

- [23] Judy Hsu, Yung-Hsaing. *Estimation and Control of Lateral Tire Forces Using Steering Torque*. Stanford University, Palo Alto, USA, 2009. ISBN: 978-1243609298
  
- [24] "Modelling of Tyres." *Etusivu - Tampereen Teknillinen Yliopisto*. Web. 15 Aug. 2011.  
<[http://www.tut.fi/plastics/tyreschool/moduulit/moduuli\\_10/hypertext/8/8\\_1.html](http://www.tut.fi/plastics/tyreschool/moduulit/moduuli_10/hypertext/8/8_1.html)>.
  
- [25] "Tire Model in Driving Simulator." *Dynamics and Control at SUNY at Buffalo*. University of Buffalo. Web. 14 July 2011.  
<<http://code.eng.buffalo.edu/dat/sites/tire/tire.html>>.
  
- [26] Dihua, Guan, Shang Jin, and L. H. Yam. "Modeling of Tire Cornering Properties with Experimental Modal Parameters." *Tire and Wheel Technology* SP-1439 (1999): pp. 31-36.
  
- [27] Short, Michael, Michael J. Pont, and Qiang Huang. *Simulation of Vehicle Longitudinal Dynamics*. Tech. no. ESL 04-01. 1st ed. Vol. 4. Safety and Reliability of Distributed Embedded Systems.
  
- [28] Willis, Mark. *Proportional-Integral-Derivative Control*. Technical Report. University of Newcastle, Newcastle upon Tyne, UK, 6 October 1999.